2022 Doctoral Dissertation

Guidance of Axon Outgrowth Activated by

Femtosecond Laser Processing in a Microfluidic Device

(マイクロデバイスのフェムト秒レーザー加工によ

って制御された神経細胞の軸索伸長誘導)

Dian Anggraini

Nara Institute of Science and Technology

Graduate School of Materials Science

Bio-Process Engineering Laboratory

(Main Supervisor: Prof. Yoichiroh Hosokawa)

September 2022

Table of Contents

Chapter 1

General Introduction

1.1 Importance of single-cell analysis

Cells are known to have heterogeneity even in the same population and with neighboring cells, which may display different characteristics and biophysical properties relevant to various mechanisms of cellular development, regeneration, and evolution.[1–6] Bulk cell analysis is started by cell loading, culture, and manipulation at a population level. The cells come into contact with each other and produce substances that can induce signal transduction pathways in other cells. These events promote cellular diversities among cell populations, resulting in an average of cellular and subcellular information. During cell manipulation, cell responses (*e.g.*, morphology, proliferation, differentiation, and migration) often do not interpret the actual cellular phenomena due to the cross-talk of cells and substances. In addition, the failure of disease treatment can also occur due to cell heterogeneities.

To overcome these limitations, single-cell analysis is necessary to obtain homogeneous cellular information at a single-cell level. Single-cell analysis can be consisted of single-cell isolation, cultivation, and manipulation conducted on-chip and off-chip for performing cell phenotyping, cell-cell interaction investigations, and omics profiling.[7–13] Single-cell manipulation is required to actuate the cells to observe the actual and sequenced cellular and subcellular information during on-chip analysis. Also, it helps deliver the molecules affecting cell responses, *i.e.*, the production of uniform single-cell clones and cell-derived products during on-chip analysis,[14–16] and is helpful for detailed further single-cell analysis off-chip.[17,18] Further, in examining drug efficacy, single-cell manipulation is needed to precisely actuate, deliver, and treat the individual cells with specific drugs in a particular state of diseases.

1.2 Purpose of single-cell analysis for cell behavior

In conventional cell culture methods, cells are cultivated at a population level, resulting in an average of information about cellular populations. In single-cell analysis systems, individual cells are cultured to monitor the cells' behavior and produce single-cell derived clones and bioproducts. The observation of cellular phenomena of individual cells can be performed periodically and sequentially. Various cell behaviors of single cells that need to be investigated to understand the mechanisms underlying each phenomenon are morphology, proliferation, differentiation, and migration.

Cell morphology represents the shape, structure, and size of cells. Animal cells are categorized into non-adherent and adherent cells, which float in the medium culture and attach to the culture substrate, respectively. Cell morphology is influenced by cell microenvironment (*e.g.*, stiffness and topographic of culture substrates), neighboring biophysical, and biochemical cues.[19–23] In neuroscience studies, chemical guidance cues are used to induce the outgrowth of neurites and axons of neurons on the scaffolds, which are beneficial in *in vitro* studies and to be applied to promote tissue reconstitution and improve functional recovery after the brain injury.[24–27] One of the fundamental biomaterials containing in cells that respond to various cues is proteins. For example, actin works as a cytoskeleton that determines mechanical, migration, and intracellular transportation properties.[28–30] Cell morphology can be observed by various microscopes, such as an optical microscope, phase-contrast microscope, and fluorescence microscope with chemical tags. Analysis of time-lapse images obtained by these microscopy techniques enables the measurements of spatial and temporal morphological changes during certain interval times. Since cell morphology at a population level is easily influenced by neighboring cells and cell-derived substances, it is desired to measure the basic properties of individual cells during single-cell analysis without interferences from other cells.

Cell proliferation and differentiation are induced by multiple factors derived from scaffolds and neighboring cells, such as stiffness and excreted molecules.[31–36] For example, signals from dead liver cells during liver injury lead to the proliferation and differentiation of neighboring cells to renew and replace the injured cells.[37,38] A stem cell is a rare cell that has both capabilities of proliferation and differentiation, which undergoes self-renewal and produces mature cells with various functions. For example, hematopoietic stem cells in the bone marrow proliferate into cells with stem cell-like capability, *i.e.*, blood progenitor cells (*e.g.*, myeloid and lymphoid). These cells differentiate into other types of blood cells, *i.e.*, lymphocytes, erythrocytes, platelets, macrophages, and granulocytes.[39,40] Single-cell culture and analysis are needed to investigate detailed mechanisms that induce proliferation and differentiation of cells into different shapes and functions. It is also beneficial to increase the specificity of measurements that influence those cellular phenomena.

Cell migration is involved in cell morphogenesis during development and pathological states, which influences tissue formation, tissue regeneration, and wound healing. During migration, cells communicate with neighboring cells and tissues, allowing the movement of harmonized cells into target locations.[41,42] During the development of the mammalian brain, as much as 60% of all neurons, cerebellar granule cells migrate along radial glia fibers. The neurons move from the external granule layer to the internal granule layer.[43,44] In terms of tissue regeneration, the transplantation of neural progenitor cells can migrate to the injured tissue and differentiate into neurons, astrocytes, and oligodendrocytes.[45] Besides, stem cells can also migrate to the injured tissues and secrete growth factors to induce cell/tissue regeneration.[46] The factors involved in cell migration are the chemical gradient in solution (chemotaxis) and the gradient of chemoattachment (haptotaxis).[47,48] These factors are found highly complex in *in vivo* conditions. Therefore, single-cell cultivation in a controlled environment is required to

evaluate individual factors on cell migration. In addition, the continuous tracking of individual cells that respond to these factors can also be realized by single-cell analysis.

1.3 Technology for single-cell analysis

During single-cell analysis, individual cells are isolated from heterogeneous or homogeneous cell populations via various methods, *e.g.*, manual pipetting, limiting dilution, density-gradient centrifugation, magnetic cell sorting, and flow cytometry.[49–55] Once single cells of interest are isolated, these individual cells are cultivated and monitored periodically in the desired environment to demonstrate their cellular phenomena, such as morphology, proliferation, differentiation, and migration. Several conventional culture vessels, such as Petri dish and multi-well plate, have been widely used for culturing single cells. The cells are firstly agitated by various methods, such as shaking, stirring, sieving, density gradient-centrifugation, and manual selection. The separated cells from the clusters are then ready to be placed and cultured in a soluble, semisolid, or solid medium.[54,56–59] Using this method, the individual plant cells can divide and differentiate into embryos.[54,58] Unfortunately, the cells are not isolated from other individual cells, leading to the possibility of cross-talk of cellular products and being limited to subsequent cell manipulation. Also, manual methods, *i.e.*, sieving by a nylon screen or gauze and manual selection by a pipette, are impractical, time consuming, and increase contamination probability.

Recently, other culture vessels have been developed to increase the simplicity efficiency of single-cell analysis, *i.e.*, microgels and micropatterned substrates. Microgels made from hydrogels (*e.g.*, alginate, agarose, collagen, hyaluronic acid, and polyethylene glycol) are employed to trap individual cells and provide the space for single-cell cultivation. This method has enabled long-term single-cell cultivation. Furthermore, based on its porous structure, the microgel acts as a 3D culture matrix that provides the transport and exchange of nutrients, pH,

oxygen, secretome, and wastes.[60,61] However, some challenges of this method still need to be addressed, *i.e.*, low effectivity of single-cell trapping limited by the Poisson distribution, non-optimum cell behaviors due to excess cell debris and cell secretions in long-term culture, and dependence on temperature shifting, ion addition, and pH adjustment to induce sol–gel transition, which may induce cellular and subcellular changes.

In addition, micropatterned substrates fabricated by various technologies, *e.g.*, photolithography, laser ablation, thermo-responsive polymer brush, and microcontact printing, allow the culture of adhered single cells in the patterns. This approach results in the adhesion and differentiation of the cells by the geometric cues of the substrates.[62–69] Despite of the ability to control attachment and culture at a single-cell level, this approach lacks the cell confinement structure to support effective cell capture. Thus, cell loss due to the applied high shear stress can still occur. Furthermore, the developed substrate is suitable for only one type of cell, which is limited for advanced applications, such as cell–cell interactions. As an alternative, microfluidics is a promising method, which allows the process of introduction, cultivation, manipulation, and analysis in one chip at single-cell level with flexible handling, inexpensive processes, and high throughput.[28,30–33]

Microfluidic devices have several advantages over previous culture vessels and methods. Microfluidic platforms can be equipped with various microscale compartments, so that they only require a small sample size and reagent volume, resulting in an efficient and sensitive analysis.[14,15,70,71] Also, several controllers can be incorporated within the device to regulate the process of single-cell loading, sorting, trapping, and dispensing, allowing continuous processing with reduced labor costs and contaminations.[15,18,72–78] Real-time measurement techniques, such as time-lapse microscopy, fluorescence microscopy, Raman microscopy, mass spectrometry, electrical impedance spectroscopy, and electrophysiological recording, can also be integrated with microfluidic systems to ensure direct evaluation of cellular behaviors with

high reliability, precision, and accuracy.[15,16,18,73,78–84] Finally, micromanipulators and reverse fluidic forces (*e.g.*, hydrodynamic force) can be applied to recover single cells for further downstream analysis, *e.g.*, real-time quantitative PCR (qPCR) and whole genome sequencing.[15,18,85] Thus, effective and efficient complete analyses of single cells from upstream to downstream can be carried out using one integrated microfluidic chip.

During and after single-cell cultivation, numerous manipulating forces can be incorporated to actuate the cells or substrates, *i.e.*, mechanical, magnetic, electrical, acoustic, and optical forces. Dielectrophoretic is one of the mechanical forces generated from the induced motion of polarizable particles in an ununiform electrical field. This technology has been proven as a versatile force to manipulate microparticles, nanoscale materials, bioparticles, and cells.[18,86] However, this approach may induce cell interferences due to the applied electrical fields. In addition, one of the optical forces, optical tweezers, are widely used in precise single particle and single cell handling, which are attracted toward the center of the beam.[87,88] However, this technology has limitations in handling multiple cells at the same time. To overcome this limitation, femtosecond (fs) laser with the characteristic of spatiotemporal resolution has been used to manipulate cells and substrates in different sites and timing, realizing actuation in real-time conditions and single-cell resolutions.[62,64,89–92] In addition, the fs laser that works at 800 nm wavelength has the capability to penetrate the most transparent objects, such as cells, cell scaffolds, glass materials, and cell culture dishes.[92–99] These advantages are beneficial to incorporate in various culture vessels, including microfluidic devices. Therefore, this study incorporated a microfluidic device and a fs laser to improve the reliability and reproducibility of single-cell analysis, such as cell manipulation and cell sorting.

1.4 Microfluidic devices for single-cell analysis

Single-cell analysis offers opportunities to measure actual and uniform cellular and subcellular phenomena from upstream to downstream at a single-cell level. Analyzing individual cells in microfluidic platforms typically starts by adjusting cell seeding concentration to fit the designed microchambers, allowing single-cell view and single-cell trapping in confined spaces. The individual cells are cultivated and manipulated in response to various substances to produce single-cell clones and/or express their cellular phenomena. Besides, single cells can also be cultivated with other types of single cells to reveal cellular communication. The use of microfluidic devices for single-cell analysis simplifies the setup of measurement and enables the investigation of the influence of various cellular factors. Microfluidic devices for single-cell analysis categorized based on materials and methods are discussed.

1.4.1 Materials

Numerous types of microfluidic devices have been developed for single-cell analysis. Typical materials used to fabricate microfluidic platforms for single-cell analysis, *i.e.*, polydimethylsiloxane (PDMS) and glass. In addition, other materials such as silicon and porous membrane are also utilized.

1.4.1.1 Polydimethylsiloxane (PDMS)

In the last century, PDMS has been a common material used to fabricate microfluidic devices with numerous favorable characteristics, such as flexible, biocompatible, and permeable. The production of PDMS-based microfluidic devices always requires fabricating the mold with soft lithography techniques. The mixture of PDMS and curing agent is poured on the fabricated mold followed by the curing process. The cured PDMS can be formed into a

wide variety of structures and sizes. For example, two microchambers separated by parallel microchannels are developed for placing individual cell bodies and axons to obtain reliable individual neuronal analysis.[77] Moreover, two-cell traps that fit with the sizes of the cells are crucial for maintaining the cells in contact to study the interactions between immune cells and tumor cells. Another study implemented narrow channels for observing budding yeast cell division at a single-cell level.[14]

PDMS has been recognized as a biocompatible and non-toxic material for cell culture. Before *in vitro* cell culture, the surface of PDMS is coated with an extracellular matrix to facilitate cell attachment and growth. The growth rate of mammalian cells (*e.g.*, endothelial cells, epithelial cells, fibroblasts, and osteoblasts) on PDMS is similar to polystyrene (PS; material for conventional culture flasks and culture wells).[100] Also, the differentiation of PC12 cells into neuron-like cells cultured on PDMS and PS shows no significant difference in morphology, cell viability, and cell cycle distribution. However, there are increases in gene expression of PC12 cells cultured on the PDMS compared to PS, which may involve the development and function of neuronal cells.[101]

Besides being used as the main chambers, PDMS has also been developed for other functional components in microfluidic devices. A system for measuring contractile forces of single cells using PDMS micropillar arrays has been developed.[102] PDMS valves have also been fabricated to isolate individual Jurkat cells inside the channel.[103] Despite these advantages of the PDMS material for main chambers and functional components, some challenges have been raised during single-cell cultivation. Based on its flexibility, the PDMS chamber is unsuitable to be applied with highspeed fluid flow, which causes channel leakage and deformation. Based on its permeability, PDMS as a culture chamber is also unsuitable for long-term single-cell cultivation, because it can absorb small molecules, such as fluorescent dyes and drugs,[104,105] causing misleading quantitative data and false-negative results. In addition, fewer interactions

of animal cells and viruses are shown in the PDMS-based microfluidic chamber than in the conventional chamber.[106] This might be caused by the hydrophobic conformer of viruses that can be easily adsorbed to the PDMS.[107]

1.4.1.2 Glass

Glass is another typical material used to develop microfluidic devices due to its biocompatibility, mechanical and chemical stability, optical transparency, and rigidity. Glass has been used as the main channels and supporting parts of microfluidic chips. Microstructures in glass-based microfluidic devices can be fabricated by various methods, *e.g.*, wet etching, dry etching, laser fabrication, mechanical fabrication, photostructuring, and molding process.[108] The fabricated glass is then modified and coated with a certain extracellular matrix to influence cell attachment and growth. Borosilicate glass as a culture substrate is compatible for growing neurons,[109,110] bacteria,[111] and stem cells.[112] Moreover, fused silica glass also allows the growth of animal cells.[113,114]

Due to its mechanical and chemical stability, glass is suitable for long-term single-cell cultivation and analysis in microfluidic devices. Glass does not absorb any molecules, both organic or inorganic, and is resistant to high-pressure liquid perfusion in microfluidic devices for single-cell cultivation.[79] Thus, the loss of culturing cells caused by chamber deformation can be prevented. In addition, glass is optically transparent, allowing high-resolution imaging of individual cells, such as single bacterial cells,[115] the special part of single moss (*e.g.*, bud and gametophore),[116] and single bacterial cells in droplets.[76,117] Therefore, real-time analysis techniques can be equipped with glass-based microfluidic devices for monitoring single-cell behaviors, *e.g.*, Raman spectroscopy, optical impedance spectroscopy, and fluorescence microscopy.[79,81,118]

In addition to these characteristics, glass has high rigidity and low conductivity properties. Glass can be embedded with the electrode material (*i.e.*, platinum) called Envirostat, integrated with negative dielectrophoretic (nDEP) force for efficient single-cell isolation and cultivation.[83,119] For highly reliable single-cell analysis, functional components, such as electrode inlays and valves, have also been developed in glass-based microfluidic devices. Glass is used to create an electrode template connected with PDMS containing target cells.[81,120] In addition, glass valves integrated with thin glass can control the solution flow inside the microfluidic channels. By applying the pressure on the thin glass, open and close switching of each glass valve can be performed, providing the large-scale manipulation, culture, and analysis of individual cells.[121]

1.4.1.3 Other materials

Despite the common use of PDMS and glass materials, they are unsuitable for all types of microfluidic devices. Based on the above discussion, PDMS has an unfavorable characteristic, *i.e.*, deformation due to the shear flow, causing channel leakage and cell loss. Although glass has a more rigid feature to tackle the deformation problem, it has low conductivity, which makes it impossible to be mounted with peripheral electronic connectors. Other materials, *i.e.*, silicon (Si), have been used for microfluidic platforms with rigid, biocompatible, and conductivity properties. It has been reported that silicon-on-insulator wafers can be integrated with electronic pressure regulators to induce pressure-driven flow for single-cell capture and cultivation.[18] In addition, a silicon chip coupled with a plasma source with a pair of microelectrodes is used to investigate the reactive species of individual cells.[122]

Another material that has also been widely reported in single-cell cultivation-based microfluidic devices is the porous membrane. This material is developed for providing culture spaces and supporting components in microfluidic devices. As culture space, the porous

membrane is seeded with the first cells, and it is flipped over to be sealed by the second cells. This enables the cross-talk of cell metabolites located in each pore.[85] As supporting cultures, the porous membranes are beneficial for gas and medium interchange. The membranes are implemented to squeeze the air out and diffuse the electrolysis-generated bubbles from the chamber, which are useful for the next solution introduction and cell cultivation.[121,122] Moreover, the membrane is installed between the PDMS plate and waste tank, inducing medium exchange during medium flow.[123]
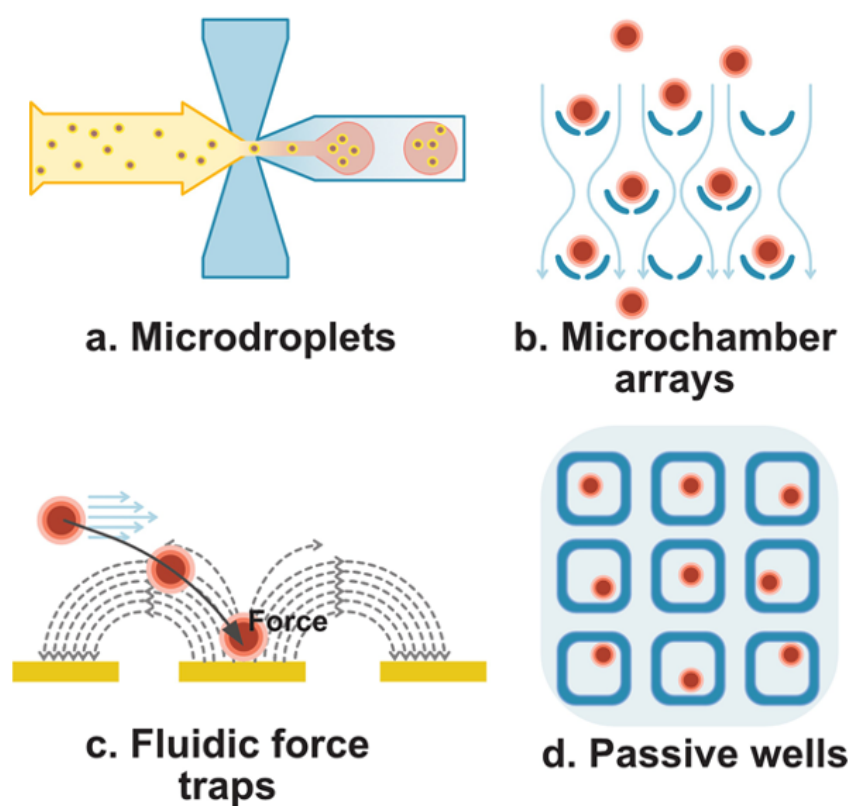
Figure 1. Schematic illustration of methods of microfluidic devices for single-cell analysis. Microfluidic-based methods used for single-cell analysis are classified into (a) microdroplets, (b) microchamber arrays, (c) fluidic force traps, and (d) passive wells. Reproduced from ref. 124 with permission from Royal Society of Chemistry (RSC).

1.4.2 Methods

Individual cells that are seeded and cultured in microfluidic devices originate from either heterogeneous or homogeneous cell populations. In the case of heterogeneous derived cells, the cells need to be sorted to obtain homogeneous cell population and then seeded in the trapping

structures for single-cell cultivation and manipulation. Afterwards, real-time measurement can be performed during these processes. Advanced microfluidic devices equipped with retrieval structures enable further analysis at the downstream. Therefore, efficient analysis from upstream to downstream can be obtained in one platform. The main methods used in the microfluidic devices for single cell-analysis are classified into microdroplets, microchamber arrays, and fluidic force traps, and passive wells **(Figure 1)**.[124]

1.4.2.1 Microdroplets

Droplet microfluidic devices have been used to precisely perform on-chip and various downstream processes. Single-cell droplet microfluidics consist of compartments for cell sorting, droplet generation, droplet imaging, droplet sorting, and single-cell cultivation, manipulation, and analysis. For example, homogeneous chemotactic bacterial cells can be obtained from heterogeneous bacteria by the chemotactic response to aspartic acid gradients.[125] Then, an optimal concentration of cell suspension is mixed with optimal flow rates of the internal and external phases in a capillary channel-based droplet generator. The size and design of droplet generators are optimized to allow the encapsulation of only a single cell in a droplet.

Despite the optimal concentration of cell suspension and optimal flow rates of both phases, Poisson statistics also play a role to obtain single-cell events in a droplet. Poisson statistics is described as $P_{\lambda,k} = \lambda^k \exp(-\lambda)/k!$, where k is the number of cells inside a droplet and λ is the mean number of cells per droplet. The probability of single-cell events in a droplet is ranging from 10 to 30% with the estimated $\lambda = 0.1 - 0.5$.[76,125,126]

The attempts to introduce the external and internal phases in the droplet generators can be categorized into active and passive approaches. With an active approach, single-cell encapsulated droplets are produced by adjusting flow rates using syringe pumps.[76,125,127–133] In addition, passive approaches, such as gravity and hydrostatic pressure, are used by adjusting

the height position of the samples.[117,134] Moreover, a manual syringe vacuum and a 3D printed droplet generator can also be employed to create monodisperse single-microbe laden droplets. Both approaches are suited to the design of the microfluidic platform to provide stable, uniform, and continuous liquid in droplet generators.
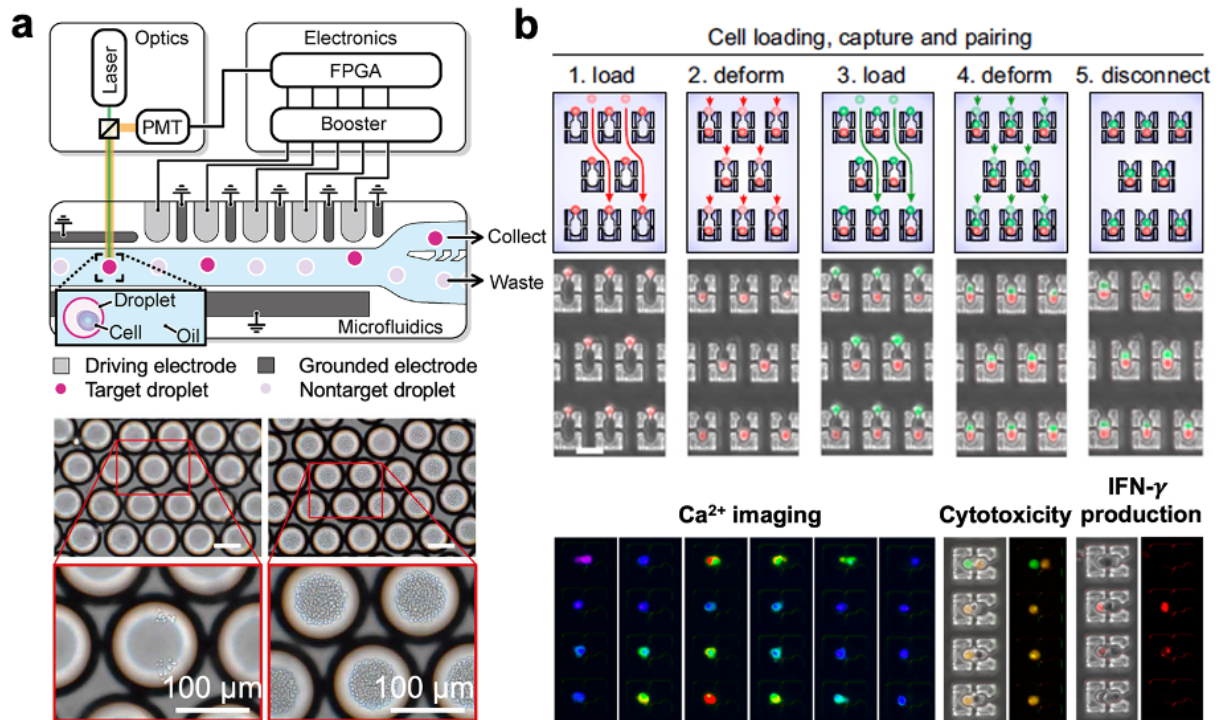
Figure 2. Microfluidic devices based on microdroplets and microchamber arrays for single-cell analysis. (a) A schematic of a microdevice using a dielectrophoretic system for droplet sorting (top). Bright-field images of slow-growing yeast (bottom left) and fast-growing yeast (bottom right) after culture and sorting by dielectrophoretic-based droplet microfluidics. Reproduced from ref. 75 with permission under open license CC BY-NC 4.0. (b) A schematic of a microchamber array for cell-cell interaction. The process consists of the loading of NK92MI cells (1), deformation of type I cells (2), loading of K562 cells (3), deformation of the type II cells (4), and disconnection of all applicants to continue with cell culture (5) (top). Cell-cell interactions between both cells are demonstrated by Ca^{2+} imaging, cytotoxicity, and IFN-γ production (bottom). Reproduced from ref. 15 with permission from National Academy of Sciences.

During droplet generation, a droplet can contain single, double, triple, or beyond cells. Thus, to achieve droplets containing only individual cells, single-cell sorting and manipulation are required. Single-cell sorting is performed by identifying the cells based on various cell information, *e.g.*, cell number, cell size, and DNA/RNA sequences. The cell information is

identified by observing cell-laden microdroplets flowing through the channels with an optical microscope, fluorescence microscope, and Raman microscope.[74,76,117] The target cells are sorted from the non-target cells with numerous manipulation system, *i.e.*, a valve-based sorting, a dielectrophoretic system **(Figure 2 (a)),**[74–76,126,135] and a capillary-tuned solenoid microvalve.[76] In addition, fluorescence intensity from the cells is detected to determine an electrical signal that triggers the driving electrodes to produce a dielectrophoretic force on the target droplets.[74,75,135]

The isolated single-cell laden droplets are then directly analyzed or recovered for further observation. The recovery process is assisted by varied attempts, such as a capillary interface to collect a droplet in the tube (one-cell-one-tube), the different phases of the flow solution and the collecting well, and the pipette aspiration.[76,117] The collected single-cell laden droplets are investigated for the visualization of gene expression, RNA sequencing, and whole-genome sequencing.

1.4.2.2 Microchamber arrays

Microfluidic devices embedded with microchamber arrays have advantages in precise single-cell separation and large-scale single-cell manipulation. Because of the micro size of structures for trapping single cells, separating cells is crucial to prevent clogging and ensure the distribution of cells in the array-based microfluidic devices. Single-cell loading and separation in the array-based microfluidics can be achieved by incorporating mechanical filters,[15] entrapped air bubbles,[73,136] hydrodynamic forces,[18,137] and hydrostatic forces.[138]

In microfluidic devices with microchamber arrays, individual cells (both non-adherent and adherent) flow to each microchamber which acts as a cell trap for further cultivation and analysis. In handling non-adherent cells, it is crucial to attain single cells by proper perfusion methods and suitable trap structures to prevent cell misplacement. Different types of arrays,

such as capture structures (*e.g.*, lane trap and two-cell trap),[15,18] narrow channel,[14,139] and geometric confinements,[70] have been employed for efficient individual non-adherent cell trapping and analysis. A dual flow rate is employed to load (low flow rates) and squeeze (high flow rates) cancer and immune cells into a microchamber array, showing cell-cell interactions in the expression of Ca^{2+} imaging, cytotoxicity, and growth factor production **(Figure 2 (b))**.[15] Further, column arrays and narrow channels are utilized to isolate size-related yeast mother cells and observe the simultaneous division of yeast cells for up to 80 generations, respectively. Both devices are useful for analyzing the lifespan of yeast mother cells and mother-daughter cells related interaction and phenomenon.[14,70]

Furthermore, array-based microfluidic devices are commonly utilized for simultaneously evaluating the growth and development of non-adherent cells, *e.g.*, germination screening of fungi spores,[138] heterogeneity analysis of tumor cells,[72] growth rate analysis of bacteria and yeast,[73,140] and sex differentiation of diatom. They are also useful for culturing bacteria morphology, behaviors, and protein intensity.[136,141] In principle, the cells delivered into each chamber are cultivated for several hours or days in controlled medium perfusion with or without additional molecules or substances to induce cellular responses. Relatively low flow rate is usually applied to prevent the detachment and interferences of adherent cells in the growth chamber. Afterwards, the cellular phenomenon can be recorded by time-lapse and fluorescence microscopy, enabling real-time investigation of individual cells. For long-term single-cell cultivation, the accumulated cell debris and cell secretions may affect the performance of the cells. Thus, diffusion of medium based on mass transport and through the semipermeable membrane can be applied to achieve low shear stress during the medium exchange.[72,73,123,136]

Besides direct assessment during cell trapping and cultivation, some microdevices enable retrieval of cultivated cells for off-chip analysis. A simple cell recovery can be performed in an open-format device designed from top to bottom: a PDMS channel, PDMS membrane, and

coverslip. The trapping and manipulation of cells are carried out in the PDMS channel, on the top of the PDMS membrane. After cell manipulation, the ultralow-temperature agarose gel is poured into the channel containing cells, allowing cell trapping in the agarose gel. The device is opened and flapped, and then the desired single cells can be recovered by a micromanipulator. Finally, individual cell cultivation is conducted to obtain sufficient numbers of single-cell clones that are useful for gene profiling.[15]

1.4.2.3 Fluidic force traps

Fluidic forces, such as hydrodynamic and dielectrophoretic forces, have been reported for manipulating individual cells in microfluidic platforms. Hydrodynamic force is the phenomenon that arises from fluid velocity and acceleration, which is useful for isolating, trapping, culturing, and manipulating single cells. Hydrodynamic force for single-cell isolation allows the detachment of adherent cells and the collection of individual cells that are useful for further single-cell investigation. Hydrodynamic force is typically designed to deliver single cells to the physical constraint traps for single-cell trapping and cultivation. Individual T cells are loaded into the bypass channels and flowed into the lane traps (P2 – P3), which has higher fluidic resistances (P2 – P3) than those along each bypass channel (P1 – P2 and P1 – P3). After a single cell is trapped, the pressure along the main channel and lane trap remains low to prevent the loss of the trapped cells. The trapped cells are allowed to proliferate and occupy the subsequent lane traps. Thus, each lane trap consists of sister and cousin cells from the single mother cell, which enables to elucidate multigenerational relationships and mutation phenomena across sub lineages.[17,18]

In addition, hydrodynamic force is applied in the capture structures to trap single cells flowing from bypassing channels. Single-cell capturing can be achieved by applying a higher hydrodynamic resistance at the capture structure than at bypassing channel. After the different

cells are trapped, the backflow solution is applied to transport the cells from the capture structure to the microchamber. Eventually, specific cell-cell interactions of individual cells (*i.e.*, cancer and endothelial cells) are observed inside the microchambers by time-lapse microscopy. Lastly, hydrodynamic for is also employed for cell retrieval. The reverse differential pressure is applied to move a single T cell from the lane trap into the main channel. Thus, individual cells can be collected by flushing with buffer, and downstream analysis of single-cell transcriptomics is performed.[18]
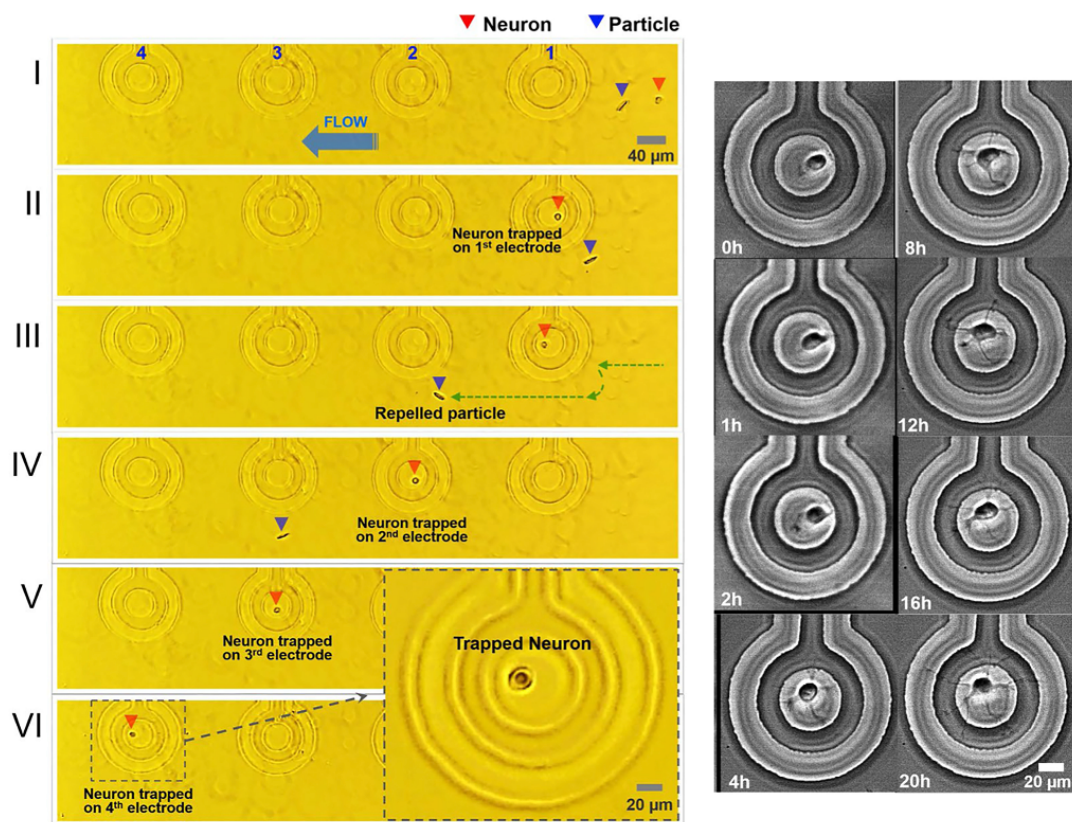
Figure 3. Microfluidic devices based on dielectrophoretic forces for single-cell analysis. The microfluidic device with a negative dielectrophoretic (nDEP) force for trapping and cultivating neurons. The neuron is flowed and is trapped in the 1st electrode (I and II). The particle is repelled by the 1st electrode and moved with a medium flow (III). When the 1st electrode is turned off, and the 2nd electrode is turned on, the neuron flows out from the 1st electrode and is trapped in the 2nd electrode (IV). A similar process is observed for the 3rd and 4th electrodes (V and VI) (left). The trapped single neuron is cultured for 20 h, resulting in the outgrowth of neurites (right). Reproduced from ref. 120 with permission under open license CC BY.

Single-cell processing has also been carried out by dielectrophoretic force, which is produced when the dielectric particles are subjected to an inhomogeneous electric field.

17

Negative dielectrophoretic (nDEP) force is used for single-cell processing without the contact with electrode surface. The development of 3D octupole microelectrodes in Envirostat 2.0 enables contactless trapping and cultivation of various bacteria, *e.g.*, *Bacillus subtilis*, *Escherichia coli*, and *Corynebacterium glutamicum*. The device consists of channels for cell separation, isolation, cultivation, and disposition. By actuating pump mode one, the cell subpopulation in the separation channel flows into the waste outlet for cell dispensing and the isolation channel for cell trapping, controlled by the deflector electrode and the gate electrode, respectively. The isolated cells are trapped by funnel electrodes. Then, by deactivating pump mode one and activating pump mode two, the trapped cells move to the cultivation channel and are retained by funnel and octupole electrodes. Individual cells are cultivated with a continuous perfusion culture medium for observing the growth of bacteria. Finally, by activating pump mode three, the cultivated single cells and extracellular metabolites secreted by single clones are deposited for off-chip analysis, such as mass spectrometry.[142]

In addition to advanced single-cell analysis, high-resolution tools (*e.g.*, Fourier-transform ion cyclotron resonance mass spectrometry (FT-ICR-MS)) can also be coupled with nDEP-based microfluidic devices for evaluating secondary metabolites of *C. glutamicum*.[83] Besides, the array of ring-shaped electrodes producing nDEP allows the maintenance of single cells in the microfluidic device. By turning on and off the nDEP force, the single neurons can be trapped in the target electrode and cultivated **(Figure 3)**. This device can also be integrated with electrophysiological recording for measuring action potentials of individual neurons in real time.[120]
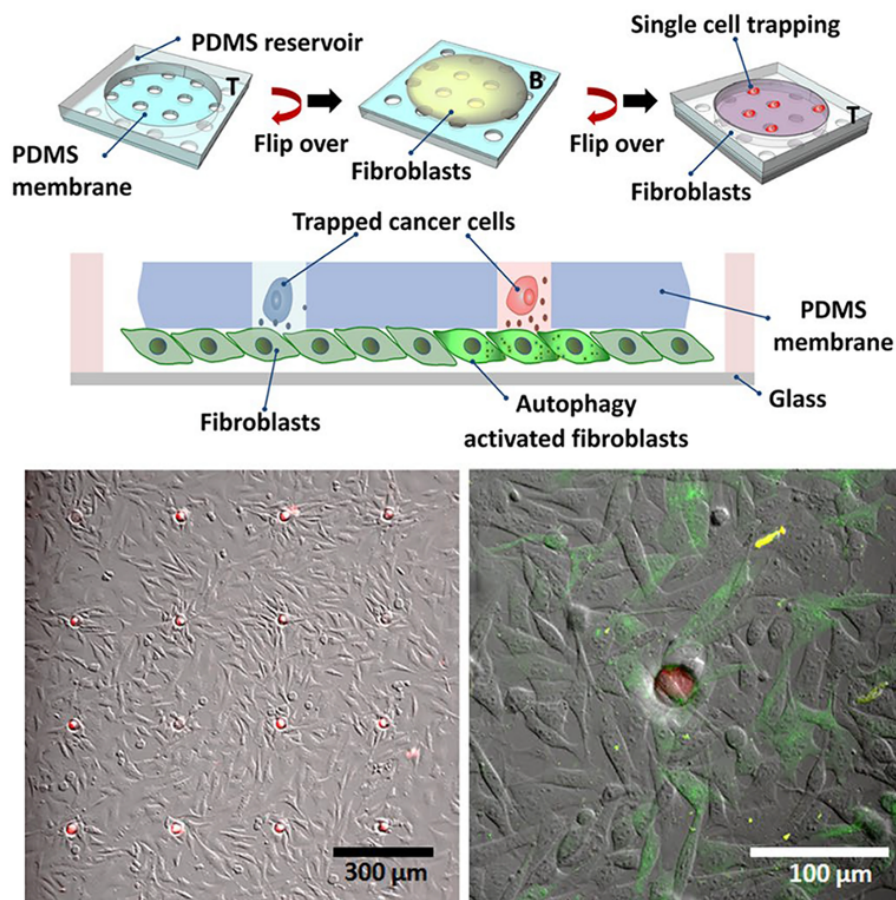
1.4.2.4 Passive wells

Compared to microdroplets, microchamber arrays, and fluidic force traps, passive well-based microfluidics enables simple but precise single-cell trapping, cultivation, real-time

analysis, and post-treatment analysis. Single-cell trapping and cultivation in the passive wells can be obtained by flipping the multilayer device consisting of a microchannel with two sets (*i.e.,* upper and below sides) of microwell arrays. These microwells have different diameters (d) and heights (h), *i.e.,* small microwells (d: 25 µm, h: 30 µm) for cell capture and large microwells (d: 285 µm, h: 300 µm) for cell culture. Suspensions of KT98 cells and A549 cells are loaded into the microchannel, and the cells automatically move to the capture wells by gravitational force. The excess cells are flowed out from the microchannels, and then only individual cells remain in the capture wells. By flipping out the device, single cells from the capture wells transfer into culture wells by gravitational force, resulting in only one cell in one well. The trapped cells are cultivated by adding a differentiation medium to induce differentiation of KT98 cells and a medium containing epithelial growth factor (EGF) to induce colony formation of A549 cells.[143]

In another study, cell-cell interactions can also be observed using the flipping method. The device consists of a PDMS reservoir for confining cell growth, a PDMS membrane for cell culture, and a PDMS-coated cover glass for supporting the cell position inside the device. The GFP-LC3 transgenic mouse embryonic fibroblasts (MEF) are cultured on the bottom side of the PDMS membrane for 2 h. The PDMS membrane is turned over and attached to the PDMS-coated cover glass. Breast carcinoma cells (MDA) are cultured on the upper side of the PDMS membrane and trapped in the holes of the membrane. MEF shows autophagy activation of up to 30% at 6 h co-culture with MDA, triggered by MDA-produced TGFβ1 **(Figure 4)**.[85] Both studies use fluorescence microscopes for observing cultivation and cell-cell interaction in real time.

Besides adequate single-cell assessments in passive well-based microfluidic devices, off-chip analysis can also be conducted in microfluidic devices with open wells. To confirm the autophagy activation of mouse embryonic fibroblasts (MEF) by TGFβ1-produced breast

carcinoma cells (MDA), MDA-activated fibroblasts are collected from the open microwells using a microscopy-based single-cell picking device. These single cells are then analyzed using PCR to show the expression of TGFβ1. As a result, MEF that are co-cultured with MDA (wild-type MDA and shTGFβ1-infected MDA) show autophagy activation with an accuracy of 81%. This device enables quantitative analysis of the interactions between heterogeneous tumor cells to obtain specific and high-throughput screening of paracrine factors to fibroblasts.[85]

Figure 4. Passive well microfluidic devices for single-cell analysis. A schematic of passive well-based microfluidics, consisting of a PDMS reservoir, a PDMS membrane, and a PDMS-coated thin glass. Fibroblasts and cancer cells are seeded on the bottom and upper sides of a PDMS membrane, respectively (top). A single cancer is trapped in each hole and shows an autophagy activation (red) with fibroblasts (green) (bottom). Reproduced from ref. 85 with permission under open license CC BY.

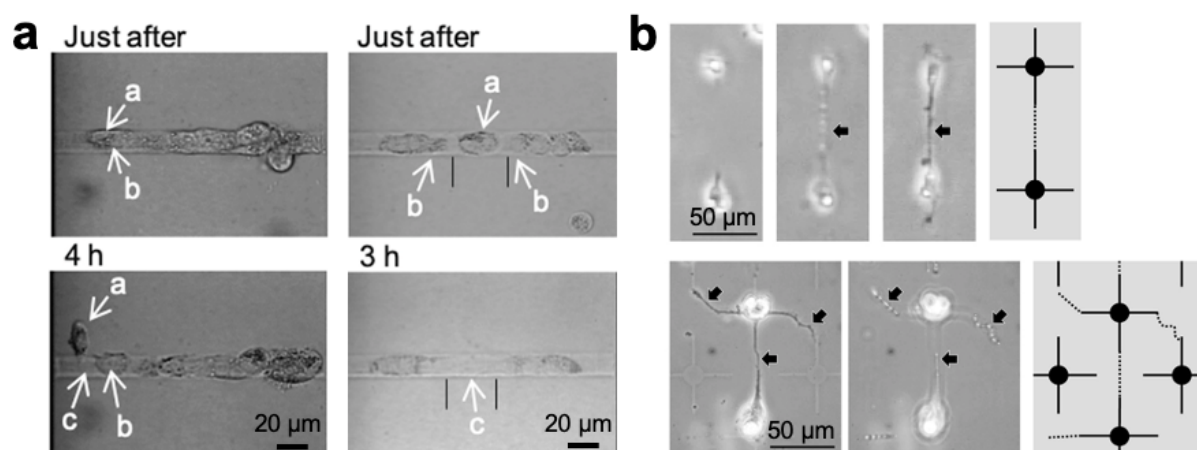## 1.5 Femtosecond laser processing for single-cell analysis

Femtosecond (fs) laser is an infrared laser that emits optical pulses with a high-speed rate in the domain of femtoseconds (1 fs = 10^{-15} s). Fs laser has been used as a powerful tool for

cellular *in vitro* studies and medical purposes. In *in vitro* studies, the fs laser is utilized to study intercellular adhesion, guided neurite outgrowth, cell detachment, and cell sorting.[64,98,144–151] For medical purposes, the fs laser is known as a non-invasive tool in ophthalmology and otolaryngology. In addition, the precise cutting of the laser is beneficial in the fields of cardiovascular surgery, arteriosclerosis treatment, and caries removal.[152,153] These wide applications are due to the advantageous characterization of the fs laser. The fs laser pulse with the 800 nm wavelength can penetrate most cells and cell scaffolds as well as glass materials and cell culture dishes. The multi-photon absorption occurs when the laser pulse is focused by the objective lens, inducing efficient absorption at the laser focal point. Thus, the high precision of 3D imaging and processing of the biological samples can be attained.[93] In addition, the short pulse duration of the fs laser decreases the energy without decreasing the delivered power. Thus, the fluence (energy per unit area) can also be reduced, indicated by the lower heat production, smaller cavitation bubbles, and less collateral tissue damage than the nanosecond and picosecond lasers.[153] Moreover, the fs laser is usually operated with a computer-controlled optical delivery system, allowing high accuracy, reliability, and reproducibility for either *in vitro* or *in vivo* purposes. Furthermore, the fs laser provides spatiotemporal resolution to control the objects in different sites and timing, realizing actuation in real-time conditions and can be applied for a wide range of applications.[92,154,155]

As mentioned above, the fs laser pulse has been applied for various single-cell manipulations. The fs laser is employed for both contact and contactless processing. Based on the ability in penetrating the 3D transparent objects, the fs laser pulse has been used to manipulate cells and culture substrates. A single shot laser ablation is focused on the nucleus of the adherent cells to detach the cells from the culture substrate. The ablated cells are then cultured for a long period, allowing the natural detachment from the culture substrate **(Figure**

21

5 (a)).[156] In addition, the laser scanning is performed to kill the non-target cells and sort the target cells to evaluate cell behaviors, such as cell proliferation and migration.

Apart from ablating the cells, contact processing by fs laser pulse is also carried out to actuate the culture substrates to influence cell behavior. In addition, the fabrication of thin-glass sheet filters with the through hole diameter of 1.94 – 2.64 μm by fs laser pulse is utilized for sorting single particles with the diameter of 1 μm.[98] Besides, the filters are incorporated in a glass device to provide gas and nutrition exchanging for the culture of HeLa, fibroblasts, and embryonic stem cells (ESCs).[97] Other than the using the fabricated filters, cell sorting can also be attained by deep grooves activated by fs laser pulse. The grooves can direct the 10 μm particles in the center of channels, which is expected to be integrated with on-chip detection components for further single-cell analysis.

Figure 5. Contact processing of femtosecond laser pulse. (a) A single shot laser pulse to kill **a** cell (top). The **a** cell is detached from the culture substrate after a few hours of culture (bottom). Reproduced from ref. 156 with permission from Elsevier B.V. (b) Linear shape (top) and customized shape (bottom) of cytophobic areas are ablated by the laser to expose the cytophilic areas, resulting in the outgrowth of neurites along with the ablated areas after 24 h of culture. Left images are the phase-contrast images. Right images are the laser scanning illustrations. Dotted lines represent the laser-scanning lines. Reproduced from ref. 65 with permission from AIP Publishing.

In the studies of guided neurite and axon outgrowth, several methods incorporating fs laser pulse are developed. In my research, the fs laser pulse irradiates the thin-glass sheet to create

the micro-holes, inducing the release of guidance molecules from the laser-fabricated micro-holes. The generated molecular gradient plays a role to promote neurite and axon outgrowth of neurons.[94,95] Furthermore, the ablation of cytophobic area to expose the cytophilic area of cell scaffold is performed for guiding neurite outgrowth arranged in the linear shape of the ablated area **(Figure 5 (b))**.[64,144,151]

In the case of utilizing the generated shock wave following an intense fs laser pulse, numerous single-cell manipulations, such as cell detachment, cell sorting, and intercellular adhesion, can be achieved by fs laser-induced impulsive force. This contactless cell manipulation is carried out by focusing the area inside the culture medium nearby the cells to induce the stress wave. The study of cell detachment is usually followed by further step to sort and isolate the cells. The fs laser-induced impulsive force has been applied to detach and isolate numerous types of individual cells, NIH/3T3,[148,149] PC12,[150] and hippocampal neurons.[147] Morphological evaluation of cell differentiation of PC12 is performed to ensure the safety of cell detachment with fs laser pulse **(Figure 6 (a))**.[150]

Moreover, the study of intercellular adhesion strength is essential to understand mechanisms that occur in single cells. Fs laser-induced impulsive force has the advantage for intercellular adhesion study due to the non-contact processing of the instrument with cells. The adhesion between Madin-Darby canine kidney (MDCK) epithelial cells cultured on the culture insert are studied by focusing the fs laser pulse at 4 μm below the insert in a cell-free area, resulting in the cleavage of cell interface near the focal point. With the estimated pressure loaded, MDCK cells appear to adhere to each other with a few hundred nanonewtons **(Figure 6 (b))**.[145] In the plant cells, the interaction between chloroplast and peroxisome is found in the mesophyll layer of *Arabidopsis thalina* to assist the photosynthesis. Thus, the quantification of the adhesion condition is required. The fs laser-impulsive force can overcome the limitation of

other instruments to manipulate 3D samples. The 61 kPa of mean pressure of laser pulse is able to break the adhesion between the peroxisomes and chloroplasts.[146]
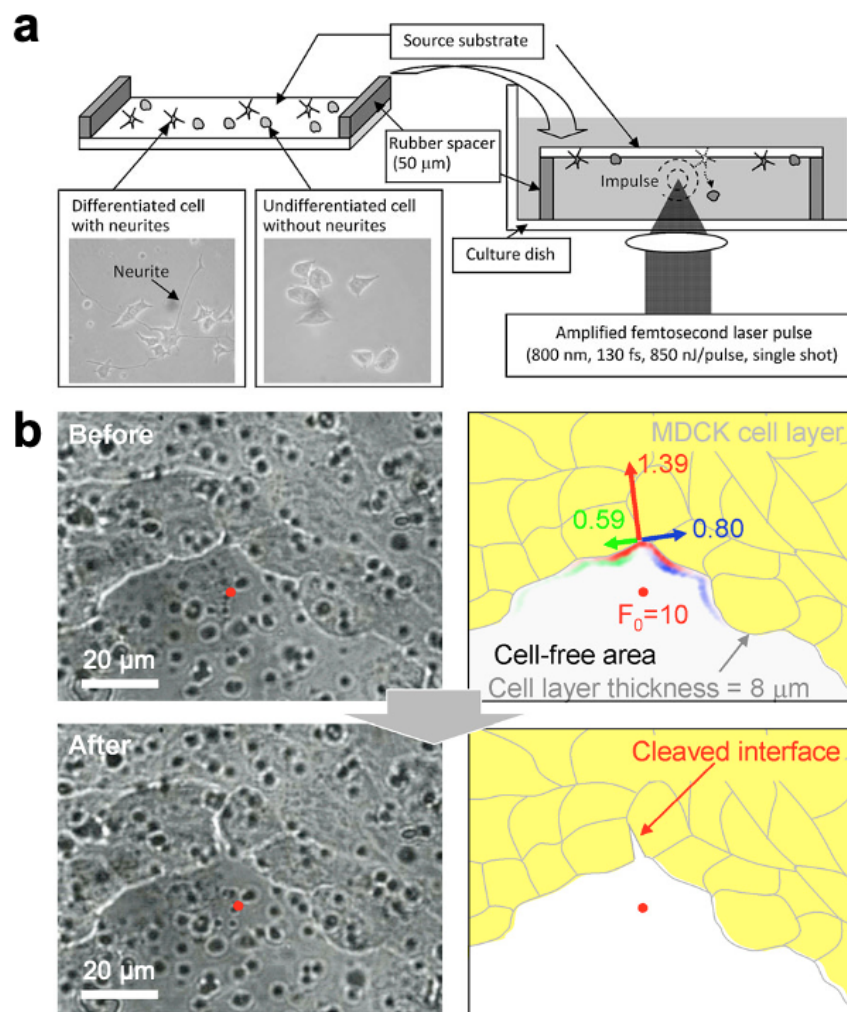
Figure 6. Contactless processing of femtosecond laser pulse. (a) The laser-induced impulsive force is applied to detach the undifferentiated PC12 cells from the culture substrate. Reproduced from ref. 150. Copyright 2010 Springer Science Business Media, LLC. (b) Intercellular adhesion of Madin-Darby canine kidney (MDCK) epithelial cells is studied by focusing the fs laser pulse at 4 μm below the culture area, resulting in the cleavage of the cell interface near the focal point. Reproduced from ref. 145 with permission from National Academy of Sciences.

1.6 Technology for guided neurite and axon outgrowth manipulation

The formation and regeneration of neuronal networks require the precise connection of synapses. The established connections between synapses are controlled by guidance cues that induce guided neurite and axon outgrowth. Dysregulation between guidance cues, signaling pathways, and cell receptors could lead to non-functional synaptic connections, resulting in the

failure of neuronal homeostasis.[157–159] Therefore, the study of guided neurite and axon outgrowth *in vitro* is indispensable for understanding the detailed mechanisms of neuronal communication. Despite the importance of *in vitro* studies, the study of guided neurons is very critical in clinical cell transplantation. Cell transplantation is the current gold standard for the treatment of brain injuries, especially those identified by large lesions, such as traumatic brain injury, spinal cord injury, and stroke.[160–166] However, neuronal regeneration following the cell transplantation alone remains one of the greatest challenges, as identified by poor cell survival, differentiation, and axonal integration.[167–170] Precise axonal integration to form functional synapses is the ultimate goal to obtain functional recovery after brain injury.[171,172] Dysregulation and dysfunction of the synaptic connections could lead to post-transplantation side effects, such as graft-induced dyskinesia.[173] Transplantation of scaffold-embedded guided neurite and axon outgrowth has been reported, which can increase cell survival, axon outgrowth, neuronal tissue reconstitution, and decrease inflammation.[174–176] Several tools and methods, such as micropatterning,[174,177–179] electrospinning,[25,180–183] and three-dimensional (3D) printing,[184,185] have been demonstrated to regulate neurite and axon outgrowth of neurons on scaffolds.

Electrospinning is the method used to align the polymer on the substrate, which is responsible for a topographic cue to improve the mechanical strength and strength resistance of the scaffold. The typical electrospinning apparatus consists of a high-voltage power supply, a syringe, a needle, an electrically conductive collector, and a syringe pump.[186,187] Biocompatible polymers are placed in the syringe with a needle connected with a high-voltage power supply and a syringe pump. Electrospinning is carried out by depositing the polymer released from the needle to the collector. Different types of collectors can be used to obtain electrospun fibers with various orientations. Different diameters of fibers are developed by various factors, *i.e.*, polymer concentrations, the distance from the spinning tip to the collection plate, the flow rate

controlled by the syringe pump, and the voltage of the power supply.[187,188] Afterward, the aligned fibers are formed on the collection screen or form into a thin layer of film as the solvent evaporated and is ready to be used as the cell scaffold for the growth of cells and influencing cell behaviors.[187,188]
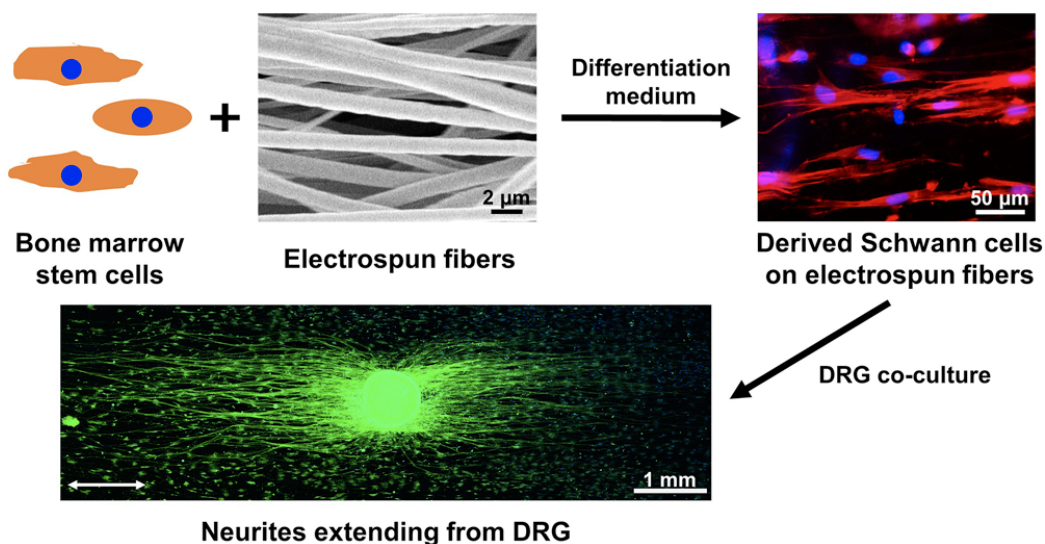
Figure 7. Electrospinning technology for regulating neurite outgrowth. The culture of bone marrow stem cells (BMSCs) on the electrospun fibers promotes the differentiation into Schwann cells aligned on the uniaxial fibers. Co-culture of the derived Schwann cells with dorsal root ganglia (DRG) increases the neurite outgrowth of DRG aligned on the fibers. Reproduced from ref. 190. Copyright 2017 American Chemical Society.

In the study of guided neurite outgrowth, different diameters of electrospun poly-L-lactic acid (PLLA) fibers are used to evaluate neurite length of dorsal root ganglia (DRG), resulting in the direction of neurite length is determined by the fiber's diameter. The large diameter fibers (1325 + 383 nm) induce a longer neurite length and higher directional neurite outgrowth than the small and intermediate diameter fibers.[188] In another study, the smaller diameter of electrospun *Bombyx mori* silk fibroin (SF) materials shows an increase in cell-spreading area with an enhanced migration efficiency of astrocytes.[187] Besides, the uniaxial alignment of electrospun fibers guides the neurite projected along the fibers and directs the perpendicular orientation of the neurites to the aligned fibers.[189] It can also optimize the differentiation of bone marrow stem cells (BMSCs) to Schwann cells and determine the morphology and

alignment of the derived cells. Co-culture of the derived Schwann cells improves neurite elongation of DRG on the uniaxially aligned fibers **(Figure 7)**.[190]

Micropatterning is the method for patterning a cell scaffold for the attachment and culture of the cells to evaluate cell behaviors. Micropatterning can be fabricated by various technologies, *e.g.*, photopatterning,[191,192] thermo-responsive polymer brush,[193] and soft lithography.[26,194] In the previous study, the immobilization of photo-reactive self-assembled monolayer (SAM) (silane-coupling agent) on the glass surface followed by photopatterning is beneficial for guided neurite outgrowth. The SAM surface is immersed in Pluronic resulting in the hydrophobic and hydrophilic layers on the surface. The surface is patterned by ultraviolet (UV) light irradiation to peel off the hydrophilic layer to provide the growth area for the cells. The growth areas for soma and neurite outgrowth are fabricated at different time points. The extracellular matrix (ECM) is introduced into the surface, demonstrating the attachment of soma and neurite outgrowth of PC12 along with the patterned areas.[191] In also utilizing the photopatterning method, the photopolymerizable monomer is exposed to UV light through a photomask to develop micropatterns across the substrate surface, showing the directional neurite outgrowth of spiral ganglion neurons (SGNs) in the directional patterns.

Another method to create micropatterns is soft lithography. The silicon master with specific patterns is fabricated by the proximity of UV lithography. The micropatterned PDMS substrate is developed by pouring the mixture of PDMS and curing agent on the silicon master. The mixture is then cured at 80 °C for 3 h. The neurite and axon outgrowth of hNT2 neuronal cells are directed in the micropatterned substrate which is useful to promote tissue reconstruction and improve functional recovery after motor cortex lesion in rats.[26] Moreover, the fabricated micropatterned PDMS substrate can also be employed to fabricate polyethylene glycol (PEG) hydrogel substrate with silver nanowire (AgNW) to increase the conductivity of the substrate. An electrical stimulus is applied to induce the differentiation of neural stem cells (NSCs) and

guide neurite outgrowth.[194] In the case of the thermo-responsive polymer (TRP) brush method, the PEG-based TRP is firstly immobilized on the gold surfaces. It is followed by controlling the temperature changes from its lower critical solution temperature (LCST), *i.e.*, lower than 33 °C and higher than 37 °C. At temperatures lower and higher than the LCST, the polymers are hydrated and dehydrated, preventing cell adhesion and promoting cell adhesion, respectively. By increasing the temperature than the LCST, the gaps coated with the TRP are shown the neurite contact between the neuronal SH-SY5Y cells and human-induced neuronal cells **(Figure 8)**.[193]
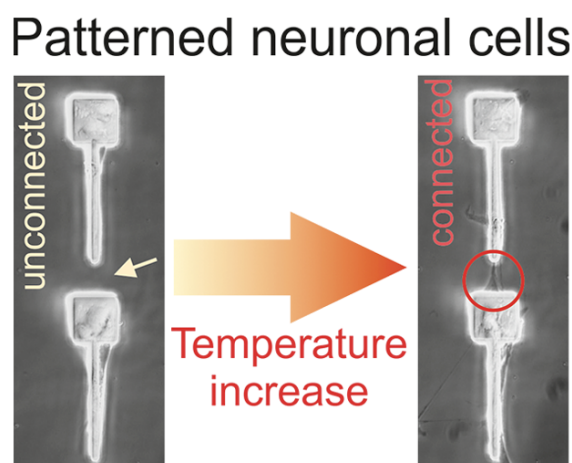
Figure 8. Micropatterning technology for guiding neurite outgrowth. Thermo-responsive polymer (TRP) controls the dehydration of the polymer by changing the temperature from its lower critical solution temperature (LCST), *i.e.*, higher than 37 °C. The increased temperature promotes neurite elongation of the neurons. Reproduced from ref. 193. Copyright 2019 American Chemical Society.

Another typical method to promote neurite and axon guidance is 3D printing. 3D printing is a method of producing 3D objects by fusing and depositing materials on a substrate layer by layer. In the study of tissue regeneration, the digital light-processing-based 3D printing method is implemented to develop a hydrogel scaffold in the shape of a cerebral cortex lesion. The hydrogel consists of polyethylene glycol diacrylate (PEGDA), methacrylated gelatin (Me-Gel), and methacrylated HA (Me-HA). The hydrogel precursor and a guidance molecule (*i.e.*, SDF-1) were printed with a 3D printer to create round-shaped lesions with diameters of 400 and 800

μm. The printing is done layer by layer using a UV projector, enabling the formation of an SDF-1 gradient from the bottom to the top. The gradient inside the lesion can induce the neural stem cell (NSC) migration and cell recruitment toward the ischemic site **(Figure 9)**.[195] Furthermore, the porous poly(lactide-co-ε-caprolactone) (PLCL) nerve guidance conduit fabricated by 3D printing plays a role as a reservoir to deliver the bioactive molecules, inducing the successful axonal regeneration and remyelination capacities.[196] In addition, the organization of axons of human induced pluripotent stem cell (iPSC)-derived retinal ganglion cells (RGCs) is observed axially projecting along the 3D-printed scaffold grooves.[184]
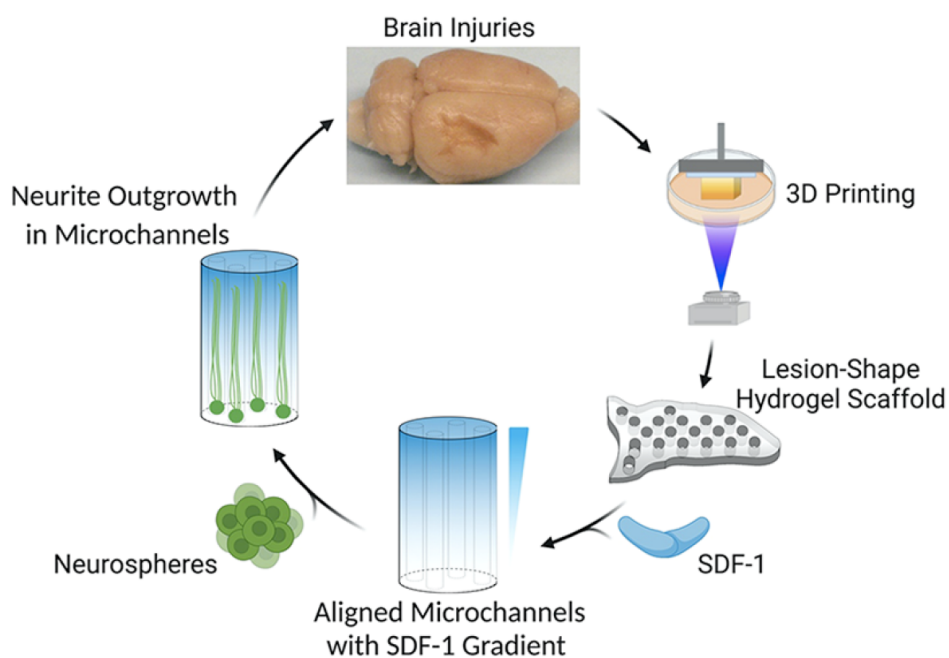
Figure 9. 3D printing technology for guiding neurite outgrowth. The hydrogel precursor and a guidance molecule (*i.e.*, SDF-1) are printed with 3D printing to mimic the lesion cavity of brain injury. The molecular gradient induces the elongation of neurites of neurospheres to the ischemic site. Reproduced from ref. 195. Copyright 2021 American Chemical Society.

Apart from the three approaches, the fs laser has also been used as a powerful tool to regulate neurite outgrowth on the scaffolds. As previously described, the outgrowth of neurite is guided by the development of hydrophilic and hydrophobic layers as the bottom and upper layer of the scaffold, respectively. The fs laser pulse ablates the hydrophobic layer with a specific shape to expose the hydrophilic layer, enabling the soma attachment and neurite

outgrowth to project along the exposed area. The addition of the extracellular matrix adhering to the exposed area is needed, providing the scaffold for cell growth.[64,144,151] By incorporating another approach, the embedded of the developed scaffolds by these technologies in a microfluidic device has also been demonstrated. The microfluidic device can increase the utility of these technologies by providing a place to store the guidance cues to promote neurite and axon outgrowth on the developed scaffolds.[177,197,198]

1.7 Research objective

The study of guided axon outgrowth is essential in neuroscience, both *in vitro* and *in vivo*. In *in vitro* study, the guidance molecule regulates guided axon outgrowth to establish neuronal network formation. Dysregulation between guidance cues, signaling pathways, and cell receptors could lead to non-functional synaptic connections, resulting in the failure of neuronal homeostasis.[157–159] In *in vivo* study, the transplantation of guided neurons on the scaffold has been reported, which can increase cell survival, axon outgrowth, neuronal tissue reconstitution, and decrease inflammation.[174–176] The attempts to develop guided axon outgrowth on the scaffold are necessary to explain detailed mechanisms of neuronal communication and further induce axonal integration to promote functional recovery after brain injury. A femtosecond (fs) laser is a tool that allows precise guided axon outgrowth and axonal integration due to its higher spatiotemporal resolution, lower heat production, and less collateral tissue damage than other pulsed lasers.[92,153–155] In addition, the incorporation of the microfluidic device has also been reported can increase the effectiveness and reliability of observation.[177,197,198]

In this thesis, the research aims to develop a precise and real-time fs laser penetration on a 4 μm thick thin-glass sheet to allow guided axon outgrowth of neurons by molecular gradients in a microfluidic device. Hippocampal neurons isolated from embryonic day 16 (E16) mice are cultured on the thin-glass sheet for 1 day *in vitro* (DIV), while the axon guidance molecule (*i.e.*,

netrin-1)[199,200] is manually introduced to the channel located below the thin-glass sheet. The points on the thin-glass sheet are selected to focus fs laser pulses to create the micro-holes. Two types of micro-hole fabrication are carried out. The first manipulation is conducted by penetrating the thin-glass sheet to create the micro-holes in single point in the center of the thin-glass sheet. The generated netrin-1 gradient is expected could induce the axons' response to the single micro-hole position. (Chapter 2 and 3)

Next, the second manipulation is carried out by fabricating the micro-holes in multiple points over the thin-glass sheet. The multiple netrin-1 gradients generated from multiple micro-holes are responsible to realize the precise guided axon outgrowth to the nearest specific micro-hole. The axons' responses in both manipulations are investigated by measuring axon elongation and axonal angles toward the micro-holes. Based on the distance varieties of axons to the micro-holes, the axons' responses (*i.e.*, guided time, guided length, and axon outgrowth rate) dependent on the distances toward the micro-holes are also demonstrated. (Chapter 2 and 4)

Cell sorting attempt after single-cell manipulation is indispensable to gather more information, *e.g.*, biochemical and physiological studies to a single-cell level. Flow cytometry technology is employed to isolate floating cells in suspension using fluorescent probes, so the cells can only be used once during processing. Thus, continuous cell observation following the sorting cannot be achieved. Laser technology, *i.e.*, femtosecond laser, provides the sorting process with a high spatiotemporal resolution and effective absorption at the laser focal point, enabling precise cell elimination, *in situ* cell sorting, and multiple uses of isolated cells for further single-cell manipulation and analysis.[124] In the next experiment, a reverse cell sorting system is conducted by femtosecond laser scanning by detaching non-target cells to attain individual target cells. Immortalized megakaryocyte progenitor cell lines (imMKCLs) and the

myoblast cell line (C2C12) are used. The target cells are then cultured and continuously observed to verify their ability to proliferate (Chapter 2 and 5)

1.8 Thesis outline

This thesis consisted of six chapters, *i.e.*, general introduction, methods, guided axon outgrowth by molecular gradient generated from single-point and multiple-point femtosecond laser-fabricated micro-holes, reverse cell sorting by femtosecond laser scanning, and general conclusions **(Figure 10)**.

Chapter 1 General Introduction: In this chapter, several topics of single-cell analysis utilizing microfluidic devices and femtosecond laser were discussed, *i.e.*, the importance of single-cell analysis, single-cell behavior analysis, technology for single-cell analysis, microfluidic devices for single-cell analysis based on materials and methods, and femtosecond laser processing for single-cell analysis. In addition, the main manipulation of single-cell behavior in this thesis, *i.e.*, guided neurite and axon outgrowth, were described by various technologies.

Chapter 2 Methods: The chapter demonstrated the methods for regulating axon outgrowth by molecular gradient generated from laser-fabricated micro-holes and reverse cell sorting by femtosecond laser scanning. The methods for guiding axon outgrowth by molecular gradient consisted of the fabrication of microfluidic device, simulation of gradient generation for manipulation, experimental characterization of gradient generation for manipulation, culture of hippocampal neurons, femtosecond laser manipulation and time-lapse imaging, and quantification of neuron growth and statistical analysis. The methods for reverse cell sorting by femtosecond laser scanning composed of cell culture of immortalized megakaryocyte progenitor cell lines (imMKCLs) and the myoblast cell line (C2C12), femtosecond laser scanning and time-lapse imaging, and cell death assay.

Chapter 3 Guided Axon Outgrowth by Molecular Gradient Generated from Single-Point Femtosecond Laser-Fabricated Micro-holes: The chapter started with an introduction consisting of the importance of guided axon outgrowth, the problem caused by previous methods, the advantages of the femtosecond laser, and the regulation of guided axon outgrowth by the femtosecond laser pulse. Furthermore, the whole chapter comprised of design and principle of the microfluidic device, characterization of a single-molecular gradient for manipulation, single-point manipulation by femtosecond laser pulses, and guided axon outgrowth by guidance molecule released from a single point of micro-holes.

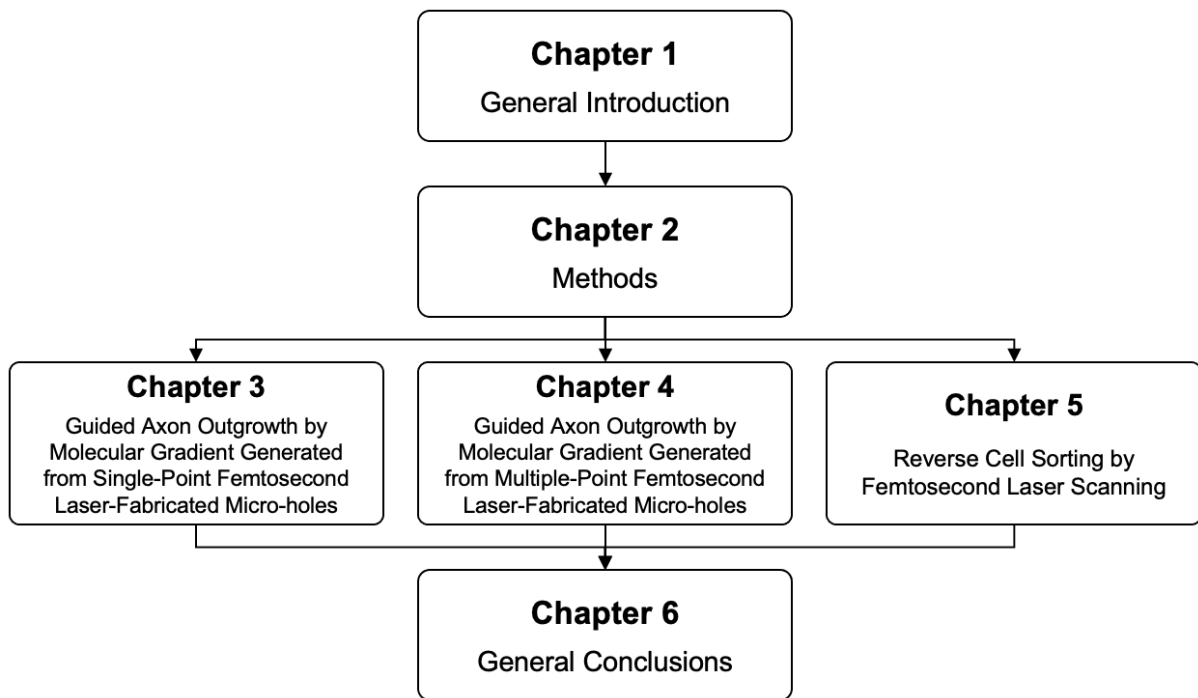**Chapter 4 Guided Axon Outgrowth by Molecular Gradient Generated from Multiple-Point Femtosecond Laser-Fabricated Micro-holes:** The chapter started with an introduction comprising of the importance of spatial control, previous methods for spatial control, and the use of femtosecond laser for spatial control to induce precise guided axon outgrowth. In sum, the chapter consisted of characterization of multiple-molecular gradients for manipulation, multiple-point manipulation by femtosecond laser pulses, guided axon outgrowth by guidance molecule released from multiple points of micro-holes, distance-dependent neuronal response to netrin-1, and comparison between single-point manipulation, multiple-point manipulation, and control groups.

Chapter 5 Reverse Cell Sorting by Femtosecond Laser Scanning: The chapter started with an introduction consisting of the importance of single-cell analysis, especially single-cell sorting, the challenges of other technologies for sorting individual cells from the culture substrate, the importance for sorting immortalized megakaryocyte progenitor cell lines (imMKLCs), and the advantages of femtosecond laser for cell sorting. In addition, the chapter discussed the system of reverse cell sorting by femtosecond laser scanning and the observation of cell proliferation ability following laser scanning.

Chapter 6 General Conclusions: The chapter presented the conclusions of the study and perspectives for future studies.

Figure 10. Flowchart of this study.

Chapter 2

Methods

Guided axon outgrowth by molecular gradient generated from femtosecond laser-fabricated micro-holes

2.1 Fabrication of microfluidic device

The microfluidic device in this study allowed the introduction of guidance molecules and real-time manipulation using femtosecond (fs) laser. The microfluidic device consisted of five layers from the bottom to the top. Layer 1 was a glass substrate (1 mm thickness) used as the basis of the microfluidic device. Layer 2 was a channel (1 mm depth and 3 mm width) for placing the guidance molecule (*i.e.*, netrin-1). Layer 3 was a thin-glass sheet (4 μm thickness and 4 mm width) used as a culture substrate and was penetrated by fs laser pulses to fabricate the micro-holes. Layer 4 were chambers (1 mm depth and 1 mm diameter) for confining the growth area of the cells and placing the medium. Layer 5 were PDMS slabs (1 mm thickness) placed opposite the chambers to prevent the outspread of the medium. Inlet and outlet were fabricated directly to connect with the channel **(Figure 11 (a))**. The thin-glass sheet was fabricated by weight-controlled load-assisted precise thermal stretching.[201] The chamber, channel, and PDMS slab were fabricated using standard soft lithography fabrication. All the compartments were bonded together by plasma treatment (Plasma Cleaner CY-P2L-B, China) to form a five-layered device **(Figure 11 (b, c))**. The device was then dry sterilized (AS-ONE SONW-300, Japan) at 160 °C for 1 h to prevent contamination.

## 2.2 Simulation of gradient generation for manipulation

Netrin-1 diffusion from the channel to the chamber via laser-fabricated micro-holes was simulated using the commercial finite element software COMSOL Multiphysics 5.4. The simulations were described in 2D and 3D models. In the chamber, there was no convection;

thus, the diffusion of netrin-1 from the channel to the chamber was described by diffusion equations:

$$\partial c / \partial t + \nabla \cdot (-D\nabla c) = 0$$

where t denoted time, c was the concentration, and D was the solute diffusion coefficient, and D in an aqueous culture medium was 2.36×10^{-12} m^2/s. Concentration boundary condition occurred in the channel, defined as c=c0, c0=1×10^{-5} mol/m^3. These were defined as no flux boundary conditions:

$$(-D\nabla c) \cdot n = 0$$
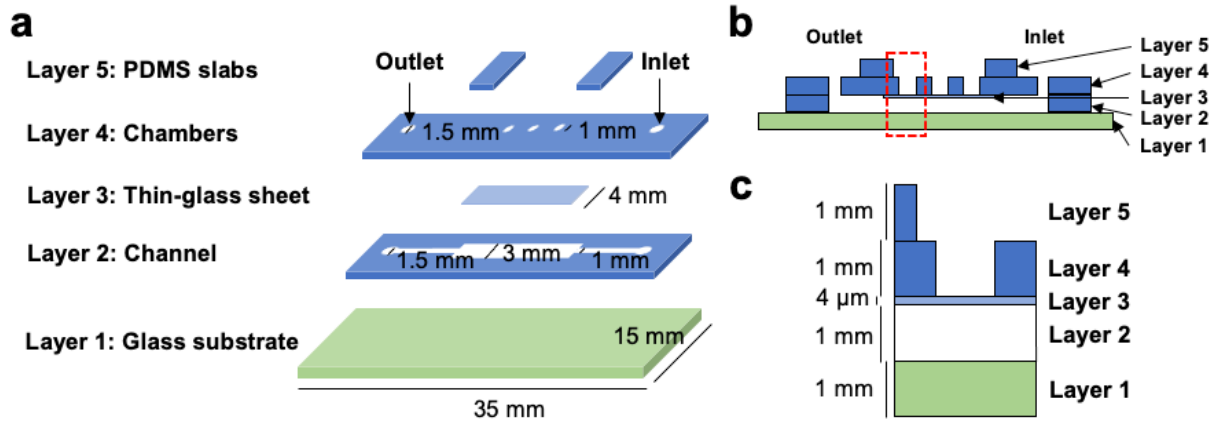
Figure 11. Schematic illustration of a microfluidic device for guiding axon outgrowth. (a) The 45-degree view of each layer of a microfluidic device. (b) A side view of a five-layered device. (c) A cross-sectional view of the dashed rectangle in (b) with the details of the thickness of each layer. The microfluidic device consists of five layers from the bottom to the top. Layer 1 is a glass substrate. Layer 2 is a channel for placing a guidance molecule. Layer 3 is a thin-glass sheet as a culture substrate for culturing the cells and is penetrated by the femtosecond laser pulse. Layer 4 chambers for placing the neurons and complete medium. Layer 5 is PDMS slabs for preventing the outspread of the medium.

2.3 Experimental characterization of gradient generation for manipulation

The diffusion netrin-1 from the channel to the chamber via laser-fabricated micro-holes was confirmed with bovine serum albumin (BSA) labeled Alexa Fluor 488 (Invitrogen, USA). Molecular weight of BSA (66.0 kDa) was similar to netrin-1 (68.2 kDa) which was expected to have a similar molecular gradient pattern. Alexa Fluor 488-BSA (5.33 μM; excitation wavelength (λ_{ex}) = 490 nm, emission wavelength (λ_{em}) = 525 nm) was introduced to the

channel of the device.[27] The device containing the molecule was placed on an inverted microscope (IX71, Olympus, Japan) equipped with a confocal laser-scanning system (FV300, Olympus) and maintained in an environmental chamber (37 °C, 5% CO_2). An amplified femtosecond laser pulse (Solstice-Ace; 800 nm, 150 fs, Spectra-Physics, USA) was focused and penetrated the thin-glass sheet through 10× objective lens (NA. 0.25, Olympus) to fabricate the micro-holes. The time-lapse imaging was conducted before (0 h) and after laser processing (1 – 16 h) by selecting the area of the thin-glass sheet. The fluorescence intensity shift of the Alexa Fluor 488-BSA in the chamber was evaluated by subtracting the fluorescence intensity value after laser processing (1 – 16 h) with the value before laser processing (0 h). The fluorescence intensity shift of the Alexa Fluor 488-BSA gradient was evaluated by subtracting the fluorescence intensity value at the micro-hole distance of 45 – 225 μm to the value at 0 μm.

2.4 Silanization of the thin-glass sheet surface

Silanization aims to change the charge of the thin-glass sheet from negative to positive with organosilane molecules. This process helps the attachment of the cells to the thin-glass sheet. Firstly, the microfluidic device was treated by plasma at 65 W for 2 min. The surface of the thin-glass sheet was silanized by coating with 2% 3-(2-aminoethylamino)propyldimethoxymethylsilane (Shin-Etsu Chemical Co., Japan) dissolved in pure water for 30 min. The organosilane solution was removed. The coated surface was then baked at 80 °C for 1 h to enhance the covalent bonding of the silanol groups. The surface was washed by pure water and 70% ethanol **(Figure 12 (a))**. Finally, the thin-glass sheet embedded in the microfluidic device was ready to be used as culture substrate.

2.5 Culture of hippocampal neurons

The silanized thin-glass sheet was coated with poly-D-lysine (PDL) (100 μg/mL) (Gibco, USA) and laminin (50 μg/mL) (Fujifilm Wako Pure Chemical Industries, Ltd, Japan). Hippocampal neurons isolated from embryonic day 16 (E16) mice were provided by the Division of Biological Science, Nara Institute of Science and Technology, Japan. The neurons were seeded on the laminin-coated thin-glass sheet with a cell density of 2.0×10^4 cells/cm^2. The neurons were cultured in a plate out medium containing Neurobasal (Gibco), 10% fetal bovine serum (FBS) (Gibco), and penicillin (100 units/mL) – streptomycin (100 μg/mL). After 3 h, the medium was changed into a complete medium containing Neurobasal, 2% B-27 supplement (50×) (Gibco), penicillin (100 units/mL) – streptomycin (100 μg/mL). The neurons were cultured in the incubator (37 °C, 5% CO$_2$) for 1 day *in vitro* (DIV) **(Figure 12 (b))**.
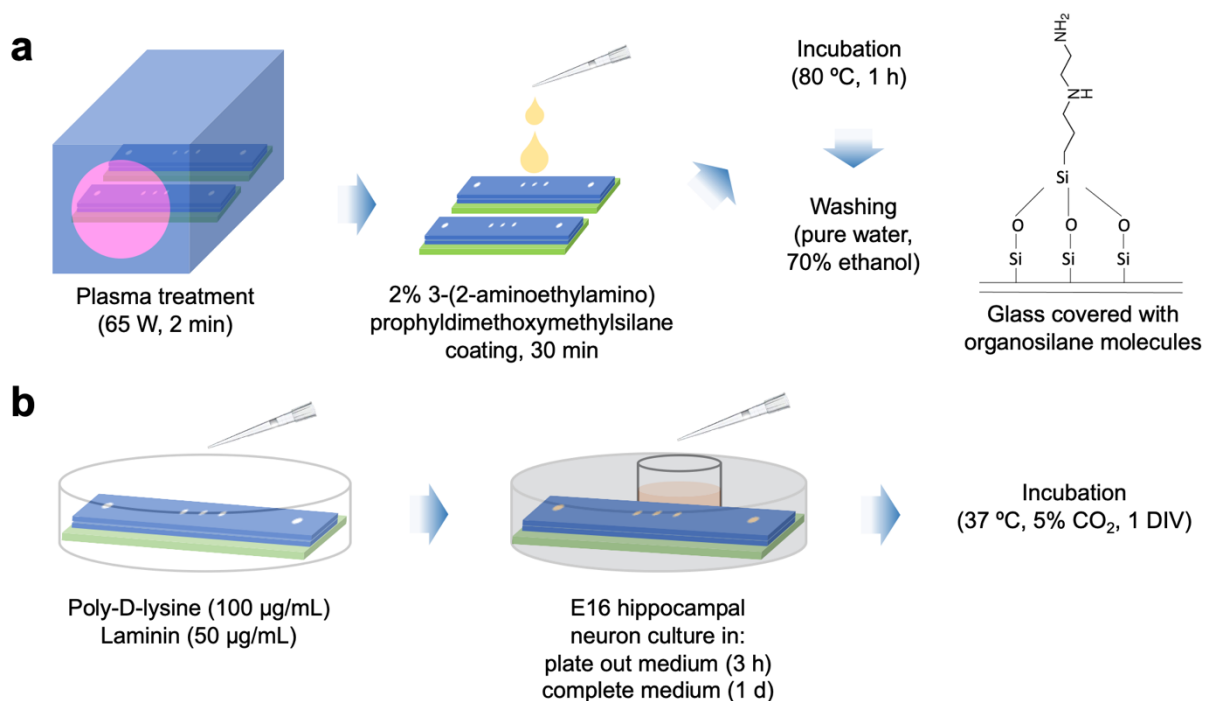
Figure 12. Silanization of the thin-glass sheet surface and neuronal culture on the microfluidic device. (a) Silanization is carried out by plasma treatment, coating the surface of a thin-glass sheet with a silane solution, incubation, and washing. (b) Neuronal culture is performed by firstly coating the silanized thin-glass sheet with poly-D-lysine and laminin. The neurons are seeded and cultured on the thin-glass sheet with a medium and incubated for 1 day *in vitro* (DIV).

2.6 Femtosecond laser manipulation and time-lapse imaging

Before the actuation, netrin-1 (800 ng/mL; Funakoshi, Japan) was introduced to the channel manually using a micropipette via the inlet. The device containing cultured cells and guidance molecules was placed on an inverted microscope and maintained in an environmental chamber (37 °C, 5% CO_2). An amplified femtosecond laser pulse (Solstice-Ace; 800 nm, 150 fs, Spectra-Physics, USA) irradiated the thin-glass sheet through a 10× objective lens (0.25 NA). The frequency and power of 1 kHz and 5.3 J/cm, respectively, were used for fabricating the micro-holes on the thin-glass sheet.[94,95] The micro-holes were fabricated for two experimental schemes, *i.e.*, in single point (center) of the thin-glass sheet and multiple points over the thin-glass sheet. The response of neurons to the netrin-1 gradient was observed with time-lapse imaging every 10 min using a confocal microscope equipped with a CCD camera (Teli CS3330B), a 10× objective lens, and FLUOVIEW software **(Figure 13)**.
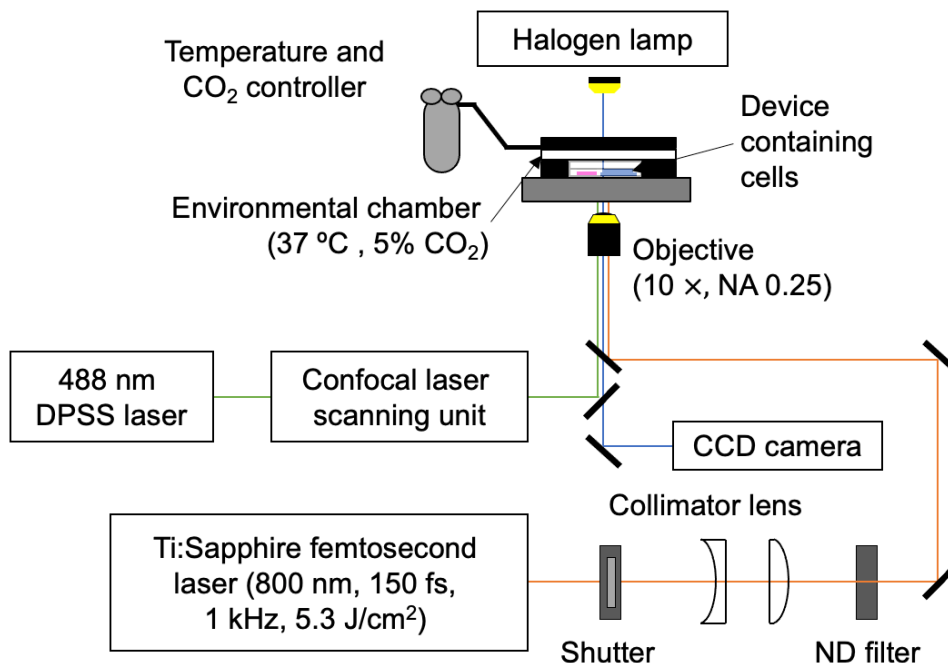
Figure 13. Schematic illustration of femtosecond laser processing and time-lapse imaging.

2.7 Quantification of neuron growth and statistical analysis

The time-lapse pictures of axon elongation and axonal angle were measured using ImageJ software (Version 1.52q). Guided axon outgrowth is the axon elongation that grows farthest toward the micro-holes at a specific time. Axonal angle is the axonal endpoint angle towards the micro-holes. Axonal angular change/alternation is the subtraction of axonal angle before and during netrin-1 exposure. The positive and negative values indicate that the axon is guided towards and away from micro-holes, respectively. Independent *t*-test was performed to compare: 1) axon elongation between experimental groups, 2) axonal angles higher and lower than the average turning angle, and 3) guided axon timing, guided axon length, and axon outgrowth rate dependency on axon-to-micro-hole distance.

Reverse cell sorting by femtosecond laser scanning

2.8 Cell culture

2.8.1 Immortalized megakaryocyte progenitor cell lines (imMKCLs)

The imMKCLs were cultured as previously described.[202] To immobilize the imMKCLs, cells were seeded on the Matrigel (Corning, USA) coated glass-bottom dish with grids (AGC, Japan).

2.8.2 The myoblast cell line (C2C12)

The C2C12 was obtained from the RIKEN Cell Bank (Tsukuba, Japan). The cells were seeded on the glass-bottom dish with a cell density of 1.5×10^3 cells/cm^2 and cultured in DMEM high glucose (Gibco, USA), 10% fetal bovine serum (Gibco), and penicillin (100 units/mL) – streptomycin (100 µg/mL) (Gibco) under CO_2 (5%) and saturated vapor at 37 °C for 1 day *in vitro* (DIV).

2.9 Femtosecond laser scanning and time-lapse imaging

The glass-bottom dish containing cultured cells was placed on an inverted microscope (IX71, Olympus, Japan) equipped with a confocal laser-scanning system (FV300, Olympus) and maintained in an environmental chamber (37 °C, 5% CO_2). An amplified femtosecond laser pulse (Solstice-Ace; 800 nm, 150 fs, Spectra-Physics, USA) was focused and scanned on the non-target cells through a 10× objective lens (NA. 0.25, Olympus). The repetition rate and pulse energy of the laser were 1 kHz and 135 nJ/pulse, respectively. The laser scanning speed was 0.03 mm/s. The laser scanning was performed until all non-target cells died, as indicated by the detachment of cells from the culture substrate and the rupture of the intact cells into cell debris. The behavior of the target cells was observed with time-lapse imaging every minute using a digital inverted microscope equipped with a color CMOS camera, a transmitted white LED, and a 4× objective lens (WSL-1800 CytoWatcher, Atto, Japan).

2.10 Cell death assay

To ensure that the non-target cells died after the laser scanning, a propidium iodide (PI) assay was performed. PI is a membrane-impermeable fluorescence molecule that binds to the DNA structure. The non-viable cells become permeable when their membranes become damaged. Thus, the non-viable cells were stained in bright red, particularly in their nucleus containing the DNA structure. PI solution (0.075 mM; λ_{ex} = 535 nm, λ_{em} = 617 nm) (Dojindo Laboratories, Japan) was added to the 100 μL of culture medium containing cells, followed by incubation in a dark room for 20 min. After the incubation, the fluorescence signal was detected using a confocal fluorescence microscope with an excitation wavelength of 532 nm.

Chapter 3

Guided Axon Outgrowth by Molecular Gradient Generated from Single-Point Femtosecond Laser-Fabricated Micro-holes

3.1 Introduction

The study of guided axon outgrowth is essential in neuroscience, both *in vitro* and *in vivo*. In *in vitro* study, the guidance molecule regulates guided axon outgrowth to establish neuronal network formation. Dysregulation between guidance cues, signaling pathways, and cell receptors could lead to non-functional synaptic connections, resulting in the failure of neuronal homeostasis.[157–159] In clinical study, cell transplantation is the current gold standard for treating brain injuries, especially those identified by large lesions, such as traumatic brain injury, spinal cord injury, and stroke.[160–166] However, after the transplantation of cells alone, neuronal regeneration remains one of the greatest challenges, as identified by poor cell survival, differentiation, and axonal integration.[167–170] Precise axonal integration to form functional synapses is the ultimate goal to obtain functional recovery after brain injury.[171,172] Transplantation of guided neurons on the scaffold has been reported, which can increase cell survival, axon outgrowth, neuronal tissue reconstitution, and decrease inflammation.[167–170] Therefore, the systems to develop guided axon outgrowth on the scaffold are necessary to explain detailed mechanisms of neuronal communication and further induce axonal integration to promote functional recovery after brain injury.

In aligning the neurite and axon outgrowth on the scaffolds, previous technologies, *i.e.*, electrospinning, micropatterning, and 3D printing are carried out by developing the scaffolds first and followed by the cell culture.[25,26,177,180–184,187,193,195] Due to the indirect process of scaffold fabrication and cell culture using these technologies, the actual cell behaviors during the manipulation cannot be observed. In addition, the clinical attempts using these technologies still face difficulties in forming precise axonal integration between transplant and host neurons

to establish functional synapses. Therefore, it calls for a high-precision tool with spatiotemporal resolution to regulate guided axon outgrowth in real-time conditions to achieve robust axon regeneration and promote functional recovery following brain injury. Based on numerous advantageous characteristics of femtosecond (fs) laser, such as offering spatiotemporal resolution,[92,154,155] producing lower heat production and less collateral tissue damage than other pulsed lasers,[153] the fs laser has been used as a powerful tool to precisely regulate neurite outgrowth.[144,151,203] In addition, the incorporation of the microfluidic device has also been reported can increase the effectiveness and reliability of observation.[177,197,198]

In this study, the fs laser and microfluidic device approaches were integrated to enable real-time manipulation for regulating axon outgrowth on a 4 μm thick thin-glass embedded in a microfluidic device. The thin-glass sheet was applied as a culture substrate with the advantages of uniform surface profile and surface roughness.[201] In addition, the thin-glass sheet was also easy to cut and penetrate with a fs laser.[98] Hippocampal neurons isolated from embryonic day 16 (E16) mice were cultured on the thin-glass sheet for 1 day *in vitro* (DIV), while the axon guidance molecule (*i.e.*, netrin-1)[199,200] was manually introduced to the channel. The micro-hole fabrication was conducted in single point in the center of the thin-glass sheet. The netrin-1 diffused and generated a radial concentration on the thin-glass sheet via the micro-holes, inducing the elongation and outgrowth of axons of neurons **(Figure 14)**. The axons showed accelerated elongation toward the micro-holes during netrin-1 exposure. Moreover, a majority of axons were guided toward the netrin-1 gradient, indicated by narrower axonal angular changes during exposure to netrin-1. These results demonstrated that the developed system is capable of controlling guided axon outgrowth precisely in real-time conditions.
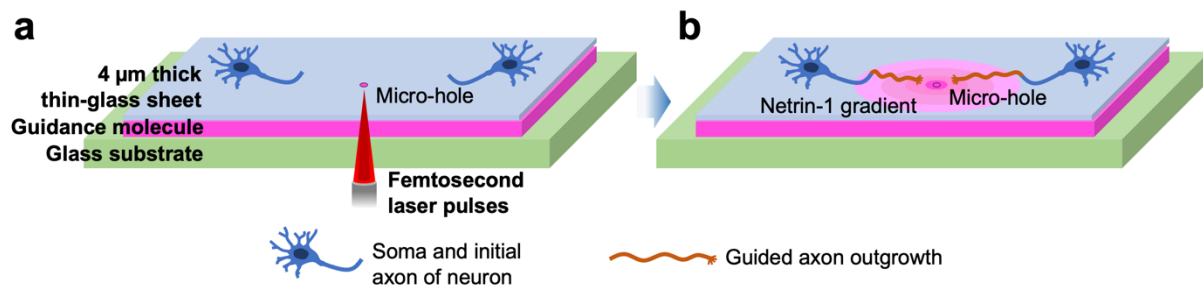
Figure 14. Schematic illustration of guidance of axon outgrowth of neurons by a single point molecular gradient (netrin-1 gradient) released from femtosecond laser-fabricated micro-holes. (a) The femtosecond laser pulse irradiates the thin-glass sheet to fabricate the micro-hole. (b) The molecule releases and generates a gradient on a thin-glass sheet, inducing the outgrowth of axons toward the micro-hole.

3.2 Design and principle of the microfluidic device

The microfluidic device enables the embedded of culture substrate (*i.e.*, 4 µm thick thin-glass sheet) penetrated by fs laser pulses to generate a simple diffusion process of a guidance molecule (*i.e.*, netrin-1) from the channel to the chamber. The microfluidic device was comprised of five layers from the bottom to the top, *i.e.*, a glass substrate, a channel, a thin-glass sheet, chambers and PDMS slabs. The width of the channel and the chamber were 3 mm and 1 mm, respectively, allowing the thin-glass sheet (4 mm width) to separate the upper compartment for performing cell culture and the below compartment for placing the guidance molecule. The chamber with a diameter of 1 mm was fabricated to confine the growth area of the cells on a thin-glass sheet. This limited growth area was convenient for observing cell behaviors in a single field of view microscope. The depth of the chamber and the PDMS slab were 1 mm and 1 mm, respectively. The total depth of both layers was sufficiently high (2 mm in total) to retain the medium amount in a microfluidic device **(Figure 15 (a))**. For long-term cell culture, a five-layered device was placed inside a culture dish equipped with a dish containing medium and a wet paper **(Figure 15 (b))**. This setup can maintain cell culture in a stable pH medium without evaporation for up to 7 DIV.
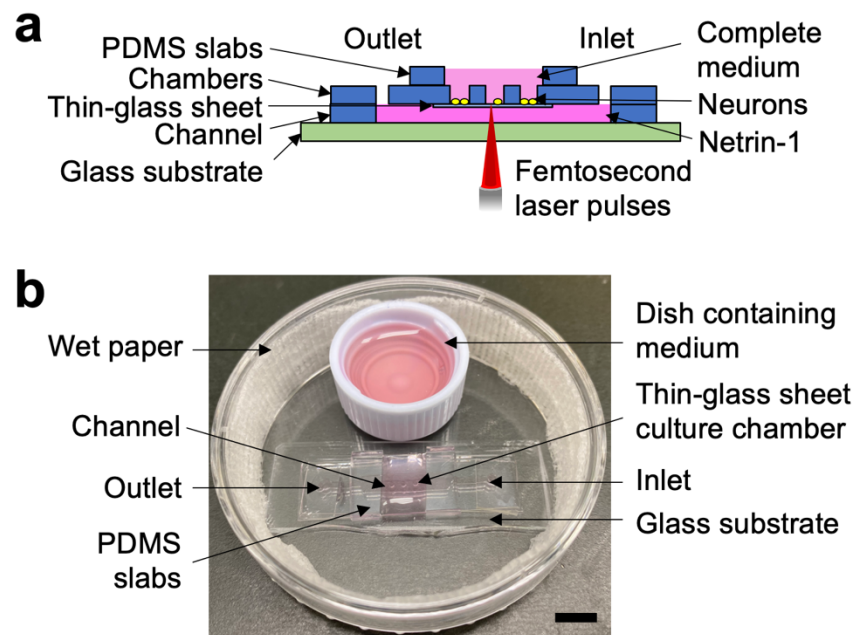
Figure 15. A microfluidic device for guiding axon outgrowth of neurons. (a) A side view of a microfluidic device consisting of a guidance molecule (*i.e.*, netrin-1), neurons, and a complete medium. (b) The microfluidic device is placed inside the culture dish equipped with a dish containing medium and a wet paper to prevent medium evaporation. The scale bar is 5 mm.

3.3 Characterization of a single-molecular gradient for manipulation

To characterize molecular gradient in the microfluidic device, the finite element method simulation was performed to model the diffusion pattern of the guidance molecule released from laser-fabricated micro-holes over time. The micro-holes were fabricated in the center point of the thin-glass sheet for single-point molecular gradient. The guidance molecule diffused and generated a gradient from single-point laser-fabricated micro-holes with a radial concentration over time **(Figure 16 (a))**. In addition, the molecule was continuously released from the channel to the chamber via micro-holes with a saturation concentration after 8 h **(Figure 16 (b, c))**.

In parallel, the experimental characterization of the netrin-1 gradient was also conducted. Alexa Fluor 488-BSA was used to confirm concentration profiling of netrin-1. The surface of the thin-glass sheet was selected as the focused area to observe fluorescence intensity changes, representing the location of the axon outgrowth responses to the molecular gradient **(Figure 17 (a))**. The Alexa Fluor 488-BSA was introduced to the channel located on the below side of the

focused area, defining reference fluorescence for measurements. The fluorescence intensity was continuously taken from 1 to 16 h after laser processing. The molecule released from the center point of the micro-holes on the thin-glass sheet. The fluorescence intensity increased by 8 h and was followed by a plateau **(Figure 17 (b))**. The molecule diffused and generated a gradient from the point near (0 μm) to far from the micro-holes (225 μm) **(Figure 17 (c))**. The fluorescence intensity shift of the gradient decreased over time **(Figure 17 (d))**, indicating the saturated concentration of the molecule at the final time point of observation. The series of results show the capability of the microfluidic device with fs laser pulses for generating a gradient (from 0 to 8 h) to induce guided axon outgrowth.
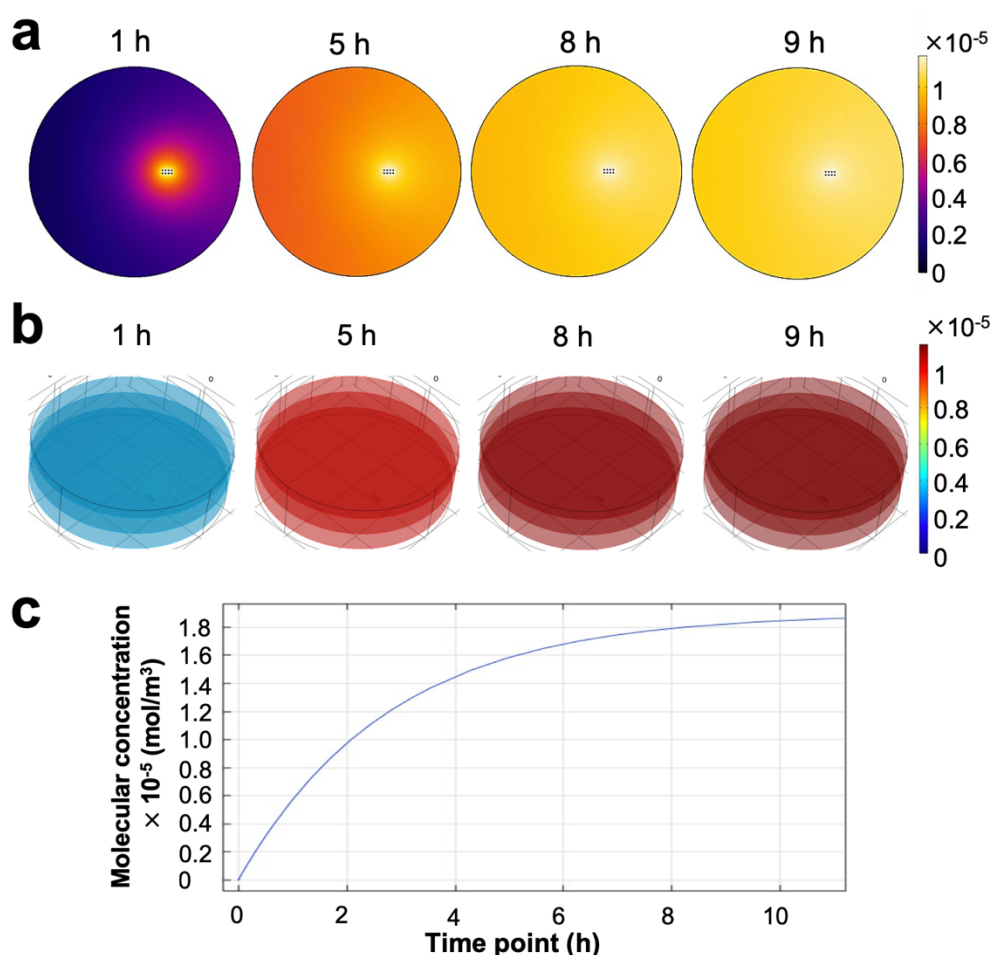
Figure 16. Simulation of a single-point molecular gradient. (a and b) 2D (a) and 3D diffusion simulation of a molecular gradient from single-point micro-holes in the center of the thin-glass sheet over time (b). (c) Molecular concentration from 3D simulation in the chamber of the device over time. The saturation concentration is indicated after 8 h.
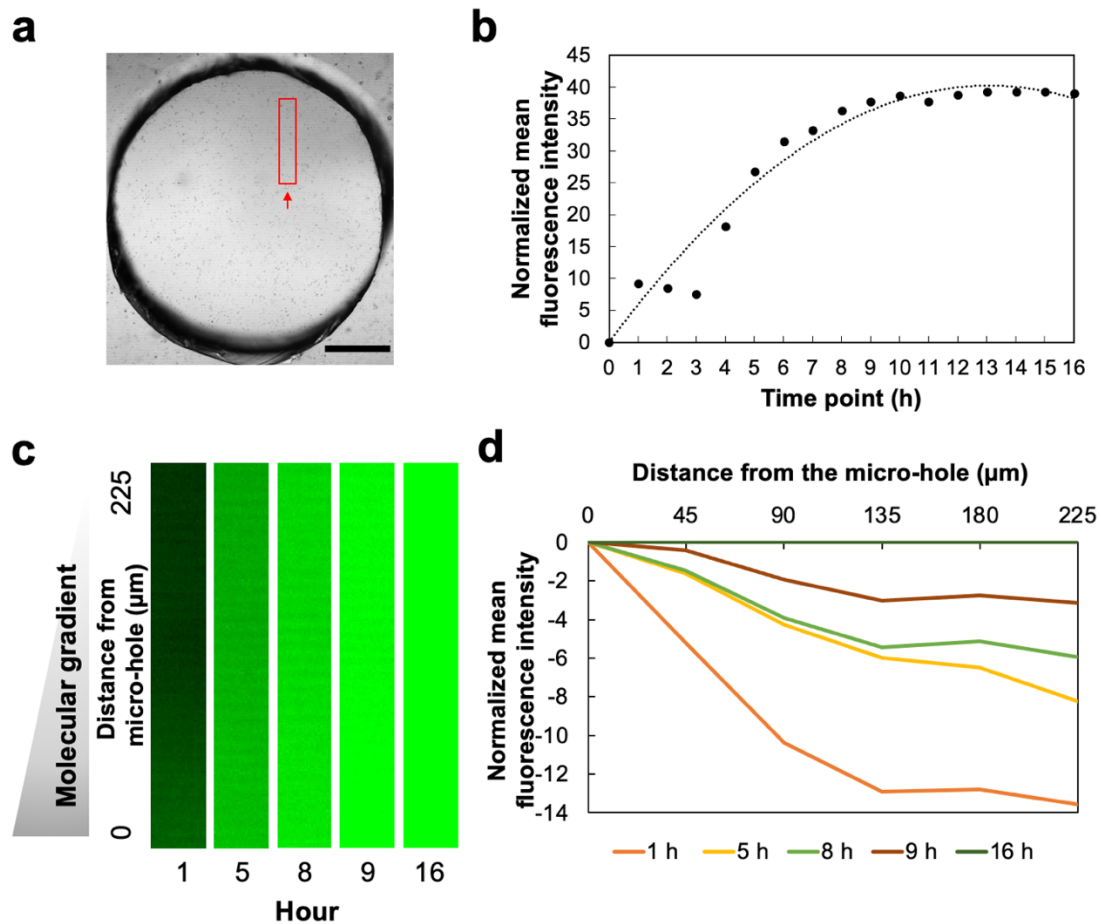
Figure 17. Experimental characterization of a single-point molecular gradient. (a) The surface of a thin-glass sheet in the chamber that is selected as the focused area of fluorescence intensity changes. The red arrow is micro-hole position. The red rectangle is the observed area for molecular gradient changes. (b) Fluorescence intensity shift in the chamber for 16 h from single-point laser-fabricated micro-holes. (c) Fluorescence images of a molecular gradient from a red rectangle in (a) from the distance of 0 – 225 μm to the micro-holes over time. (d) Fluorescence intensity shift of a molecular gradient across the field. The scale bar is 200 μm.

3.4 Single-point manipulation by femtosecond laser pulses

This study is the first to utilize a 4 μm thick thin-glass sheet as a culture substrate for hippocampal neurons. The 4 μm thick thin-glass sheet was used as a culture substrate for the cells. The 4 μm thick thin-glass sheet has recognized as the thinnest glass with high transparency, which is beneficial for use as a culture substrate actuated by laser technology **(Figure 18 (a))**. The extracellular matrix (*i.e.*, laminin) was coated on the thin-glass sheet surface for the cell scaffold. Neurons adhered to the thin-glass sheet surface at 3 h after cell

seeding, then started to project their axons at 1 DIV. The state of growth was suitable for actuation by fs laser to prevent cell detachment.

A real-time actuating system by fs laser pulses was performed by irradiating the point on the thin-glass sheet during cell culture. The center point of the thin-glass sheet was penetrated to create the micro-holes to induce the response of hippocampal neurons **(Figure 18 (b))**. Various laser energy densities were examined to obtain a short-time laser processing and minimal water bubble generation to prevent cell interferences. The laser energy density of 5.3 J/cm^2 was successful in fabricating the micro-holes with a short-time laser penetration (*i.e.*, 2 – 8 s per micro-hole) and minimal water bubble generation. The fabrication conditions with 5.3 J/cm^2 fs laser did not affect cell detachment and damage **(Figure 18 (c))**.
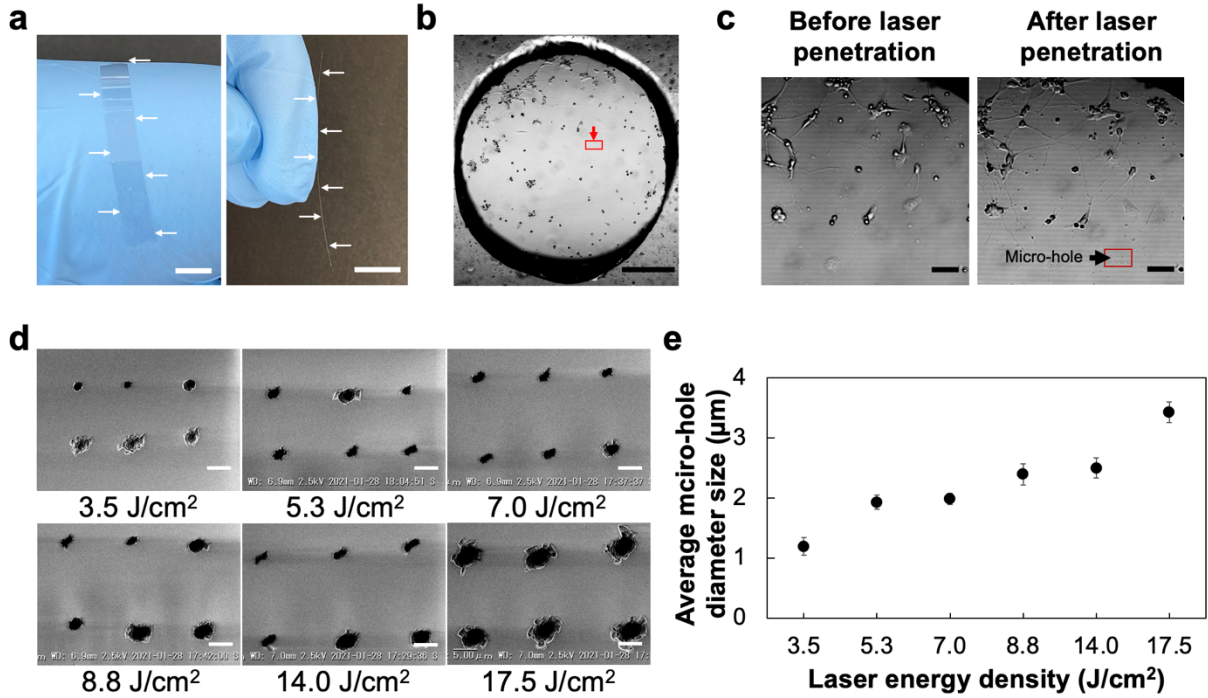
Figure 18. A real-time manipulation system by femtosecond (fs) laser pulses to fabricate micro-holes on a 4 μm thick thin-glass sheet and scanning electron microscopy (SEM) observation of laser-fabricated micro-holes. (a) A top (left) and side view of the thin-glass sheet (right) showing its ultra-thin thickness. (b) A photomicrograph of the 1 DIV neuronal culture. The red rectangle indicates the laser-fabricated micro-holes. (c) Photomicrographs before (left) and after laser processing (right). (d) A top view of SEM images of laser-fabricated micro-holes on the thin-glass sheet by different energy densities. (e) Laser energy density dependency on the laser-fabricated micro-hole diameter of the thin-glass sheet by different energy densities. Values are shown as means ± SE. Scale bars are 5 mm (a), 200 μm (b), 50 μm (c), and 5 μm (d).

Scanning electron microscopy (SEM) images confirmed the diameter of the micro-holes fabricated using laser energy density of 5.3 J/cm^2 ranging from 1.11 to 2.75 µm. Furthermore, SEM observations were also carried out to investigate the diameter of the micro-holes fabricated with different laser energy densities **(Figure 18 (d))**. Micro-hole diameter averages were: 1.19 ± 0.51, 1.93 ± 0.40, 1.98 ± 0.31, 2.39 ± 0.60, 2.50 ± 0.56, and 3.42 ± 0.51 µm, when the laser energy densities were 3.5, 5.3, 7.0, 8.8, 14.0, and 17.5 J/cm^2, respectively **(Figure 18 (e))**. The SEM analysis reveals that micro-hole diameter increased with the increase of the laser energy density.

3.5 Guided axon outgrowth by netrin-1 released from a single point of micro-holes

After demonstrating the capability for generating molecular gradients, the device was utilized to regulate axon outgrowth of the primary culture of hippocampal neurons by an axon guidance molecule (*i.e.*, netrin-1) released from the center point of micro-holes. Through the micro-holes fabricated by fs laser pulses in the center of the thin-glass sheet, netrin-1 was released and distributed throughout the chamber over time. The freely projected axons with varying distances to the netrin-1 source (micro-holes) were investigated before and after laser processing. Guided axon outgrowth is the axon elongation that grows farthest toward the micro-holes at a specific time. The initial axons located at 84 – 292 µm to the micro-holes showed guided axon outgrowth, identified by the axon elongations toward the micro-holes. Otherwise, initial axons at distance greater than 292 µm showed the projection away from the micro-holes **(Figure 19 (a))**. The axon outgrowth rate during exposure to the netrin-1 was 25.5 µm/h.
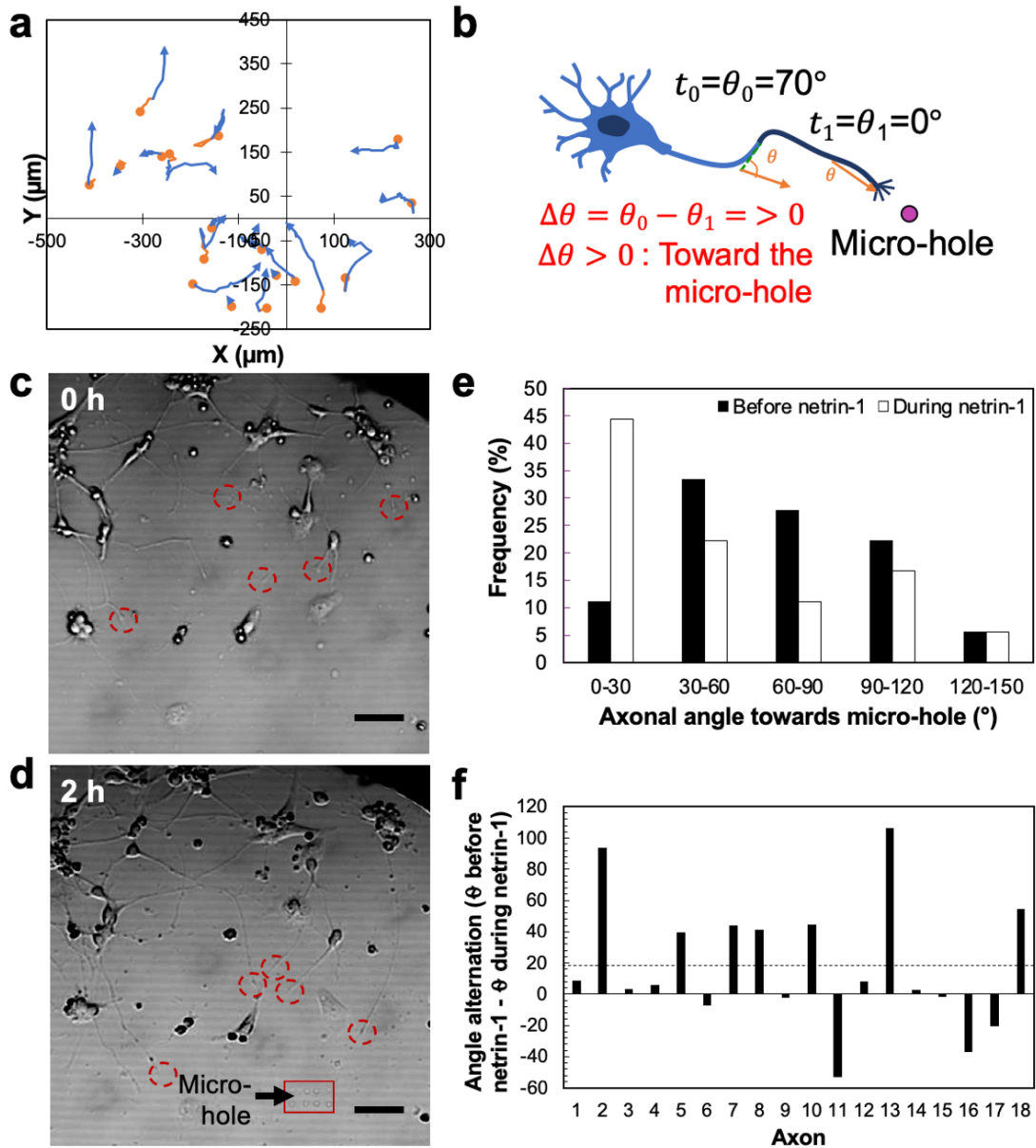
Figure 19. Response of neurons to netrin-1 released from a single point of micro-holes. (a) Axon trajectories of neuronal culture with netrin-1 gradients generated from laser-fabricated micro-holes in the center of the thin-glass sheet during 8 h exposure to netrin-1. The micro-holes are normalized at (x = 0 μm and y = 0 μm). The initial axons are normalized with the position of the micro-holes. (b) Schematic illustration of the angular change ($\Delta\theta$) of the initial axonal angle (θ_0) before micro-hole fabrication (t_0) with axon outgrowth angle (θ_1) after micro-hole fabrication (t_1). (c, d) Photomicrographs of initial axons before netrin-1 exposure (c) and axon outgrowth at 2 h exposure to netrin-1 (d), showing guided axon outgrowth towards the micro-holes. (e) Frequency of axonal angle distribution towards the micro-holes before and during exposure to netrin-1. (f) Angular change of axons before and during exposure to netrin-1. The dashed line represents the mean angle of turning (18.4°) (Upper and lower values from the average turning angle, $p < 0.05$, independent t-test, n = 18). Scale bars are 50 μm.

To further determine whether neurons responded to the netrin-1 source, angular change and angle distribution of axons were evaluated. Angular changes were analyzed by subtracting angles of axonal endpoints toward the micro-holes before and during exposure to netrin-1. The positive angular change indicated that the axon guided towards the micro-holes **(Figure 19 (b))**. The observed axons had varying angles, identified at angles from 0° to 150° toward the micro-holes, with high percentage axons at angles of ≤ 60°, ≤ 90°, and ≤ 120° **(Figure 19 (c, e))**. After the laser processing, guided axon outgrowth to the netrin-1 source was investigated at different time points depending on the first time point of axons to grow farthest toward the micro-holes, resulting in higher percentage of axons at angle of ≤ 30° and lower percentage at angles of ≤ 60°, ≤ 90°, and ≤ 120° **(Figure 19 (d, e))**. However, few axons turned away from the micro-holes, indicated by higher percentage axons at angle of ≤ 150° during exposure to netrin-1.

The mean of axonal angular change during exposure to netrin-1 was 18.4°. Based on this average, 12 out of 18 axons (67%) were guided toward the micro-holes, indicated as positive angular changes: 7 axons turned more than the average value (toward the micro-holes), 5 axons with positive angular changes less than the average value (toward the micro-holes), and the remaining 6 axons with negative angular changes (away from the micro-holes) **(Figure 19 (f))**. These results showed that the axons responded to the single-point netrin-1 source and demonstrated the reliability of the system for regulating guided axon outgrowth following the fabrication of micro-holes by fs laser.

3.6 Discussion

Real-time actuation for controlling axon outgrowth enabled by guidance molecule released from fs laser-fabricated micro-holes on a 4 μm thick thin-glass sheet was demonstrated. The real-time actuation was achieved by penetrating the thin-glass sheet using fs laser during cell

culture in a microfluidic device. The microfluidic device was designed without geometric limitations (*e.g.*, microchannel arrays and asymmetric channels),[174,178,204] allowing free and random cell growth on the culture substrate. Thus, the device relied solely on the generated radial concentration of molecular gradients by laser-fabricated micro-holes, inducing cell responses toward the gradients **(Figure 16 (a))**. Radial concentrations were identified as a typical pattern for local actuating systems, such as micropipette-based chemotactic assay and implant-based drug delivery.[205,206] Unlike other microfluidic devices that utilize fluidic controllers (*e.g.*, pumps and valves) to generate fluid flow,[207–211] this device enabled the diffusion of guidance molecule from the channel to the chamber via laser-fabricated micro-holes without any concerns of fluid flow-induced cell interferences.

This study is the first to show cell behavior responses of hippocampal neurons toward the guidance molecules released from laser-fabricated micro-holes. The gradient of netrin-1 with concentrations ranging from 5 to 1000 ng/mL has been demonstrated to extend axon outgrowth.[27,198,212–218] In this study, the released netrin-1 from the channel to the chamber affected increased axon elongation of the hippocampal neurons at a particular time point. The mean axon outgrowth rate (*i.e.*, 25.5 μm/h) was comparable to other experiments with a threefold extension from their soma.[197,198,212]

Apart from the role of netrin-1 to promote axon outgrowth rate of neurons, netrin-1 has been known to organize guided axon outgrowth on various scaffolds in soluble and scaffold-attached form.[27,216,217,219–221] In soluble form, netrin-1 is introduced in a one-sided manifold to control axon outgrowth.[27,216,217] In scaffold-attached form, netrin-1 is immobilized in a scaffold to form a topographic gradient to guide the outgrowth of axons.[220,221] Unlike those systems, this chapter achieved local actuation activated by a single point of micro-holes generated molecule gradients to induce guided axon outgrowth. Most axons were guided toward the netrin-1, as indicated by narrower axonal angles and positive axonal angular changes during 2 – 8 h

exposure to the netrin-1 gradient **(Figure 19 (e, f))**. The guidance effect of netrin-1 was in accordance with the release and generation of netrin-1 gradient from 0 to 8 h **(Figure 16 (c), 17 (b))**.

3.7 Conclusions

The combination of the femtosecond laser and microfluidic device could achieve guided axon outgrowth with non-invasive and real-time actuation. The femtosecond laser setup facilitated the controllable system to fabricate micro-holes, generating the slow stream of molecules to induce the growth of slow-response cells, especially neurons. The microfluidic device enabled the storing of guidance molecule that is important for real-time actuation of cell behaviors, *i.e.*, guided axon outgrowth. Moreover, manual introduction of the solution in the microfluidic device prevented shear stress-induced cell interferences, which was beneficial in gathering reliable cellular information. The 4 μm thick thin-glass sheet embedded in a microfluidic device enabled the simple process of extracellular matrix coating, which was useful as a culture substrate for neurons. The ultra-thin thickness of the glass allowed short-time actuation by laser technology, providing non-invasive cell manipulation. Also, the low opacity of the thin-glass sheet improved the accuracy of laser actuation and increased the resolution for observing adherent cells. Based on these favorable characteristics, this system can be applied to investigate other cell types for different experimental purposes, *e.g.*, neural regeneration, immune cell response, stem cell differentiation, cancer cell proliferation, wound healing process, and other biological phenomena.

Chapter 4

Guided Axon Outgrowth by Molecular Gradient Generated from Multiple-Point Femtosecond Laser-Fabricated Micro-holes

4.1 Introduction

The previous chapter investigated the single-cell behavior (*i.e.*, guided axon outgrowth) of individual neurons by single-point laser-fabricated micro-holes. In this chapter, guidance of axon outgrowth to the specific point of micro-holes was conducted, realizing the precise manipulation at a single-cell level. The study of spatial control in neuroscience is critical to induce established neuronal networks. Spatial control to guide axon outgrowth enables to manipulate and observe neuronal behavior responses toward varied locations.

In previous studies, spatial control to regulate axon outgrowth can be achieved by using electrospinning and micropatterning technology based on the geometric cue.[26,191–193,222,223] However, these approaches require integrated equipment and complicated steps. In other studies, the near-infrared (NIR) laser beam has been utilized to regulate axon outgrowth of rat hippocampal and cortical neurons. Using its spatial resolution, the laser can generate localized microscopic temperature increase that plays a role as guidance and repulsive cue to direct axon outgrowth towards and away from the cue, respectively.[224,225] These approaches use thermal cues with the temperature condition of 40 – 43 ºC, which may display cellular and subcellular changes as well as cell damage. In addition, critical parameters and biological mechanisms governed by these physical cues remain indefinable.

This study used a chemical cue to control axon outgrowth by incorporating a femtosecond (fs) laser and a microfluidic device. The design of the microfluidic device was similar with the previous chapter. To realize the spatial control, the thin-glass sheet was irradiated by the fs laser to create multiple micro-holes nearby the projected axons. The netrin-1 diffused and generated multiple radial concentrations on the thin-glass sheet via the micro-holes, influencing the

elongation and guidance of axons toward the nearest micro-hole **(Figure 20)**. The projected axons nearest the micro-holes experienced narrower axonal turning toward the micro-holes during netrin-1 exposure. Eventually, axon responses, such as guided time, guided axon length, and axon outgrowth rate, depended on the distances of initial axons toward the molecular sources. These results demonstrated that the fs laser could precisely manipulate guided axon outgrowth to the nearest specific micro-hole in a microfluidic device.
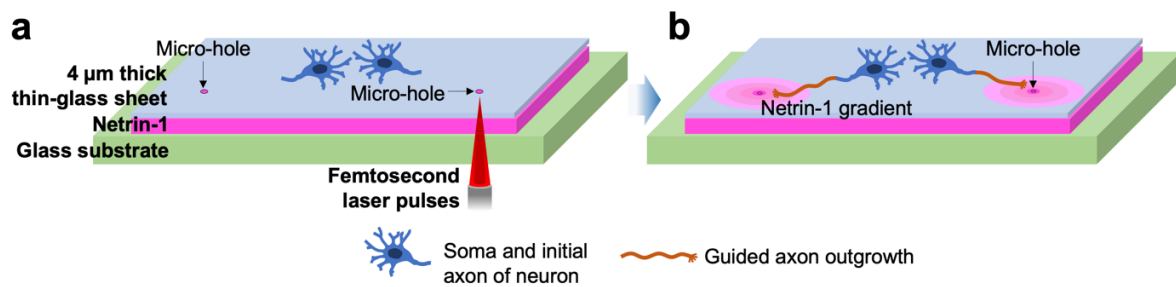
Figure 20. Schematic illustration of guided axon outgrowth of neurons toward multiple points of molecular gradients by a femtosecond laser. (a) Multiple points of micro-holes are fabricated by femtosecond laser pulses. (b) Multiple molecular gradients are generated via the micro-holes to induce guided axon outgrowth to the nearest micro-hole.

4.2 Characterization of multiple-molecular gradients for manipulation

To characterize multiple-molecular gradients generated from multiple points of micro-holes, finite element method simulation and experimental characterization of netrin-1 gradients were conducted. The micro-holes were fabricated near the freely projected axons with a total of 9 micro-holes. The multiple gradients were generated starting from the points near the micro-holes with radial concentrations **(Figure 21 (a))**. The guidance molecule was continuously diffused from the channel to the chamber via micro-holes with a saturation concentration after 8 h **(Figure 21 (b, c))**.
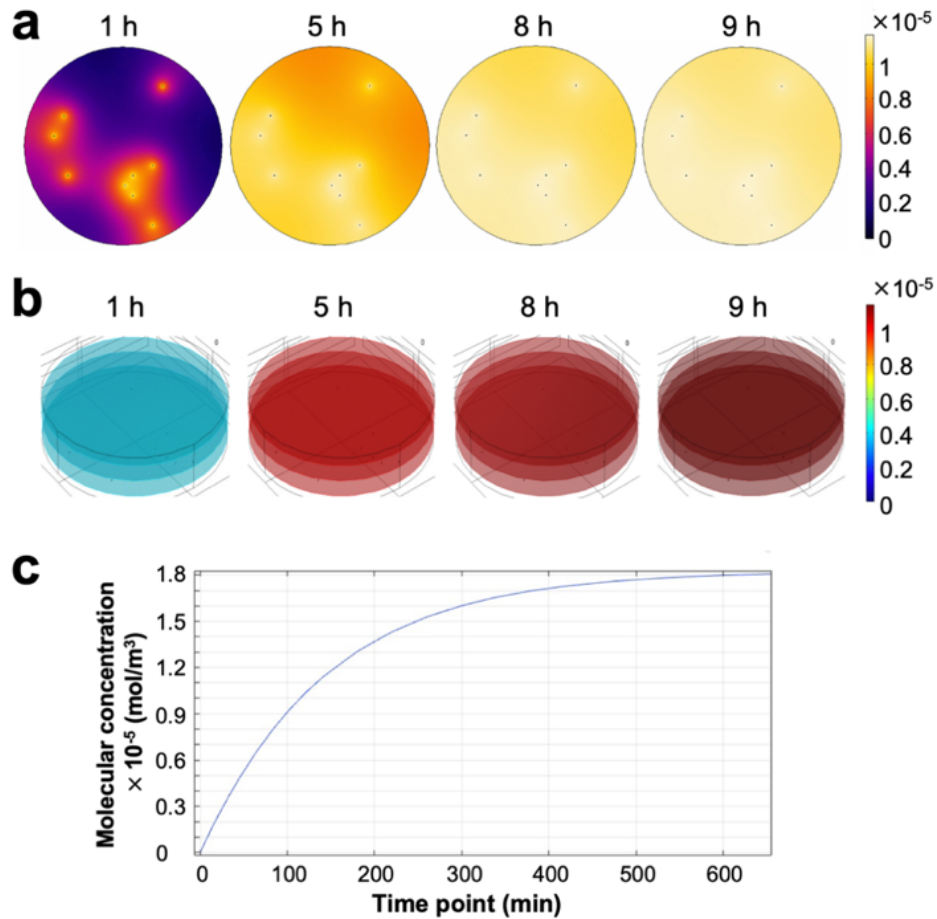
Figure 21. Simulation of multiple points of molecular gradients. (a and b) 2D (a) and 3D diffusion simulation of molecular gradients from multiple-point micro-holes of the thin-glass sheet over time (b). (c) Molecular concentration from 3D simulation in the chamber of the device over time. The saturation concentration is indicated after 8 h.

In addition, experimental characterization of netrin-1 gradients released from the multiple points of micro-holes was visualized with Alexa Fluor 488-BSA. The fluorescence intensity shift was observed from the surface of the thin-glass sheet with micro-holes in the chamber **(Figure 22 (a))**. The fluorescence intensity of the molecule increased starting from 1 to 8 h and was followed by a plateau **(Figure 22 (b))**. Different molecular gradients were investigated from the points with less and many micro-holes. The diffusion and gradient generation of the molecule from both conditions started from the point near (0 μm) to far from the micro-holes (225 μm) **(Figure 22 (c))**. The fluorescence intensity shift of the gradient showed different profiles from both representative areas. The faster saturated concentration was shown in the

56

point with many micro-holes than those of less of micro-holes **(Figure 22 (d))**. These results indicated that the developed system could realize precise manipulation by multiple-molecular gradients at a particular time (from 0 to 8 h) to induce individual cell behavior responses (*i.e.*, guided axon outgrowth).
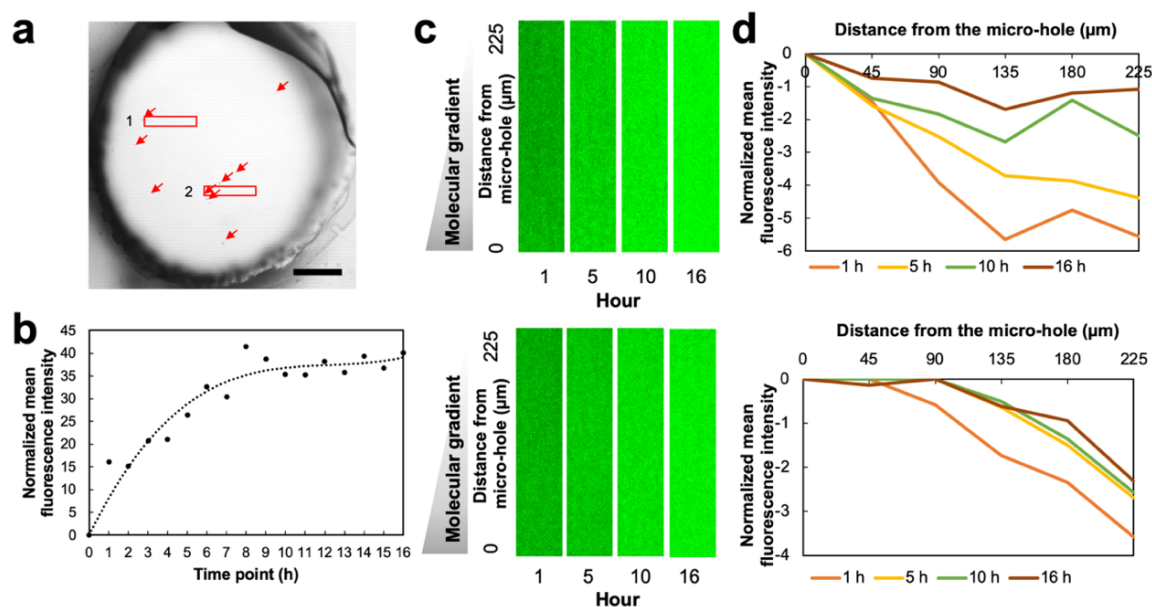

Figure 22. Experimental characterization of multiple points of molecular gradients. (a) The surface of a thin-glass sheet in the chamber that is selected as the focused area of fluorescence intensity changes. The red arrows are the position of micro-holes. The red rectangles are the observed area for molecular gradient changes in the point with less of micro-holes (1) and many of micro-holes (2). (b) Fluorescence intensity shift in the chamber for 16 h from multiple-point laser-fabricated micro-holes. (c) Fluorescence images of a molecular gradient from a red rectangle in (a) from the distance of 0 – 225 μm to the micro-holes over time in the point with less of micro-holes (1; top) and many of micro-holes (2; bottom). (d) Fluorescence intensity shift of a molecular gradient across the field in the point with less of micro-holes (1; top) and many of micro-holes (2; bottom). The scale bar is 200 μm.

4.3 Multiple-point manipulation by femtosecond laser pulses

A multiple-point manipulation by fs laser pulses was carried out to observe hippocampal neuron responses to the multiple-molecular gradients. A multiple-point manipulation was carried out by penetrating the points on the thin-glass sheet during 1 DIV culture. The points on the thin-glass sheet near the neurons with the freely projected axons were selected as the laser-focused spots. The similar laser energy density, *i.e.*, 5.3 J/cm^2, was used to penetrate the thin-glass sheet to fabricate 9 micro-holes **(Figure 23 (a))**. The cells did not affect by the laser

processing, as indicated by the axon outgrowth of neurons located at the nearest distance to the micro-holes **(Figure 23 (b))**.
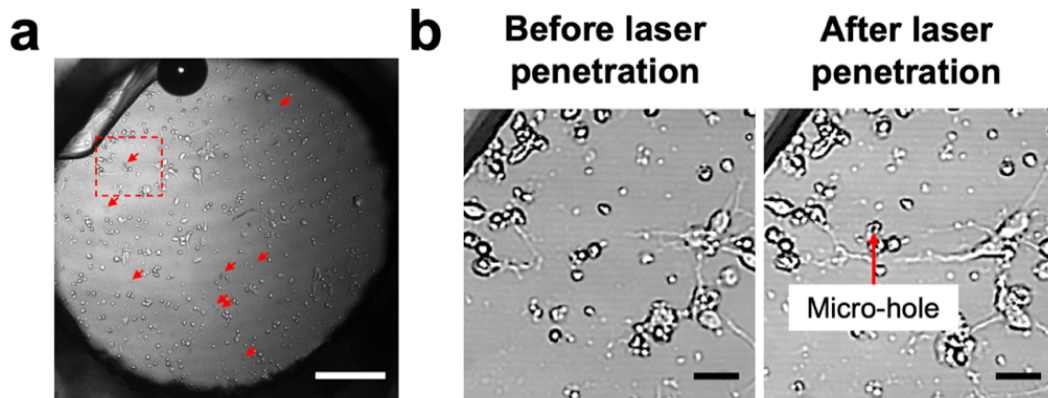

Figure 23. A multiple-point manipulation by fabricating multiple micro-holes on the thin-glass sheet using the femtosecond laser. (a) A photomicrograph of the 1 DIV neuronal culture. Red arrows indicate the laser-fabricated micro-holes. (b) Photomicrographs from a red rectangle in (a) before (left) and after laser processing (right). Scale bars are 200 μm (a) and 50 μm (b).

4.4 Guided axon outgrowth by netrin-1 released from multiple points of micro-holes

After confirming that the netrin-1 gradient generated from single-point laser-fabricated micro-holes can actuate guided axon outgrowth of hippocampal neurons, a precise neuronal actuating system was realized by fabricating micro-holes in multiple points of the thin-glass sheet to generate multiple-molecular gradients. The freely projected axons (n = 12) located near the specific micro-holes were observed **(Figure 24 (a))**. Similar with the single-point micro-hole position, the axons were guided toward each micro-hole in different time points during exposure to netrin-1 (*i.e.*, 2 – 8 h) **(Figure 24 (b, c))**. The trajectories of individual axons with different distances to the micro-holes were depicted during exposure to netrin-1, showing most of the axons projected toward the micro-holes **(Figure 24 (d))**. This result in compliance with the narrower axonal angles during netrin-1 exposure from angles at ≤ 60°, ≤ 90°, and ≤ 120° to ≤ 30° **(Figure 24 (e))**. The mean of axonal angle alternation was 16.6°. Based on this average, 9 out of 12 axons (~75%) had positive angular changes, identified with 7 axons turned higher than the angle average (toward the micro-holes), 2 axons with positive angular changes lower

than the angle average (toward the micro-holes), and 3 axons with negative angular alternation (away from the micro-holes) **(Figure 24 (f))**. These results indicated that the axons responded to multiple netrin-1 gradients generated from multiple points of micro-holes during netrin-1 gradient generation, allowing precise neuronal actuation by fs laser pulses.
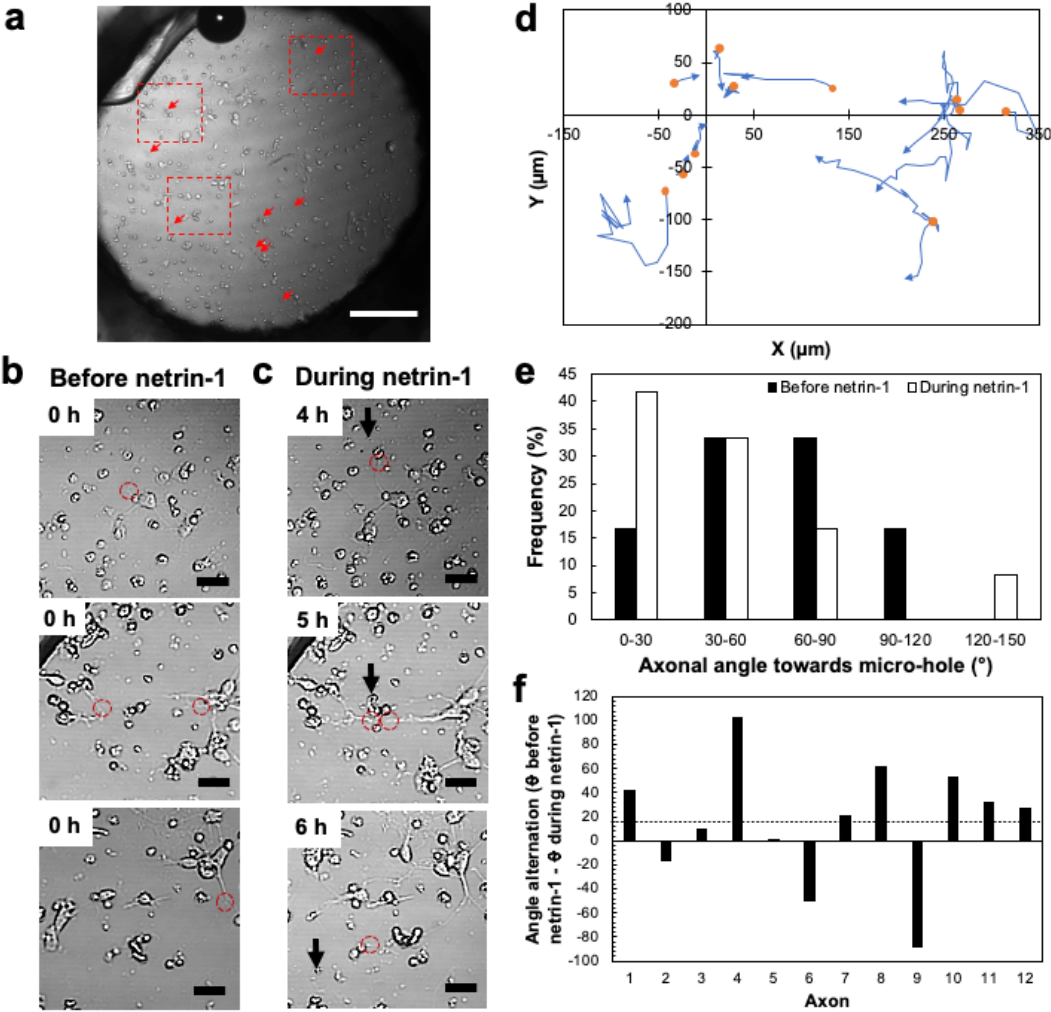
Figure 24. Response of neurons to netrin-1 released from multiple points of micro-holes. (a) Photomicrograph of 9 micro-holes over the thin-glass sheet and the observed freely projected axons. (b, c) Photomicrographs of initial axons from the red rectangles in (a) before netrin-1 exposure (b) and axon outgrowth during netrin-1 exposure (4 – 6 h) (c), showing guided axon outgrowth towards each micro-hole. Black arrows are the micro-holes. (d) Axon trajectories of neurons to netrin-1 gradients generated from multiple points of micro-holes over the thin-glass sheet during 8 h exposure to netrin-1. The micro-holes are normalized at (x = 0 μm and y = 0 μm). The initial axons are normalized with the position of micro-holes. (e) Frequency of axonal angle distribution towards the micro-holes before and during exposure to netrin-1. (f) Axonal angular change before and during exposure to netrin-1. The dashed line represents the mean angle of turning (16.6°) (Upper and lower values from the average turning angle, $p < 0.05$, independent t-test, n = 12). Scale bars are 200 μm (a) and 50 μm (b).

4.5 Distance-dependent neuronal response to netrin-1

Finally, the axon response dependent on the distance toward the molecular source was also investigated. The initial axons with varying distances to the micro-holes were evaluated based on guided timing and guided length. Guided axon timing was the first time point of axons to grow farthest toward the micro-holes. Guided axon length was the elongation of axons toward the molecular gradients at the guided time. The graphics depicted that guided axon timing and guided axon length for the axons located closer to the micro-holes (35 – 135 µm) were shorter than those of the axons located far from the micro-holes (135 – 320 µm) **(Figure 25 (a, b, c, d))**. Interestingly, axons located near the micro-hole also showed a lower axon outgrowth rate than those far from the micro-holes **(Figure 25 (e))**. These analyses demonstrated that guided axon timing, guided axon length, and axon outgrowth rate are dependent on the distance of axons to the micro-holes.
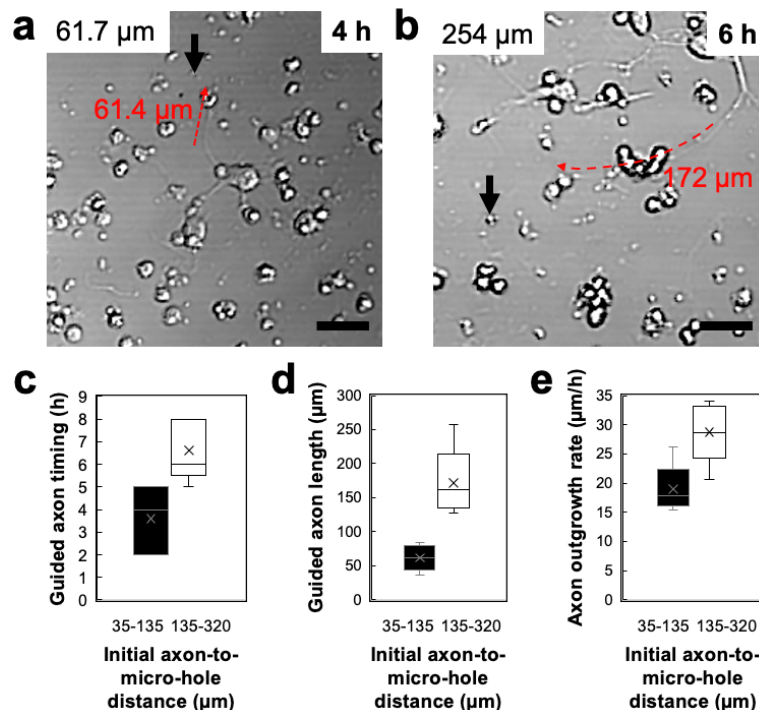
Figure 25. Distance-dependent neuronal response to netrin-1. (a, b) Photomicrographs of axon outgrowth to the micro-holes (red dashed arrow line) for axons located near (61.7 µm) (a) and far from the micro-holes (254 µm) (b). Black arrows are the micro-holes. (c, d, e) Dependency of axon-to-micro-hole distance against guided axon timing (c), guided axon length (d), and axon outgrowth rate (e) located near (35-135 µm) and far from the micro-holes (135-320 µm) ($p < 0.05$, independent t-test, n = 12). Scale bars are 50 µm.

4.6 Comparison of axon guidance and elongation between three experimental groups
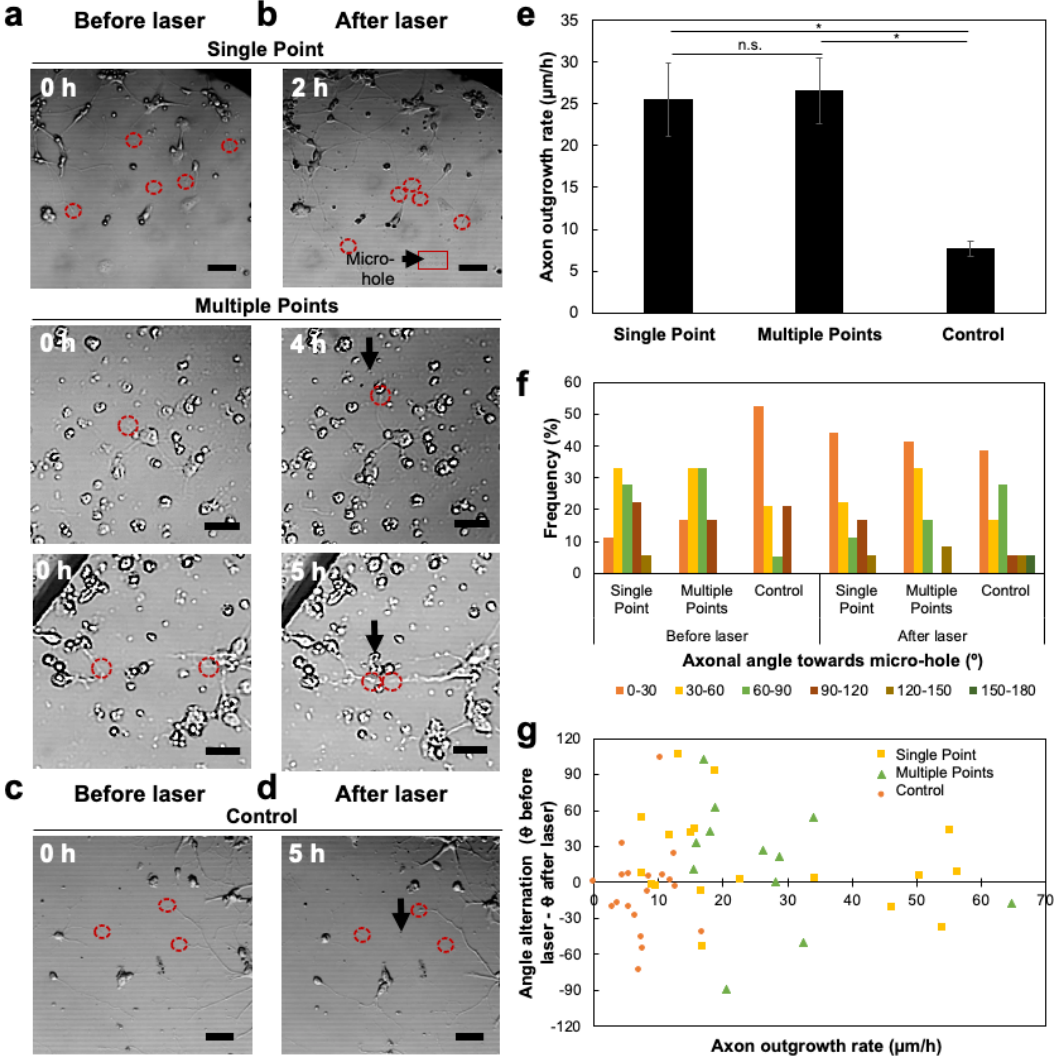
Figure 26. Comparison of axon guidance and elongation from three experimental groups. (a, b) Photomicrographs of initial axons from single-point and multiple-point schemes before laser processing (a) and axon outgrowth after laser processing (b). (c, d) Photomicrographs of initial axons in the control group before laser processing (c) and after laser processing (d). (e) Axon outgrowth rate of neurons from three experimental groups, *i.e.*, single point of micro-holes, multiple points of micro-holes, and control group. Values are shown as means ± SE (n.s., not significant, *, $p < 0.05$, independent *t*-test). (f) Frequency of axonal angle distribution towards the micro-holes before and after laser processing from three experimental groups. (g) Scatter plot of angle alternation before and after laser processing and axon outgrowth rate from three experimental groups (Upper and lower values from the average turning angle of each group, $p < 0.05$, independent *t*-test, n = 12 – 18). Scale bars are 50 μm.

To ensure the behavioral response of cells using this system, the comparison of axon guidance and elongation between three experimental groups were compared. As previously demonstrated, the initial axons were guided toward the micro-holes after netrin-1 exposure from

both experimental groups (single-point and multiple-point manipulation) **(Figure 26 (a, b))**. In contrast, the axons in the control group did not show an extensive acceleration towards the micro-holes after the laser processing **(Figure 26 (c, d))**. In addition, the system could also induce the acceleration of axon elongation during exposure to netrin-1 from both experimental groups (single-point and multiple-point schemes), shown by axon outgrowth rates of 25.5 and 26.6 μm/h, respectively. These values were significantly higher than those in the experimental group with micro-holes without netrin-1 (control group), *i.e.*, 7.7 μm/h **(Figure 26 (e))**.

For the observation of guided axon outgrowth, the percentage of axons at an angle of ≤ 30° was higher than at angles of ≤ 60° − ≤ 180° for single-point and multiple-point schemes during exposure to netrin-1. This result was comparatively different from the control group, showing a lower percentage at an angle of ≤ 30° after the laser processing **(Figure 26 (f))**. In addition, the axonal turning averages for both experimental groups were 18.4° and 16.6°, with 67% and 75% of axons turned with positive angular changes toward the micro-holes. In contrast, the mean of axonal turning was significantly lower (*i.e.*, -7.2°) in the control group, with 44% of axons experiencing a positive turn **(Figure 26 (g))**. These results indicated that most axons were guided toward the micro-holes, shown by narrower axonal angles and positive angular changes in the experimental group with laser-fabricated micro-holes generated netrin-1 gradients.

4.7 Discussion

In chapter 3, the capability of the microfluidic device and fs laser to induce cell behavior responses to the desired manipulation point was realized. In this chapter, spatial control was carried out to induce guided axon outgrowth to observe neuronal behavior responses to varied locations. In previous studies, spatiotemporal control to regulate axon outgrowth can be achieved by various technologies based on geometric and physical guidance cues.[26,191–193,222–225] In this study, a chemical cue was released by the fs laser pulse by penetrating the thin-glass

sheet to create the micro-holes depending on the location of nearby freely projected initial axons. The use of 4 μm thick thin-glass sheet embedded in the microfluidic device enabled the penetration of fs laser in short time within seconds. Thus, the operation of multiple-point manipulation by fs laser was precise yet simple compared to the other technologies due to the not time-consuming processing and not complicated steps.

Based on the role of netrin-1 that can accelerate axon elongation of neurons, the outgrowth rate of the observed axons toward the nearest micro-holes (multiple-point manipulation) (*i.e.*, 26.6 μm/h) was comparable with single-point manipulation (*i.e.*, 25.5 μm/h) and other experiments with netrin-1 **(Figure 26 (e))**. Moreover, based on the capability of the device to generate multiple gradients of netrin-1 **(Figure 21 (a), 22 (c)),** the neuronal behavior response of guided axon outgrowth during the netrin-1 exposure was investigated. Most axons experienced guided axon outgrowth, as indicated by narrower axonal angles **(Figure 24 (e), 26 (f))** and positive axonal angular changes to each micro-hole generated-molecular gradient **(Figure 24 (f), 26 (g))**.

Furthermore, the ability of the device to exhibit different timing of saturation concentration of netrin-1 **(Figure 22 (d))** affected the different axons' responses located near and far from the micro-holes. The initial axons near the micro-holes received the netrin-1 gradients earlier with higher concentrations than those far from the micro-holes, affecting guided axon outgrowth with a shorter guided timing **(Figure 25 (c))**. In addition, the axons also had a shorter guided length with an average outgrowth rate lower than the axons far from the micro-holes **(Figure 25 (d, e))**. These shorter responses are caused by the saturation effect, where receptors in the axonal growth cones respond to high concentrations of netrin-1.[226,227]

Apart from the most percentage of axons underwent narrower angular changes, some axons experienced grow away from the molecular gradients. This might be caused by the different stages of neurodevelopment history of neurons when a netrin-1 gradient is applied. In addition,

the responsiveness of neurons to netrin-1 may have altered after dissociation.[198] The response of the axon guidance to netrin-1 is determined by transmembrane receptors expressed on the part of the axon, called the growth cone, which continually explores the environment to sense the presence of chemical cues. Apart from its function as a chemo-attractant cue, netrin -1 also has a function as a repellent cue in axon guidance. The attractive and repulsive responses of axons are triggered by activated netrin-1 receptors within the same growth cone, *i.e.*, Deleted in Colorectal Cancer (DCC) and UNC5.[228] In the previous study, co-expression of DCC on growth cones of neurons leads axon attraction.[229] In addition, the DCC expression is also present in the dependent effect of UNC5 for axon repulsion.[229,230] Thus, DCC has a critical role in both responses during neuronal growth and development.[198,231]

4.8 Conclusions

In utilizing the advantage of fs laser in spatial resolution, precise guided axon outgrowth of neurons could be achieved in a microfluidic device. The multiple-point manipulation was obtained by fs laser penetration on target points of the thin-glass sheet. Each fabricated micro-hole was employed as a mediator to transport a guidance molecule to influence individual cell behavior response (*i.e.*, guided axon outgrowth). The 4 µm thick thin-glass sheet was also advantageous to allow the fabrication of micro-sized micro-holes, allowing the transportation of the molecule in a low stream and the generation of molecular gradients to induce precise guided axon outgrowth. The developed system can be used to investigate other individual cell behavior responses. In the future, the development of an integrative microfluidic device, *e.g.*, the installation of liquid controllers and multiple molecular compartments, is required to observe longer cell behavior and monitor multiple cell behaviors simultaneously. Further, neuronal regeneration can also be achieved by implanting a microfluidic device penetrated with a femtosecond laser into brain lesions to attain functional tissue recovery following brain injury.

Chapter 5

Reverse Cell Sorting by Femtosecond Laser Scanning

5.1 Introduction

In neuroscience, the downstream analysis after single-cell manipulation is indispensable to gather more information about the genes, transcriptomes, proteins, and metabolomics at a single-cell level. For example, derived cells from neural stem cells (NSC), such as neurons and microglia, are dynamic cells that change their morphology and expression profile in response to their local environment, including chemical guidance cues.[232,233] The isolation and sorting attempts that target individual cells expressing specific morphology and substances are required to profile health conditions and neurological diseases.

Several methods have been employed to sort NSC-derived cells *in vitro* and *in vivo*, including fluorescence-activated cell sorting (FACS), laser-capture microdissection (LCM), and ribosome messenger RNA (mRNA)-trap technology. The FACS technology uses fluorescent probes that are labeled to the cell, so the cells can only be used once during processing.[234] Thus, the sequential observation after the sorting cannot be achieved. In addition, mRNA-trap technology has been used to distinguish different cell populations in brain.[235,236] However, this approach needs the use of transgenic mice, expensive reagents, and performs with complicated steps. Furthermore, LCM technology takes advantage of infrared laser that can penetrate the cells, allowing the capture of a single neuron with high specificity and spatial resolution.[237,238] However, this technology introduces stresses during cell isolation, which may display an alternation of cellular and subcellular information. Thus, the cell sorting attempt with the prerequisites of high spatiotemporal resolution to prevent undesirable stimulation, minimize cell interferences, and provide sequential cell observation for further single-cell manipulation and analysis, is needed.[124] Based on the advantages previously described, a femtosecond (fs) laser can be applied to fulfill these requirements in single-cell sorting.

In this chapter, reverse cell sorting of immortalized megakaryocyte progenitor cell lines (imMKCLs) was conducted by detaching non-target cells using fs laser scanning to isolate individual target cells. The imMKCLs are derived from human induced-pluripotent stem cells (hiPSCs) or human embryonic stem cells (hESCs) overexpressed with c-MYC, BMI1, and BCL-XL genes to induce cell proliferation. The imMKCLs are reported to be promising alternative cells to produce platelets, replacing fresh platelets obtained from blood donors.[202] Platelet transfusions are recognized to play a role in the treatment of blood diseases and traumas.[239–243] The use of imMKCLs has several advantages over fresh platelets in providing effective transfusions. The cells have a long shelf life under frozen conditions and an extended culture period. Also, the cells provide human leucocyte antigen (HLA) and human platelet alloantigen (HPA) matching between donor and recipient that minimizes cell rejection.[202]

The ability of imMKCLs to proliferate is essential for maintaining the production of platelets. During cell expansion, megakaryocytes are sensitive to various handling procedures, such as freezing, thawing, and washing.[244–247] In addition, the cells are known to weakly adhere to the culture substrate, leading to their detachment following medium aspiration.[248,249] The exposure of the cells to these conditions could induce degranulation and internal shape alterations.

It has been reported that different clones of imMKCLs with gene modification or growth factor addition may display different cell fates, *i.e.*, remaining as megakaryocytes or differentiating to platelets.[202] These cells are usually characterized and purified in bulk numbers with a flow cytometer.[202,250] Flow cytometry technology uses fluorescent probes to purify floating cells in suspension, so the cells can only be used once during processing. Thus, continuous cell observation following the purification cannot be achieved, limiting the biochemical and physiological studies to a single-cell level. Based on the sensitive characteristics of the cells and the limitation of further cell analysis by the previously available

technology, a system that allows *in situ* cell sorting to prevent undesirable stimulation and allows sequential cell observation after the sorting process is therefore required for further single-cell manipulation and analysis at a single-cell level.

Several technologies have been employed for *in situ* cell sorting that allow sequential cell observation after the sorting process, such as temperature-responsive polymer,[251,252] laser-induced light-responsive polymer,[253] ultraviolet (UV) laser,[254,255] visible laser,[256,257] and infrared (IR) laser (*e.g.*, femtosecond laser).[90,148,149] However, the utilization of temperature-responsive and laser-induced light-responsive polymers are limited for eliminating adherent cells. It is also necessary to coat specific polymers on the cell culture dish and maintain specific chemical and thermal conditions to control the polymers and cells that may induce cell interferences and cellular changes. Recently, laser technologies (*e.g.*, UV, visible, and fs lasers) allow the sorting process for floating and adherent cells with simple cell preparation and culture conditions. In addition, laser technologies offer spatiotemporal resolution, enabling precise cell elimination, *in situ* cell sorting, and multiple uses of isolated cells for further single-cell manipulation and analysis.

The fs laser has advantages over other pulsed lasers. The IR ultrashort pulse penetrates most cells and cell scaffolds as well as glass materials and cell culture dishes,[63,64,91–99] inducing an effective absorption at the laser focal point. As a benefit of the three-dimensional absorption and the photomechanical ablation,[93] the fs laser pulse allows selective cell elimination with a small pulse energy. On the other hand, when other pulsed lasers (*e.g.*, nanosecond lasers with wavelengths from UV to IR regions) are utilized, a relatively large pulse energy is required for cell elimination due to ineffective multi-photon absorption as well as photothermal and photochemical ablations. The small energy exposure by the fs laser is presumed to minimize the photothermal or photochemical denaturation of the object outside the focal point.

Hosokawa group has reported the application of a fs laser-induced impulsive force to isolate

numerous individual cells, *e.g.*, NIH/3T3,[90,148,149] PC12,[150] and hippocampal neurons.[147] The manipulation is carried out by focusing the pulse on the area inside the culture medium around the cells to induce stresswaves, which are beneficial for detaching and isolating the cells.[90,147–150] However, this research has been limited by the slow isolating process and low viability of the sorted cells. In another study, fs laser ablation was also used to kill and detach the cells from the culture substrate.[156] A single laser pulse ablated the non-target cells to induce their natural detachment from the culture substrate, leaving the individual target cells. However, this attempt required long-time processing (1 – 5 h) for cell detachment, and the sequential observation of the target cells was therefore limited.
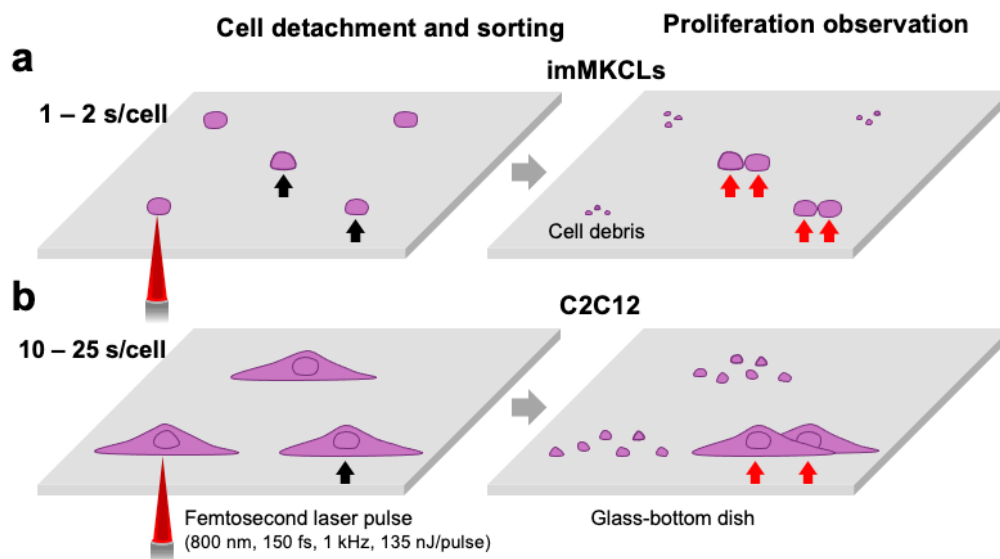
Figure 27. Schematic illustration of femtosecond (fs) laser scanning for immortalized megakaryocyte progenitor cell lines (imMKCLs) and the myoblast cell line (C2C12) and proliferation observations. (a) The imMKCLs were killed by fs laser scanning on the culture substrate within 1 – 2 s/cell. (b) The C2C12 cells were scanned by the fs laser pulse to kill and detach the cells from the culture substrate within 10 – 25 s/cell. The target cells (black arrows) were sorted and cultured. Afterward, the target cells underwent proliferation into two cells (red arrows) at a particular time point.

Based on the challenges of previous technologies and studies, a reverse cell sorting system with the perquisites of simple operation, applicability to different cell types, having high spatiotemporal resolution to prevent undesirable stimulation, minimizing cell interferences, and

providing sequential cell observation for further single-cell manipulation and analysis, is needed.[124] In this study, the reverse sorting of imMKCLs by femtosecond laser scanning was demonstrated. In addition, the myoblast cell line (C2C12) was also used to represent the adherent cells that attach to the culture substrate. The reverse sorting was carried out by killing and detaching non-target cells from the culture substrate and sorting the target cells. The target cells were then cultured and continuously observed to verify their ability to proliferate **(Figure 27)**.[258]

5.2 Reverse cell sorting by femtosecond laser scanning

Initially, cell death following irradiation with various energies of laser pulses was investigated. Cell death analysis based on PI staining showed that increasing the laser pulse energy resulted in higher numbers of cell deaths **(Figure 28)**. The pulse energy of 70 nJ/pulse did not induce cell death. Meanwhile, laser pulse energies higher than 70 nJ/pulse could induce cell death, with pulse energy of 135 nJ/pulse and 160 nJ/pulse inducing death of all cells. Based on this result, the 135 nJ/pulse laser energy was utilized to kill and detach imMKCLs and C2C12 cells since it can kill all cells while generating minimum water bubbles.
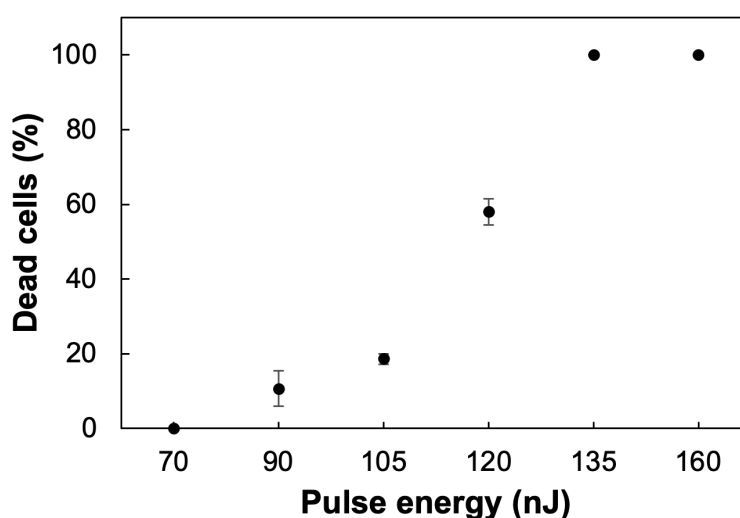
Figure 28. Percentage of dead cells at different laser pulse energies. The marks show the average percentage of dead cells, and the bars indicate the standard error (SE; n = 3).

5.3 Cell behavior observation after laser scanning

Firstly, C2C12 cells were processed by fs laser scanning due to their adherent behavior on the culture substrate, which allows easier manipulation and observation. After 1 DIV of culture, the cells were randomly selected as the target and non-target cells **(Figure 29 (a))**. The laser scanning was then performed to detach and eliminate the non-target cells from the culture substrate. The pulse energy of 135 nJ/pulse was able to kill and detach the cells within $10 - 25$ s/cell. The laser scanning could detach non-target cells from the culture substrate, while the sorted viable target cells remained attached to the substrate. Confocal fluorescence microscopy observation also confirmed the PI localization in the dead detached cells, while the viable target cells remained unstained **(Figure 29 (b))**.
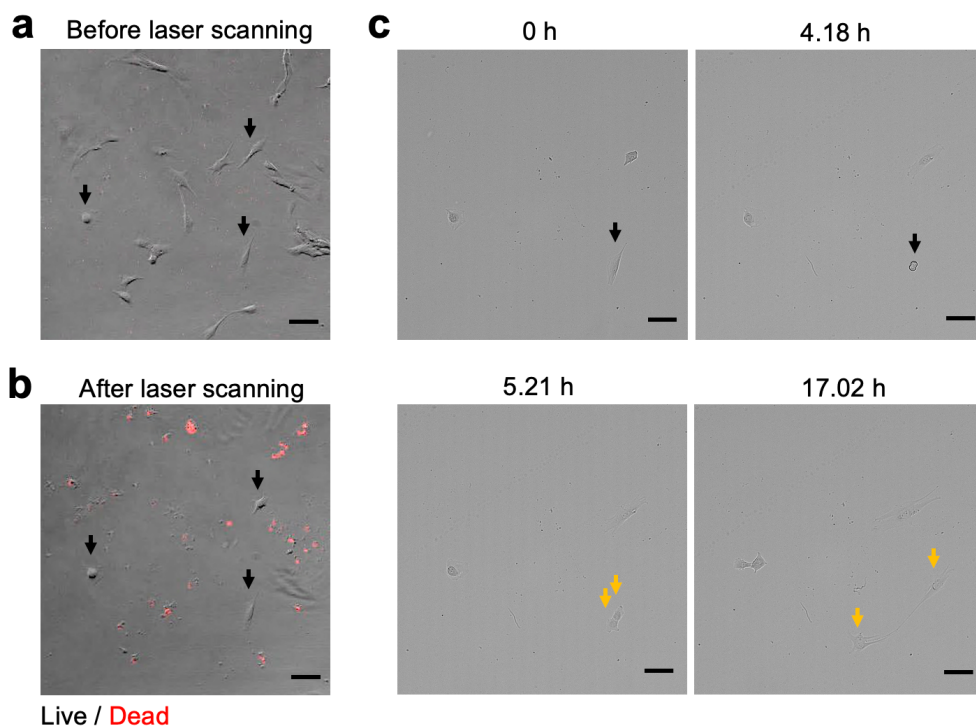
Figure 29. Observation of C2C12 behavior after femtosecond laser scanning. (a) Culture conditions before laser scanning, showing the target cells (black arrows) and non-target cells attached on the culture substrate. (b) Confirmation of cell death of non-target cells using PI staining after laser scanning. (c) Time-lapse observation of the target cell (black arrow) showing cell division into two daughter cells (yellow arrows) and migration. Scale bars are 100 μm.

After the laser scanning of C2C12 cells, the culture medium containing the non-target cells

was replaced with fresh medium. The washing process could also extend the space for cell growth. The attached target cells remained on the culture substrate after the washing. Time-lapse observation showed that the target cells could proliferate at a particular time point. In the proliferation stage, the morphology of the cells changed into a spherical shape, divided into two daughter cells, re-attached and then migrated **(Figure 29 (c))**.
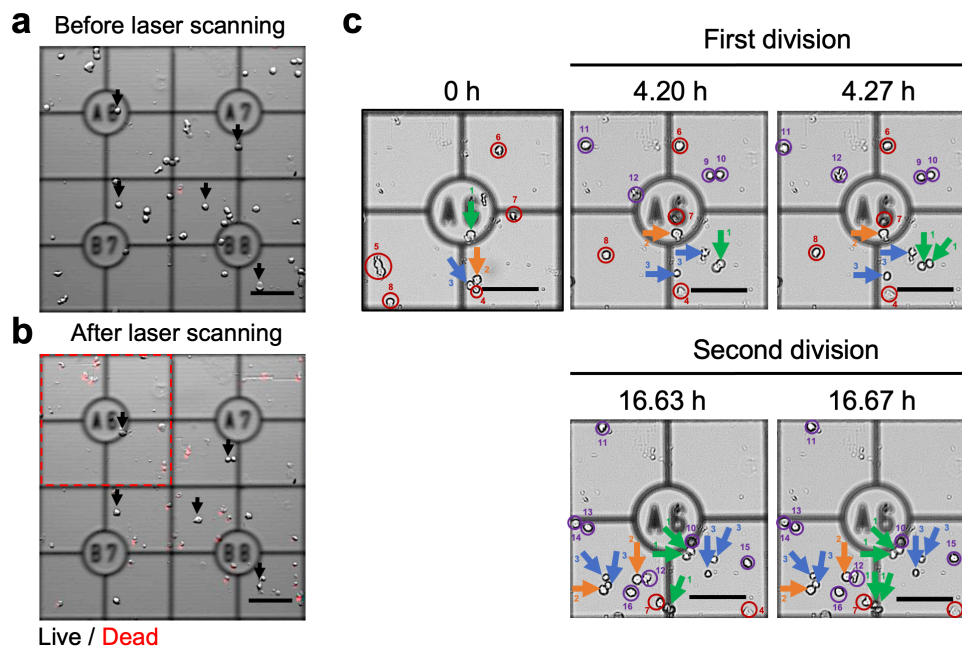

Figure 30. Observation of imMKCL behavior after femtosecond laser scanning. (a) Cell culture before laser scanning. (b) Confirmation of cell death of the non-target cells by PI staining after laser scanning. Black arrows indicate viable target cells. (c) Representative time-lapse observation of the target cells in the A6 grid (red dashed square in (b)). The difference in target cell positions in (b) and (c) might be due to the addition of fresh medium after laser scanning, which moved the imMKCLs that were weakly attached to the Matrigel-coated glass-bottom dish. The target cells (blue, green, and orange arrows) could undergo division, producing daughter cells. Further observation showed that the daughter cells could undergo second division. Several non-target cells (red circles) were observed to float out of the observation area. In addition, non-target cells from adjacent areas were observed to float into the observation area (purple circles). No cell divisions were observed in the non-target cells. Scale bars are 100 μm.

In the imMKCL culture, irradiation with the 135 nJ/pulse could also kill the non-target cells within 1 – 2 s/cell, as demonstrated from the PI staining **(Figure 30 (a, b))**. The time-lapse observation was conducted to investigate the behavior of target cells **(Figure 30 (c))**. As a demonstration, the target cells in the A6 grid were observed. A slight difference was observed in the position of cells at 0 h of the time-lapse compared with the PI-stained cells in Figure 28

(b). In this study, the imMKCLs were weakly attached to the Matrigel-coated glass-bottom dish. Therefore, the addition of fresh medium before the time-lapse observation might move the cells from a location adjacent to the observation area.

The time-lapse observation showed that the target imMKCLs could migrate and divide into two cells after laser scanning. These divided cells (n = 14) were then able to divide into sequential individual cells (second proliferation) **(Figure 30 (c))**. No statistically significant difference (*p* > 0.05) was observed in the first division time of imMKCLs in the normal culture without laser scanning and target cells after laser scanning **(Figure 31 (a))**. The target cells also showed a relatively similar time between the first and second divisions as the cells cultured without laser scanning **(Figure 31 (b))**.
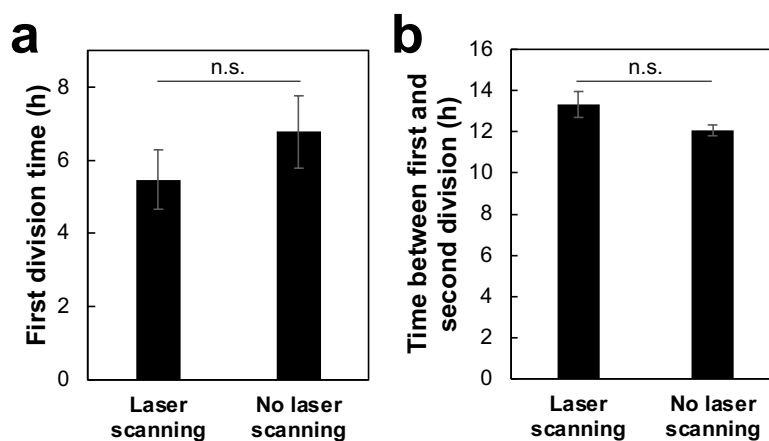
Figure 31. Division time of imMKCLs for conditions with and without laser scanning. (a) First division time of the cells after laser scanning and without laser scanning. (b) The time needed for the cells to divide between first and second cell divisions (doubling time). Values are average ± SE (n = 14). n.s., not significant, *p* > 0.05, Independent *t*-test.

5.4 Discussion

In previous studies, femtosecond laser-induced impulsive force with different laser pulse energy has been applied to kill and detach the cells from the culture substrate.[90,145–150] These studies relied on the generated shockwave following an intense fs laser pulse to manipulate the cells. However, these contactless approaches are limited by the slow process and low success rate of cell detachment. In another study, a single pulse fs laser ablation with a pulse energy of

150 nJ/pulse was used to kill the cells with a 100% success rate.[156] In this present study, the laser energy of 135 nJ/pulse was utilized to scan non-target cells for cell killing and detachment **(Figure 28)**. Both C2C12 **(Figure 29 (b))** and imMKCLs **(Figure 30 (b))** could be rapidly detached (1 – 25 s/cell), and 100% of the cells were successfully sorted.

In studies of cell detachment, laser irradiation was reported to have a damaging effect on the cells adjacent to the irradiated cells.[90,148] To minimize this effect, the cells were seeded with a particular density on the culture substrate. Therefore, the target cells that were not irradiated with the fs laser pulse were not subjected to the damaging effect. Indeed, the results indicated that the target cells showed normal cell behaviors, such as cell proliferation and migration **(Figure 29 (c), 30 (c))**. All target C2C12 cells underwent proliferation after the laser processing. The normal physiological transition of adherent cells was observed in this study, *i.e.*, initial attachment, spherical shape formation during cell division, and re-attachment to the culture substrate **(Figure 29 (c))**.[259–261] In the case of imMKCLs, each sorted cell proliferated into two cells, and each divided cell underwent a second proliferation **(Figure 30 (c))**. More importantly, the cell doubling time of the sorted cells was similar to the doubling time of the normal cells **(Figure 31)**. These simultaneous results indicated that the laser scanning did not interfere with the proliferation of imMKCLs.

5.5 Conclusions

In conclusion, this study demonstrated the reverse sorting of imMKCLs by detaching non-target cells using femtosecond laser scanning and sorting the target cells. Laser scanning allowed a short processing time with a high success rate of cell detachment and sorting. More importantly, femtosecond laser scanning had a negligible effect on the behavior of the sorted cells (*i.e.*, proliferation). This system can be applied to observe other cellular behaviors of specific cells at a single-cell level and realize further manipulations and analyses of single cells.

Chapter 6
General Conclusions

6.1 Conclusions

The research objective to develop the system of real-time and precise guided axon outgrowth on the scaffold could be achieved. This study incorporated a femtosecond (fs) laser and a microfluidic device. The fs laser played a role to attain spatial control of guided axon outgrowth on the 4 μm thick thin-glass sheet embedded in a microfluidic device. A microfluidic device provided a reservoir to store a guidance molecule and the embedded of the thin-glass sheet that was penetrated by fs laser to create the micro-holes. The fabricated micro-holes were responsible as transporters to deliver a guidance molecule to the neurons, inducing the elongation and guidance of axon outgrowth. These neuronal responses could be observed toward single-point and multiple-point molecular sources.

Cell sorting attempt after single-cell manipulation is indispensable to gather more information about genes, transcriptomes, proteins, and metabolomics at a single-cell level. In handling sensitive cells (*e.g.*, megakaryocytes), a reverse cell sorting system with the perquisites of simple operation, applicability to different cell types, having high spatiotemporal resolution to prevent undesirable stimulation, minimizing cell interferences, and providing sequential cell observation for further single-cell manipulation and analysis, is needed.[124]

In the subsequent study, reverse sorting of immortalized megakaryocyte progenitor cell lines (imMKCLs) by fs laser scanning was conducted. The myoblast cell line (C2C12) was also used to represent the adherent cells that attach to the culture substrate. The reverse sorting was carried out by killing and detaching non-target cells from the culture substrate and sorting the target cells. The target cells underwent proliferation following the laser scanning. This cell behavior showed the reliability of the system to isolate individual cells. Finally, possible

applications of the system utilizing spatial resolution of fs laser were described. Those findings were summarized chapter by chapter below.

Chapter 1 described several topics of single-cell analysis using microfluidic devices and femtosecond laser. The importance of single-cell analysis is discussed to overcome the limitation of the bulk analysis. Moreover, single-cell analysis is critical to observe several behaviors, such as morphology, proliferation, differentiation, and migration. Several methods, such as conventional culture vessels, microgels, and micropatterned substrates, are used to conduct single-cell cultivation. However, each method has limitations in observing certain phenomena during single-cell cultivation and analysis. Thus, a promising method, a microfluidic device, is employed to perform single-cell analysis, such as microdroplets, microchamber arrays, fluidic force traps, and passive wells. During single-cell analysis, a femtosecond laser can be incorporated into a microfluidic device to manipulate the behavior of cells. Therefore, femtosecond laser processing for single-cell analysis is described. The main cell behavior in this thesis, *i.e.*, guided axon outgrowth, is discussed with various technologies. Finally, the research objective and research outline were also described.

Chapter 2 described the methods for guided axon outgrowth by molecular gradients generated from laser-fabricated micro-holes and reverse cell sorting by femtosecond laser scanning. The microfluidic device was fabricated to provide the introduction of chemical guidance (*i.e.*, netrin-1) and the embedded of a culture substrate (*i.e.*, a 4 μm thin-glass sheet) penetrated by femtosecond laser pulses. The generation of molecular gradient through the micro-holes in the microfluidic device was described by simulation and experimental characterization. Before the manipulation, the hippocampal neurons were cultured on the microfluidic device for 1 day *in vitro* (DIV). An amplified femtosecond laser pulse was focused and irradiated the thin-glass sheet through a 10× objective lens (NA. 0.25) to fabricate the micro-holes to release the netrin-1. The repetition rate and pulse energy density of the fs laser

were 1 kHz and 5.3 J/cm^2, respectively. Afterward, time-lapse imaging was performed to investigate continuous guided axon outgrowth towards the fabricated micro-holes. After the manipulation of guided axon outgrowth, the methods for reverse cell sorting by femtosecond laser scanning were also described. Immortalized megakaryocyte progenitor cell lines (imMKCLs) and the myoblast cell line (C2C12) were cultured on a glass-bottom dish for 1 DIV and followed with a cell death assay. Reverse cell sorting by fs laser pulses (energy: 135 nJ/pulse and repetition rate: I kHz) was carried out by detaching the non-target cells, and time-lapse imaging was performed to verify the ability of the target cells to proliferate.

Chapter 3 discussed guided axon outgrowth by molecular gradient generated from single-point laser-fabricated micro-holes. The manipulation was carried out by the irradiating the thin-glass sheet to fabricate the micro-holes in single point in the center of the thin-glass sheet. The netrin-1 gradient was generated on the microfluidic device, affecting axon elongation and axon outgrowth. Accelerated axon elongation and axon guidance towards the micro-holes were observed. The guidance effect of netrin-1 was in accordance with the released and generation of netrin-1 gradient from 0 to 8 h.

Chapter 4 demonstrated guided axon outgrowth by molecular gradient generated from multiple-point laser-fabricated micro-holes. The manipulation was performed by fabricating the micro-holes in the multiple points of the thin-glass sheet. This experiment enabled spatial control to induce guided axon outgrowth towards varied locations. Longer axon outgrowth and guided axon outgrowth towards each micro-hole were shown. Finally, axons' responses, such as guided time, guided length, and axon outgrowth rate, were also dependent on the distance to the micro-holes.

Chapter 5 described the reverse sorting of single cells by femtosecond laser scanning. The sorted target cells were observed to verify their ability to proliferate. The proliferation time of target cells after the laser scanning was comparable with the culture without laser scanning.

These results indicated that laser scanning did not interfere with the proliferation of imMKCLs. This system is essential to process individual cells for further single-cell manipulation and analysis.

Chapter 6 described the conclusions of the achieved precise and real-time system integrating femtosecond laser and microfluidic device to induce guided axon outgrowth on the scaffold. Moreover, the subsequent study also attained reverse cell sorting by fs laser scanning with a short-processing time and high success rate. Finally, the chapter also contained a summary of each chapter and future perspectives utilizing the developed system.

6.2 Perspectives

The developed systems, *i.e.*, a microfluidic device with femtosecond laser penetration and reverse sorting by femtosecond laser scanning, can be applied for the following studies in the future.

6.2.1 Single-cell analysis

This study achieved a precise, non-invasive, and real-time actuation system of a microfluidic device integrated with a femtosecond (fs) laser to fabricate the micro-holes that enable the delivery of a guidance molecule to manipulate the cells. The combination of both approaches was beneficial in providing cell culture and cell manipulation at a single-cell level. This system can be applied to manipulate and investigate other cell types for different experimental purposes, *e.g.*, neural regeneration, immune cell response, stem cell differentiation, cancer cell proliferation, wound healing process, and other biological phenomena. After the manipulation, the fs laser is also possible to perform subsequent cell processes in a microfluidic device, such as cell sorting, manipulation, and dispensing.

The subsequent study also attained a reverse cell sorting using fs laser scanning with a short-processing time and high success rate. This system was applied to isolate the cells with high spatiotemporal resolution to prevent undesirable stimulation and minimize cell interferences. The isolated cells were observed to verify their ability to proliferate. Further, single-cell manipulation and analysis can also be conducted to obtain omics profiles of individual cells **(Figure 32)**.
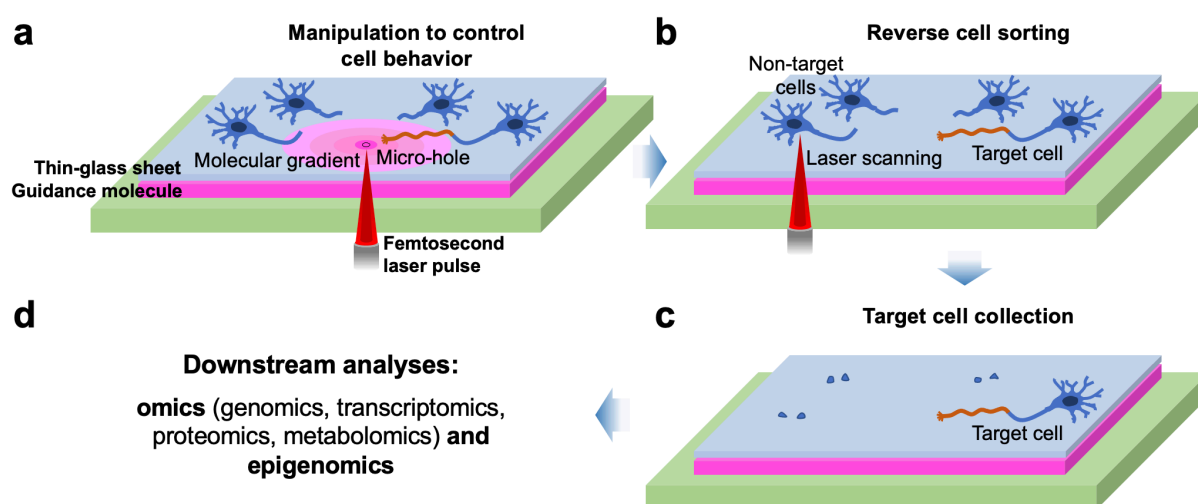
Figure 32. Schematic illustration of single-cell analysis from upstream to downstream analyses utilizing femtosecond laser processing. (a) Cell behavior is induced by a molecular gradient generated from a laser-fabricated micro-hole. (b) After the manipulation, the target cell is sorted by detaching the non-target cells using laser scanning. (c and d) The target cell is then collected for further downstream analyses.

In the future, the development of the integrative and comprehensive microfluidic device is required to improve the reliability of the system to evaluate single cells. The installation of multiple molecular compartments is needed to monitor multiple single-cell behavior responses simultaneously. The incorporation of several controllers (*e.g.*, pumps and valves) is also needed to provide the automatic regulation of cell loading, medium perfusion, and cell dispensing. In addition, the liquid controller allows the generation of a constant molecular gradient to observe longer single-cell behavior responses. The reverse cell sorting by the fs laser scanning can be continued with subsequential cell manipulation and evaluation by installing real-time

measurement techniques, such as electrophysiological recording. Furthermore, the provision of cell retrieval system (*e.g.*, cell picking or dispensing) is critical for the downstream analysis of individual cells. Therefore, the development of an advanced microfluidic device is indispensable to allow simultaneous single-cell analysis from upstream to downstream in one chip.

6.2.2 Implantable device for neuronal regeneration

As previously described, transplantation of neuronal cells and directed axonal outgrowth on the scaffold have been carried out for the treatment of central brain injury,[26,167–170,175,176] which is identified by massive cell loss and failure of the organization of neuronal connections. However, precise axonal integration to obtain functional recovery remains one of the greatest challenges. Therefore, the developed system from this study which allows the precise, non-invasive, and real-time actuation can be implemented as an implantable device for neuronal regeneration.

The femtosecond laser has been recognized as a tool for various clinical trials.[152,153] Penetration of fs laser is also possible conducted to induce neuronal regeneration after brain injury. Cortical tissue lesion of mouse brain can be treated by transplantation of a microfluidic device containing a channel for placing molecules and a thin-glass sheet penetrated by a femtosecond laser. The femtosecond laser pulses irradiate the thin-glass sheet to fabricate micro-holes. The molecule is released from the laser-fabricated micro-holes and induces axon guidance of host neurons. Axon outgrowths are expected can develop organized connections with other host neurons, inducing functional recovery after brain injury **(Figure 33)**. Based on the real-time actuation by fs laser, the developed system can be applied to treat brain injury depending on the size of cell loss and the condition of brain injury.

To realize the developed system as an implantable device, further improvements are required. The thin-glass sheet provides thin, biocompatible, and transparent characteristics, which are advantageous to be developed as a scaffold. However, further assessments of the inflammation and glial reaction after the transplantation of the thin-glass sheet are needed. Apart from the thin character of the scaffold, the thin dimension of a complete device is also necessary to increase the success of neuronal regeneration and functional recovery.
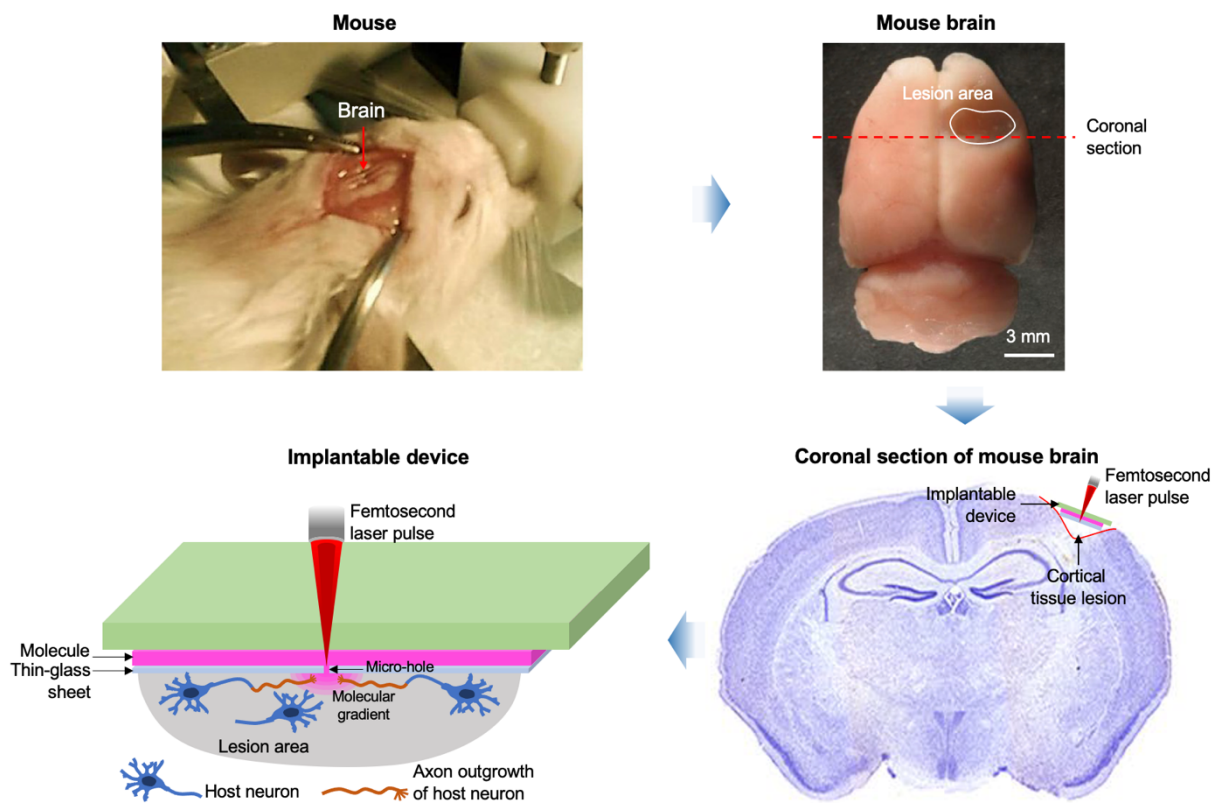
Figure 33. Schematic illustration of the implantable device for treating brain injury lesion. The mouse brain with cortical tissue lesion is transplanted with a microfluidic device containing a channel for placing molecules and a thin-glass sheet penetrated by a femtosecond laser. The femtosecond laser pulses irradiate the thin-glass sheet to fabricate micro-holes. The molecule is released from the laser-fabricated micro-holes and induces guided axon outgrowth of host neurons. Axon outgrowths are expected to develop established connections with other host neurons, inducing functional recovery after brain injury.

References

1   Y. Hao, S. Cheng, Y. Tanaka, Y. Hosokawa, Y. Yalikun and M. Li, *Biotechnol Adv*, 2020, **45**, 107648.

2   B. Gu, J. Zhang, W. Wang, L. Mo, Y. Zhou, L. Chen, Y. Liu and M. Zhang, *PLoS One*, 2010, **5**, e15795.

3   W. C. Aird, *Cold Spring Harb Perspect Med*, 2012, **2**, a006429.

4   D. G. Tang, *Cell Res*, 2012, **22**, 457–472.

5   S. Haas, A. Trumpp and M. D. Milsom, *Cell Stem Cell*, 2018, **22**, 627–638.

6   E. Papalexi and R. Satija, *Nat Rev Immunol*, 2018, **18**, 35–45.

7   B. Yang, J. B. Treweek, R. P. Kulkarni, B. E. Deverman, C.-K. Chen, E. Lubeck, S. Shah, L. Cai and V. Gradinaru, *Cell*, 2014, **158**, 945–958.

8   T. Bakken, L. Cowell, B. D. Aevermann, M. Novotny, R. Hodge, J. A. Miller, A. Lee, I. Chang, J. McCorrison, B. Pulendran, Y. Qian, N. J. Schork, R. S. Lasken, E. S. Lein and R. H. Scheuermann, *BMC Bioinformatics*, 2017, **18**, 559.

9   A. K. Poulsen, M. Ø. Petersen and L. F. Olsen, *Biophys Chem*, 2007, **125**, 275–280.

10   M. P. Kumar, J. Du, G. Lagoudas, Y. Jiao, A. Sawyer, D. C. Drummond, D. A. Lauffenburger and A. Raue, *Cell Rep*, 2018, **25**, 1458–1468.

11   L. A. Harris, S. Beik, P. M. M. Ozawa, L. Jimenez and A. M. Weaver, *Curr Opin Syst Biol*, 2019, **17**, 24–34.

12   D. Wang and S. Bodovitz, *Trends Biotechnol*, 2010, **28**, 281–290.

13   W. Chen, S. Li, A. S. Kulkarni, L. Huang, J. Cao, K. Qian and J. Wan, *Biotechnol J*, 2020, **15**, 1900262.

14   H. Nakaoka and Y. Wakamoto, *PLoS Biol*, 2017, **15**, e2001109.

15   B. Dura, M. M. Servos, R. M. Barry, H. L. Ploegh, S. K. Dougan and J. Voldman, *Proceedings of the National Academy of Sciences*, 2016, **113**, E3599–E3608.

16   N. Ota, Y. Yonamine, T. Asai, Y. Yalikun, T. Ito, Y. Ozeki, Y. Hoshino and Y. Tanaka, *Anal Chem*, 2019, **91**, 9631–9639.

17   Y. Brody, R. J. Kimmerling, Y. E. Maruvka, D. Benjamin, J. J. Elacqua, N. J. Haradhvala, J. Kim, K. W. Mouw, K. Frangaj, A. Koren, G. Getz, S. R. Manalis and P. C. Blainey, *Genome Res*, 2018, **28**, 1901–1918.

18   R. J. Kimmerling, G. Lee Szeto, J. W. Li, A. S. Genshaft, S. W. Kazer, K. R. Payer, J. de Riba Borrajo, P. C. Blainey, D. J. Irvine, A. K. Shalek and S. R. Manalis, *Nat Commun*, 2016, **7**, 10220.

19   S. Ding, P. Kingshott, H. Thissen, M. Pera and P.-Y. Wang, *Biotechnol Bioeng*, 2017, **114**, 260–280.

20   J. Z. Gasiorowski, C. J. Murphy and P. F. Nealey, *Annu Rev Biomed Eng*, 2013, **15**, 155–176.

21   J. D. Kiang, J. H. Wen, J. C. del Álamo and A. J. Engler, *J Biomed Mater Res A*, 2013, **101A**, 2313–2321.

22   J. Fernández-Pérez and M. Ahearne, *Curr Eye Res*, 2019, **44**, 135–146.

23   T. Yeung, P. C. Georges, L. A. Flanagan, B. Marg, M. Ortiz, M. Funaki, N. Zahir, W. Ming, V. Weaver and P. A. Janmey, *Cell Motil Cytoskeleton*, 2005, **60**, 24–34.

24   X. Li, Z. Xiao, J. Han, L. Chen, H. Xiao, F. Ma, X. Hou, X. Li, J. Sun, W. Ding, Y. Zhao, B. Chen and J. Dai, *Biomaterials*, 2013, **34**, 5107–5116.

25   K. E. Kador, H. S. Alsehli, A. N. Zindell, L. W. Lau, F. M. Andreopoulos, B. D. Watson and J. L. Goldberg, *Acta Biomater*, 2014, **10**, 4939–4946.

26   L. Vaysse, A. Beduer, J. C. Sol, C. Vieu and I. Loubinoux, *Biomaterials*, 2015, **58**, 46–53.

27 K. Baba, W. Yoshida, M. Toriyama, T. Shimada, C. F. Manning, M. Saito, K. Kohno, J. S. Trimmer, R. Watanabe and N. Inagaki, *Elife*, 2018, **7**, e34593.

28 T. P. Kole, Y. Tseng, I. Jiang, J. L. Katz and D. Wirtz, *Mol Biol Cell*, 2005, **16**, 328–338.

29 O. Lieleg, M. M. A. E. Claessens and A. R. Bausch, *Soft Matter*, 2010, **6**, 218–225.

30 D. D. Tang and B. D. Gerlach, *Respir Res*, 2017, **18**, 54.

31 W.-C. Chen, H.-H. Lin and M.-J. Tang, *American Journal of Physiology-Renal Physiology*, 2014, **307**, F695–F707.

32 S. Dimeloe, A. Burgener, J. Grählert and C. Hess, *Immunology*, 2017, **150**, 35–44.

33 X.-W. Li, H.-Y. Gao and J. Liu, *Nutr Neurosci*, 2017, **20**, 409–415.

34 W. Markikou-Ouni, S. Drini, N. Bahi-Jaber, M. Chenik and A. Meddeb-Garnaoui, *PLoS One*, 2015, **10**, e0143063.

35 Y. Wang, G. Wang, X. Luo, J. Qiu and C. Tang, *Burns*, 2012, **38**, 414–420.

36 J. Xu, M. Sun, Y. Tan, H. Wang, H. Wang, P. Li, Z. Xu, Y. Xia, L. Li and Y. Li, *Differentiation*, 2017, **96**, 30–39.

37 M. Okabe, Y. Tsukahara, M. Tanaka, K. Suzuki, S. Saito, Y. Kamiya, T. Tsujimura, K. Nakamura and A. Miyajima, *Development*, 2009, **136**, 1951–1960.

38 M. D. Dabeva and D. A. Shafritz, *American Journal of Pathology*, 1993, **143**, 1606–1620.

39 M. Ogawa, *Blood*, 1993, **81**, 2844–2853.

40 S. J. Morrison, N. Uchida and I. L. Weissman, *Annu Rev Cell Dev Biol*, 1995, **11**, 35–71.

41 G. Y. Huang, E. S. Cooper, K. Waldo, M. L. Kirby, N. B. Gilula and C. W. Lo, *Journal of Cell Biology*, 1998, **143**, 1725–1734.

42 W.-J. Rappel, *Proceedings of the National Academy of Sciences*, 2016, **113**, 1471–1473.

43 E. Yacubova and H. Komuro, *Cell Biochem Biophys*, 2002, **37**, 213–234.

44 H. Komuro and E. Yacubova, *Cellular and Molecular Life Sciences*, 2003, **60**, 1084–1098.

45 Y. Fujiwara, N. Tanaka, O. Ishida, Y. Fujimoto, T. Murakami, H. Kajihara, Y. Yasunaga and M. Ochi, *Neurosci Lett*, 2004, **366**, 287–291.

46 X. Fu, G. Liu, A. Halim, Y. Ju, Q. Luo and G. Song, *Cells*, 2019, **8**, 784.

47 G. Taraboletti, D. D. Roberts and L. A. Liotta, *Journal of Cell Biology*, 1987, **105**, 2409–2415.

48 A. J. Perumpanani, D. L. Simmons, A. J. H. Gearing, K. M. Miller, G. Ward, J. Norbury, M. Schneemann and J. A. Sherratt, *Proc R Soc Lond B Biol Sci*, 1998, **265**, 2347–2352.

49 D. Davies, in *Flow Cytometry*, Humana Press, Totowa, NJ, 2007, pp. 257–276.

50 T. Jaatinen and J. Laine, *Curr Protoc Stem Cell Biol*, 2007, **1**, 2A.1.1-2A.1.4.

51 T. Kekarainen, S. Mannelin, J. Laine and T. Jaatinen, *BMC Cell Biol*, 2006, **7**, 30.

52 M. Li, H. Liu, S. Zhuang and K. Goda, *RSC Adv*, 2021, **11**, 20944–20960.

53 A. Lohse, *J Autoimmun*, 1996, **9**, 667–675.

54 K. Nomura and A. Komamine, *Plant Physiol*, 1985, **79**, 988–991.

55 P. F. Ray, R. M. L. Winston and A. H. Handyside, *J Assist Reprod Genet*, 1996, **13**, 104–106.

56 J. I. Baldani, V. M. Reis, S. S. Videira, L. H. Boddey and V. L. D. Baldani, *Plant Soil*, 2014, **384**, 413–431.

57 L. Bergmann, *Journal of General Physiology*, 1960, **43**, 841–851.

58 L. G. Nickell, *Proceedings of the National Academy of Sciences*, 1956, **42**, 848–850.

59 W. H. Muir, A. C. Hildebrandt and A. J. Riker, *Am J Bot*, 1958, **45**, 589–597.

60 Z. Zhu and C. J. Yang, *Acc Chem Res*, 2017, **50**, 22–31.

61 T. Kamperman, M. Karperien, S. Le Gac and J. Leijten, *Trends Biotechnol*, 2018, **36**, 850–865.

62   K. Okano, D. Yu, A. Matsui, Y. Maezawa, Y. Hosokawa, A. Kira, M. Matsubara, I. Liau, H. Tsubokawa and H. Masuhara, *ChemBioChem*, 2011, **12**, 795–801.

63   K. Okano, H. Y. Hsu, Y. K. Li and H. Masuhara, *Journal of Photochemistry and Photobiology C: Photochemistry Reviews*, 2016, **28**, 1–28.

64   H. Yamamoto, K. Okano, T. Demura, Y. Hosokawa, H. Masuhara, T. Tanii and S. Nakamura, *Appl Phys Lett*, 2011, **99**, 163701.

65   R. Peng, X. Yao and J. Ding, *Biomaterials*, 2011, **32**, 8048–8057.

66   K. Mandal, M. Balland and L. Bureau, *PLoS One*, 2012, **7**, e37548.

67   K. Shimizu, H. Fujita and E. Nagamori, *J Biosci Bioeng*, 2010, **109**, 174–178.

68   H. Yamamoto, R. Matsumura, H. Takaoki, S. Katsurabayashi, A. Hirano-Iwata and M. Niwano, *Appl Phys Lett*, 2016, **109**, 043703.

69   C. S. Chen, M. Mrksich, S. Huang, G. M. Whitesides and D. E. Ingber, *Science (1979)*, 1997, **276**, 1425–1428.

70   Y. Zhang, C. Luo, K. Zou, Z. Xie, O. Brandman, Q. Ouyang and H. Li, *PLoS One*, 2012, **7**, e48275.

71   P. Liu, T. Z. Young and M. Acar, *Cell Rep*, 2015, **13**, 634–644.

72   F.-M. Shen, L. Zhu, H. Ye, Y.-J. Yang, D.-W. Pang and Z.-L. Zhang, *Sci Rep*, 2015, **5**, 11937.

73   C. Probst, A. Grünberger, N. Braun, S. Helfrich, K. Nöh, W. Wiechert and D. Kohlheyer, *Analytical Methods*, 2015, **7**, 91–98.

74   S. W. Lim, T. M. Tran and A. R. Abate, *PLoS One*, 2015, **10**, e0113549.

75   A. Isozaki, Y. Nakagawa, M. H. Loo, Y. Shibata, N. Tanaka, D. L. Setyaningrum, J.-W. Park, Y. Shirasaki, H. Mikami, D. Huang, H. Tsoi, C. T. Riche, T. Ota, H. Miwa, Y. Kanda, T. Ito, K. Yamada, O. Iwata, K. Suzuki, S. Ohnuki, Y. Ohya, Y. Kato, T.

Hasunuma, S. Matsusaka, M. Yamagishi, M. Yazawa, S. Uemura, K. Nagasawa, H. Watarai, D. di Carlo and K. Goda, *Sci Adv*, 2020, **6**, eaba6712.

76   Q. Zhang, T. Wang, Q. Zhou, P. Zhang, Y. Gong, H. Gou, J. Xu and B. Ma, *Sci Rep*, 2017, **7**, 41192.

77   N.-D. Dinh, Y.-Y. Chiang, H. Hardelauf, J. Baumann, E. Jackson, S. Waide, J. Sisnaiske, J.-P. Frimat, C. van Thriel, D. Janasek, J.-M. Peyrin and J. West, *Lab Chip*, 2013, **13**, 1402–1412.

78   J. Feng, Z. Fohlerová, X. Liu, H. Chang and P. Neužil, *Sens Actuators B Chem*, 2018, **269**, 288–292.

79   N. Ota, Y. Yalikun, N. Tanaka, Y. Shen, Y. Aishan, Y. Nagahama, M. Oikawa and Y. Tanaka, *Analytical Sciences*, 2019, **35**, 577–583.

80   W. Tonomura, H. Moriguchi, Y. Jimbo and S. Konishi, *Biomed Microdevices*, 2010, **12**, 737–743.

81   Y. R. F. Schmid, S. C. Bürgel, P. M. Misun, A. Hierlemann and O. Frey, *ACS Sens*, 2016, **1**, 1028–1035.

82   C. Dusny, A. Grünberger, C. Probst, W. Wiechert, D. Kohlheyer and A. Schmid, *Lab Chip*, 2015, **15**, 1822–1834.

83   C. Dusny, M. Lohse, T. Reemtsma, A. Schmid and O. J. Lechtenfeld, *Anal Chem*, 2019, **91**, 7012–7018.

84   Q. Huang, S. Mao, M. Khan, W. Li, Q. Zhang and J.-M. Lin, *Chem Sci*, 2020, **11**, 253–256.

85   H. E. Karakas, J. Kim, J. Park, J. M. Oh, Y. Choi, D. Gozuacik and Y.-K. Cho, *Sci Rep*, 2017, **7**, 2050.

86   B. Çetin and D. Li, *Electrophoresis*, 2011, **32**, 2410–2427.

87   Z. Zhang, T. E. P. Kimkes and M. Heinemann, *Sci Rep*, 2019, **9**, 1–9.

88   C. Probst, A. Grünberger, W. Wiechert and D. Kohlheyer, *J Microbiol Methods*, 2013, **95**, 470–476.

89   Y. Hosokawa, S. Iguchi, R. Yasukuni, Y. Hiraki, C. Shukunami and H. Masuhara, *Appl Surf Sci*, 2009, **255**, 9880–9884.

90   T. Kaji, S. Ito, H. Miyasaka, Y. Hosokawa, H. Masuhara, C. Shukunami and Y. Hiraki, *Appl Phys Lett*, 2007, **91**, 023904.

91   K. Okano, A. Matsui, Y. Maezawa, P. Y. Hee, M. Matsubara, H. Yamamoto, Y. Hosokawa, H. Tsubokawa, Y. K. Li, F. J. Kao and H. Masuhara, *Lab Chip*, 2013, **13**, 4078–4086.

92   T. I. Rukmana, G. Moran, R. Méallet-Renault, M. Ohtani, T. Demura, R. Yasukuni and Y. Hosokawa, *Sci Rep*, 2019, **9**, 17530.

93   Y. Hosokawa, *Jpn J Appl Phys*, 2019, 58, 110102.

94   D. Anggraini, K. Okano, Y. Tanaka, S. Yamada, Y. Yalikun and Y. Hosokawa, in *Proceedings of the IEEE International Conference on Micro Electro Mechanical Systems (MEMS)*, Institute of Electrical and Electronics Engineers Inc., 2021, vol. 2021-January, pp. 1001–1004.

95   D. Anggraini, X. Liu, K. Okano, Y. Tanaka, N. Inagaki, M. Li, Y. Hosokawa, S. Yamada and Y. Yalikun, *bioRxiv*, 2021, DOI:10.1101/2021.08.17.456633.

96   Y. Yalikun, Y. Hosokawa, T. Iino and Y. Tanaka, *Lab Chip*, 2016, **16**, 2427–2433.

97   Y. Yalikun, N. Tanaka, Y. Hosokawa, T. Iino and Y. Tanaka, *Biomed Microdevices*, 2017, **19**, 85.

98   Y. Yalikun, N. Tanaka, Y. Hosokawa, T. Iino and Y. Tanaka, *Applied Physics Express*, 2016, **9**, 006702.

99   T. Zhang, M. Namoto, K. Okano, E. Akita, N. Teranishi, T. Tang, D. Anggraini, Y. Hao, Y. Tanaka, D. Inglis, Y. Yalikun, M. Li and Y. Hosokawa, *Sci Rep*, 2021, **11**, 1652.

100 J. N. Lee, X. Jiang, D. Ryan and G. M. Whitesides, *Langmuir*, 2004, **20**, 11684–11691.

101 J. M. Łopacińska, J. Emnéus and M. Dufva, *PLoS One*, 2013, **8**, e53107.

102 Y. Tanaka, K. Sato, T. Shimizu, M. Yamato, T. Okano, I. Manabe, R. Nagai and T. Kitamori, *Lab Chip*, 2008, **8**, 58–61.

103 A. P. Hsiao, K. D. Barbee and X. Huang, in *Proceedings of SPIE-The International Society for Optical Engineering*, 2010, vol. 7759, pp. 104–112.

104 Nianzhen Li, M. Schwartz and C. Ionescu-Zanetti, *J Biomol Screen*, 2009, **14**, 194–202.

105 K. Y. Chumbimuni-Torres, R. E. Coronado, A. M. Mfuh, C. Castro-Guerrero, M. F. Silva, G. R. Negrete, R. Bizios and C. D. Garcia, *RSC Adv*, 2011, **1**, 706–714.

106 N. Xu, Z.-F. Zhang, L. Wang, B. Gao, D.-W. Pang, H.-Z. Wang and Z.-L. Zhang, *Biomicrofluidics*, 2012, **6**, 034122.

107 K. Chandran, D. L. Farsetta and M. L. Nibert, *J Virol*, 2002, **76**, 9920–9933.

108 T. Wang, J. Chen, T. Zhou and L. Song, *Micromachines (Basel)*, 2018, **9**, 269.

109 M. Arundell, V. H. Perry and T. A. Newman, *Lab Chip*, 2011, **11**, 3001–3005.

110 K. C. Spencer, J. C. Sy, R. Falcón-Banchs and M. J. Cima, *Lab Chip*, 2017, **17**, 795–804.

111 K. G. Vandervoort and G. Brelles-Mariño, *PLoS One*, 2014, **9**, e108512.

112 M. Ojansivu, A. Mishra, S. Vanhatupa, M. Juntunen, A. Larionova, J. Massera and S. Miettinen, *PLoS One*, 2018, **13**, e0202740.

113 A. C. Barbati, C. Fang, G. A. Banker and B. J. Kirby, *Biomed Microdevices*, 2013, **15**, 97–108.

114 S. Fan, J. Sun, W. Xing, C. Li and D. Wang, *J Appl Math*, 2013, **2013**, 1–13.

115 C. Probst, A. Grünberger, W. Wiechert and D. Kohlheyer, *Micromachines (Basel)*, 2013, **4**, 357–369.

116   C. S. Bascom, S.-Z. Wu, K. Nelson, J. Oakey and M. Bezanilla, *Plant Physiol*, 2016, **172**, 28–37.

117   T. Xu, Y. Gong, X. Su, P. Zhu, J. Dai, J. Xu and B. Ma, *Small*, 2020, **16**, 2001172.

118   Y. Shirokawa and M. Shimada, *Proceedings of the Royal Society B: Biological Sciences*, 2013, **280**, 20130503.

119   K. Rosenthal, F. Falke, O. Frick, C. Dusny and A. Schmid, *Micromachines (Basel)*, 2015, **6**, 1836–1855.

120   H. Kim, I.-K. Lee, K. Taylor, K. Richters, D.-H. Baek, J. H. Ryu, S. J. Cho, Y. H. Jung, D.-W. Park, J. Novello, J. Bong, A. J. Suminski, A. M. Dingle, R. H. Blick, J. C. Williams, E. W. Dent and Z. Ma, *Sci Rep*, 2018, **8**, 13194.

121   Y. Yalikun and Y. Tanaka, *Micromachines (Basel)*, 2016, **7**, 83.

122   J.-S. Oh, S. Kojima, M. Sasaki, A. Hatta and S. Kumagai, *Sci Rep*, 2017, **7**, 41953.

123   Y. Shirokawa and M. Shimada, *Proceedings of the Royal Society B: Biological Sciences*, 2013, **280**, 20130503.

124   D. Anggraini, N. Ota, Y. Shen, T. Tang, Y. Tanaka, Y. Hosokawa, M. Li and Y. Yalikun, *Lab Chip*, 2022, **22**, 1438–1468.

125   L. Dong, D.-W. Chen, S.-J. Liu and W. Du, *Sci Rep*, 2016, **6**, 24192.

126   M. Sesen and G. Whyte, *Sci Rep*, 2020, **10**, 8736.

127   S. C. C. Shih, P. C. Gach, J. Sustarich, B. A. Simmons, P. D. Adams, S. Singh and A. K. Singh, *Lab Chip*, 2015, **15**, 225–236.

128   R. Zilionis, J. Nainys, A. Veres, V. Savova, D. Zemmour, A. M. Klein and L. Mazutis, *Nat Protoc*, 2017, **12**, 44–73.

129   H. Liu, X. Xu, K. Peng, Y. Zhang, L. Jiang, T. C. Williams, I. T. Paulsen, J. A. Piper and M. Li, *Biotechnol Bioeng*, 2020, **118**, 647–658.

130   A. E. Fischer, S. K. Wu, J. B. G. Proescher, A. Rotem, C. B. Chang, H. Zhang, Y. Tao, T. S. Mehoke, P. M. Thielen, A. O. Kolawole, T. J. Smith, C. E. Wobus, D. A. Weitz, J. S. Lin, A. B. Feldman and J. T. Wolfe, *J Virol Methods*, 2015, **213**, 111–117.

131   S. S. Terekhov, I. v. Smirnov, M. v. Malakhova, A. E. Samoilov, A. I. Manolov, A. S. Nazarov, D. v. Danilov, S. A. Dubiley, I. A. Osterman, M. P. Rubtsova, E. S. Kostryukova, R. H. Ziganshin, M. A. Kornienko, A. A. Vanyushkina, O. N. Bukato, E. N. Ilina, V. v. Vlasov, K. v. Severinov, A. G. Gabibov and S. Altman, *Proceedings of the National Academy of Sciences*, 2018, **115**, 9551–9556.

132   B. Hu, B. Xu, J. Yun, J. Wang, B. Xie, C. Li, Y. Yu, Y. Lan, Y. Zhu, X. Dai, Y. Huang, L. Huang, J. Pan and W. Du, *Lab Chip*, 2020, **20**, 363–372.

133   D. Sengupta, A. Mongersun, T. J. Kim, K. Mongersun, R. von Eyben, P. Abbyad and G. Pratx, *Technol Cancer Res Treat*, 2019, **18**, 1–9.

134   A. Dewan, J. Kim, R. H. McLean, S. A. Vanapalli and M. N. Karim, *Biotechnol Bioeng*, 2012, **109**, 2987–2996.

135   L. Mazutis, J. Gilbert, W. L. Ung, D. A. Weitz, A. D. Griffiths and J. A. Heyman, *Nat Protoc*, 2013, **8**, 870–891.

136   A. Grünberger, C. Probst, S. Helfrich, A. Nanda, B. Stute, W. Wiechert, E. von Lieres, K. Nöh, J. Frunzke and D. Kohlheyer, *Cytometry Part A*, 2015, **87**, 1101–1115.

137   S. Stratz, P. E. Verboket, K. Hasler and P. S. Dittrich, *Electrophoresis*, 2018, **39**, 540–547.

138   S. Demming, B. Sommer, A. Llobera, D. Rasch, R. Krull and S. Büttgenbach, *Biomicrofluidics*, 2011, **5**, 014104.

139   D. Lindemann, C. Westerwalbesloh, D. Kohlheyer, A. Grünberger and E. von Lieres, *RSC Adv*, 2019, **9**, 14040–14050.

140 T. Geng, C. R. Smallwood, E. L. Bredeweg, K. R. Pomraning, A. E. Plymale, S. E. Baker, J. E. Evans and R. T. Kelly, *Biomicrofluidics*, 2017, **11**, 054104.

141 S. Li, C. B. Jendresen, A. Grünberger, C. Ronda, S. I. Jensen, S. Noack and A. T. Nielsen, *Metab Eng*, 2016, **38**, 274–284.

142 F. S. O. Fritzsch, K. Rosenthal, A. Kampert, S. Howitz, C. Dusny, L. M. Blank and A. Schmid, *Lab Chip*, 2013, **13**, 397–408.

143 C.-H. Lin, Y.-H. Hsiao, H.-C. Chang, C.-F. Yeh, C.-K. He, E. M. Salm, C. Chen, I.-M. Chiu and C.-H. Hsu, *Lab Chip*, 2015, **15**, 2928–2938.

144 K. Okano, A. Matsui, Y. Maezawa, P. Y. Hee, M. Matsubara, H. Yamamoto, Y. Hosokawa, H. Tsubokawa, Y. K. Li, F. J. Kao and H. Masuhara, *Lab Chip*, 2013, **13**, 4078–4086.

145 Y. Hosokawa, M. Hagiyama, T. Iino, Y. Murakami and A. Ito, *Proceedings of the National Academy of Sciences*, 2011, **108**, 1777–1782.

146 K. Oikawa, S. Matsunaga, S. Mano, M. Kondo, K. Yamada, M. Hayashi, T. Kagawa, A. Kadota, W. Sakamoto, S. Higashi, M. Watanabe, T. Mitsui, A. Shigemasa, T. Iino, Y. Hosokawa and M. Nishimura, *Nat Plants*, 2015, **1**, 1–12.

147 C. Hosokawa, S. N. Kudoh, A. Kiyohara, Y. Hosokawa, K. Okano, H. Masuhara and T. Taguchi, *Appl Phys A Mater Sci Process*, 2008, **93**, 57–63.

148 Y. Hosokawa, H. Takabayashi, S. Miura, C. Shukunami, Y. Hiraki and H. Masuhara, *Appl Phys A Mater Sci Process*, 2004, **79**, 795–798.

149 Y. Maezawa, Y. Hosokawa, K. Okano, M. Matsubara and H. Masuhara, *Appl Phys A Mater Sci Process*, 2010, **101**, 127–131.

150 Y. Maezawa, K. Okano, M. Matsubara, H. Masuhara and Y. Hosokawa, *Biomed Microdevices*, 2011, **13**, 117–122.

151 K. Okano, L. L. Liu, Y. Hosokawa and H. Masuhara, in *International Symposium on Micro-NanoMechatronics and Human Science (MHS)*, 2016, pp. 1–5.

152 H. Lubatschowski, A. Heisterkamp, F. Will, A. I. Singh, J. Serbin, A. Ostendorf, O. Kermani, R. Heermann, H. Welling and W. Ertmer, *RIKEN Review*, 2003, **50**, 113–118.

153 H. K. Soong and J. B. Malta, *Am J Ophthalmol*, 2009, **147**, 189–197.

154 Y. Hosokawa, H. Ochi, T. Iino, A. Hiraoka and M. Tanaka, *PLoS One*, 2011, **6**, e27677.

155 Y. Hosokawa, S. Iguchi, R. Yasukuni, Y. Hiraki, C. Shukunami and H. Masuhara, *Appl Surf Sci*, 2009, **255**, 9880–9884.

156 K. Okano, C. H. Wang, Z. Y. Hong, Y. Hosokawa and I. Liau, *Biochem Biophys Rep*, 2020, **24**, 100818.

157 J. Buechler and P. C. Salinas, *Front Synaptic Neurosci*, 2018, **10**, 38.

158 I. Vertkin, B. Styr, E. Slomowitz, N. Ofir, I. Shapira, D. Berner, T. Fedorova, T. Laviv, N. Barak-Broner, D. Greitzer-Antes, M. Gassmann, B. Bettler, I. Lotan and I. Slutsky, *Proceedings of the National Academy of Sciences*, 2015, **112**, E3291–E3299.

159 M. B. Ramocki and H. Y. Zoghbi, *Nature*, 2008, **455**, 912–918.

160 P. Riess, C. Zhang, K. E. Saatman, H. L. Laurer, L. G. Longhi, R. Raghupathi, P. M. Lenzlinger, J. Lifshitz, J. Boockvar, E. Neugebauer, E. Y. Snyder and T. K. McIntosh, *Neurosurgery*, 2002, **51**, 1043–1054.

161 D. A. Shear, M. C. Tate, D. R. Archer, S. W. Hoffman, V. D. Hulce, M. C. Laplaca and D. G. Stein, *Brain Res*, 2004, **1026**, 11–22.

162 D. D. Pearse, F. C. Pereira, A. E. Marcillo, M. L. Bates, Y. A. Berrocal, M. T. Filbin and M. B. Bunge, *Nat Med*, 2004, **10**, 610–616.

163 G. W. J. Hawryluk, S. Spano, D. Chew, S. Wang, M. Erwin, M. Chamankhah, N. Forgione and M. G. Fehlings, *Cell Transplant*, 2014, **23**, 365–380.

164   Y. Fan, F. Shen, T. Frenzel, W. Zhu, J. Ye, J. Liu, Y. Chen, H. Su, W. L. Young and G. Y. Yang, *Ann Neurol*, 2010, **67**, 488–497.

165   D. Kondziolka, L. Wechsler, S. Goldstein, C. Meltzer, K. R. Thulborn, J. Gebel, P. Jannetta, S. DeCesare, E. M. Elder, M. McGrogan, M. A. Reitman and L. Bynum, *Neurology*, 2000, **55**, 565–569.

166   J. C. Shin, K. N. Kim, J. Yoo, I.-S. Kim, S. Yun, H. Lee, K. Jung, K. Hwang, M. Kim, I.-S. Lee, J. E. Shin and K. I. Park, *Neural Plast*, 2015, **2015**, 1–22.

167   M. Vroemen, L. Aigner, J. Winkler and N. Weidner, *European Journal of Neuroscience*, 2003, **18**, 743–751.

168   G. W. J. Hawryluk, S. Spano, D. Chew, S. Wang, M. Erwin, M. Chamankhah, N. Forgione and M. G. Fehlings, *Cell Transplant*, 2014, **23**, 365–380.

169   D. A. Shear, M. C. Tate, D. R. Archer, S. W. Hoffman, V. D. Hulce, M. C. Laplaca and D. G. Stein, *Brain Res*, 2004, **1026**, 11–22.

170   Y. Fan, F. Shen, T. Frenzel, W. Zhu, J. Ye, J. Liu, Y. Chen, H. Su, W. L. Young and G. Y. Yang, *Ann Neurol*, 2010, **67**, 488–497.

171   K. Yokota, K. Kobayakawa, K. Kubota, A. Miyawaki, H. Okano, Y. Ohkawa, Y. Iwamoto and S. Okada, *Stem Cell Reports*, 2015, **5**, 264–277.

172   E. R. Hollis, N. Ishiko, M. Pessian, K. Tolentino, C. A. Lee-Kubli, N. A. Calcutt and Y. Zou, *Nat Commun*, 2015, **6**, 6079.

173   K. Steece-Collier, D. J. Rademacher and K. E. Soderstrom, *Basal Ganglia*, 2012, **2**, 15–30.

174   L. Vaysse, A. Beduer, J. C. Sol, C. Vieu and I. Loubinoux, *Biomaterials*, 2015, **58**, 46–53.

175   A. L. Carlson, N. K. Bennett, N. L. Francis, A. Halikere, S. Clarke, J. C. Moore, R. P. Hart, K. Paradiso, M. Wernig, J. Kohn, Z. P. Pang and P. v. Moghe, *Nat Commun*, 2016, **7**, 10862.

176   S. Zhang, X. J. Wang, W. S. Li, X. L. Xu, J. B. Hu, X. Q. Kang, J. Qi, X. Y. Ying, J. You and Y. Z. Du, *Acta Biomater*, 2018, **77**, 15–27.

177   L. J. Millet, M. E. Stewart, R. G. Nuzzo and M. U. Gillette, *Lab Chip*, 2010, **10**, 1525–1535.

178   A. Gladkov, Y. Pigareva, D. Kutyina, V. Kolpakov, A. Bukatin, I. Mukhina, V. Kazantsev and A. Pimashkin, *Sci Rep*, 2017, **7**, 1–14.

179   M. J. Jang and Y. Nam, *J Neural Eng*, 2012, **9**, 046019.

180   T. M. Dinis, R. Elia, G. Vidal, A. Auffret, D. L. Kaplan and C. Egles, *ACS Appl Mater Interfaces*, 2014, **6**, 16817–16826.

181   K. E. Kador, S. P. Grogan, E. W. Dorthé, P. Venugopalan, M. F. Malek, J. L. Goldberg and D. D. D'lima, *Tissue Eng Part A*, 2016, **22**, 286–294.

182   A. L. Carlson, N. K. Bennett, N. L. Francis, A. Halikere, S. Clarke, J. C. Moore, R. P. Hart, K. Paradiso, M. Wernig, J. Kohn, Z. P. Pang and P. V. Moghe, *Nat Commun*, 2016, **7**, 10862.

183   S. Zhang, X. J. Wang, W. S. Li, X. L. Xu, J. B. Hu, X. Q. Kang, J. Qi, X. Y. Ying, J. You and Y. Z. Du, *Acta Biomater*, 2018, **77**, 15–27.

184   T. C. Yang, J. H. Chuang, W. Buddhakosai, W. J. Wu, C. J. Lee, W. S. Chen, Y. P. Yang, M. C. Li, C. H. Peng and S. J. Chen, *Int J Mol Sci*, 2017, **18**, 2013.

185   K. E. Kador, S. P. Grogan, E. W. Dorthé, P. Venugopalan, M. F. Malek, J. L. Goldberg and D. D. D'lima, *Tissue Eng Part A*, 2016, **22**, 286–294.

186   J. Xie, M. R. MacEwan, A. G. Schwartz and Y. Xia, *Nanoscale*, 2010, **2**, 35–44.

187   J. Qu, D. Wang, H. Wang, Y. Dong, F. Zhang, B. Zuo and H. Zhang, *J Biomed Mater Res A*, 2013, **101**, 2667–2678.

188   H. B. Wang, M. E. Mullins, J. M. Cregg, C. W. McCarthy and R. J. Gilbert, *Acta Biomater*, 2010, **6**, 2970–2978.

189   J. Xie, W. Liu, M. R. Macewan, P. C. Bridgman and Y. Xia, *ACS Nano*, 2014, **8**, 1878–1885.

190   J. Xue, J. Yang, D. M. O'Connor, C. Zhu, D. Huo, N. M. Boulis and Y. Xia, *ACS Appl Mater Interfaces*, 2017, **9**, 12299–12310.

191   Y. Edagawa, J. Nakanishi, K. Yamaguchi and N. Takeda, *Colloids Surf B Biointerfaces*, 2012, **99**, 20–26.

192   B. W. Tuft, L. Xu, S. P. White, A. E. Seline, A. M. Erwood, M. R. Hansen and C. Allan Guymon, *ACS Appl Mater Interfaces*, 2014, **6**, 11265–11276.

193   L. V. J. Behm, S. Gerike, M. K. Grauel, K. Uhlig, F. Pfisterer, W. Baumann, F. F. Bier, C. Duschl and M. Kirschbaum, *ACS Appl Bio Mater*, 2019, **2**, 2853–2861.

194   J. M. Lee, J. Y. Moon, T. H. Kim, S. W. Lee, C. D. Ahrberg and B. G. Chung, *Sens Actuators B Chem*, 2018, **258**, 1042–1050.

195   C. Li, M. Kuss, Y. Kong, F. Nie, X. Liu, B. Liu, A. Dunaevsky, P. Fayad, B. Duan and X. Li, *ACS Biomater Sci Eng*, 2021, **7**, 690–700.

196   H. S. Lee, E. Y. Jeon, J. J. Nam, J. H. Park, I. C. Choi, S. H. Kim, J. J. Chung, K. Lee, J. W. Park and Y. Jung, *Acta Biomater*, 2022, **141**, 219–232.

197   N. Bhattacharjee and A. Folch, *Microsyst Nanoeng*, 2017, **3**, 1–14.

198   N. Bhattacharjee, N. Li, T. M. Keenan and A. Folch, *Integrative Biology*, 2010, **2**, 669–679.

199   N. Ishii, W. G. Wadsworth, B. D. Stern, J. G. Culotti and E. M. Hedgecock, *Neuron*, 1992, **9**, 873–881.

200 T. Serafini, T. E. Kennedy, M. J. Gaiko, C. Mirzayan, T. M. Jessell and M. Tessier-Lavigne, *Cell*, 1994, **78**, 409–424.

201 Y. Yuan, Y. Yalikun, S. Amaya, Y. Aishan, Y. Shen and Y. Tanaka, *Sens Actuators A Phys*, 2021, **321**, 112604.

202 S. Nakamura, N. Takayama, S. Hirata, H. Seo, H. Endo, K. Ochi, K. I. Fujita, T. Koike, K. I. Harimoto, T. Dohda, A. Watanabe, K. Okita, N. Takahashi, A. Sawaguchi, S. Yamanaka, H. Nakauchi, S. Nishimura and K. Eto, *Cell Stem Cell*, 2014, **14**, 535–548.

203 H. Yamamoto, K. Okano, T. Demura, Y. Hosokawa, H. Masuhara, T. Tanii and S. Nakamura, *Appl Phys Lett*, 2011, **99**, 163701.

204 T. C. Yang, J. H. Chuang, W. Buddhakosai, W. J. Wu, C. J. Lee, W. S. Chen, Y. P. Yang, M. C. Li, C. H. Peng and S. J. Chen, *Int J Mol Sci*, 2017, **18**, 2013.

205 L. Shi, D. Kuhnell, V. J. Borra, S. M. Langevin, T. Nakamura and L. Esfandiari, *Lab Chip*, 2019, **19**, 3726–3734.

206 A. Homsy, E. Laux, J. Brossard, H. J. Whitlow, M. Roccio, S. Hahnewald, P. Senn, P. Mistrík, R. Hessler, T. Melchionna, C. Frick, H. Löwenheim, M. Müller, U. Wank, K.-H. Wiesmüller and H. Keppner, *Hearing Balance Commun*, 2015, **13**, 153–159.

207 R. R. Xiao, W. J. Zeng, Y. T. Li, W. Zou, L. Wang, X. F. Pei, M. Xie and W. H. Huang, *Anal Chem*, 2013, **85**, 7842–7850.

208 N. Bhattacharjee and A. Folch, *Microsyst Nanoeng*, 2017, **3**, 1–14.

209 S. W. Nam, D. Van Noort, Y. Yang and S. Park, *Lab Chip*, 2007, **7**, 638–640.

210 C. Y. Chen, A. M. Wo and D. S. Jong, *Lab Chip*, 2012, **12**, 794–801.

211 L. J. Millet, M. E. Stewart, R. G. Nuzzo and M. U. Gillette, *Lab Chip*, 2010, **10**, 1525–1535.

212 C. R. Kothapalli, E. van Veen, S. de Valence, S. Chung, I. K. Zervantonakis, F. B. Gertler and R. D. Kamm, *Lab Chip*, 2011, **11**, 497–507.

213 A. Blasiak, G. U. Lee and D. Kilinc, *ACS Chem Neurosci*, 2015, **6**, 1578–1590.

214 Z. Xu, P. Fang, B. Xu, Y. Lu, J. Xiong, F. Gao, X. Wang, J. Fan and P. Shi, *Nat Commun*, 2018, **9**, 4745.

215 A. M. Taylor, S. Menon and S. L. Gupton, *Lab Chip*, 2015, **15**, 2781–2789.

216 R. R. Xiao, W. J. Zeng, Y. T. Li, W. Zou, L. Wang, X. F. Pei, M. Xie and W. H. Huang, *Anal Chem*, 2013, **85**, 7842–7850.

217 N. Bhattacharjee and A. Folch, *Microsyst Nanoeng*, 2017, **3**, 17003.

218 T. Serafini, T. E. Kennedy, M. J. Gaiko, C. Mirzayan, T. M. Jessell and M. Tessier-Lavigne, *Cell*, 1994, **78**, 409–424.

219 S. W. Moore, X. Zhang, C. D. Lynch and M. P. Sheetz, *Journal of Neuroscience*, 2012, **32**, 11574–11585.

220 S. W. Moore, N. Biais and M. P. Sheetz, *Science (1979)*, 2009, **325**, 166.

221 K. E. Kador, H. S. Alsehli, A. N. Zindell, L. W. Lau, F. M. Andreopoulos, B. D. Watson and J. L. Goldberg, *Acta Biomater*, 2014, **10**, 4939–4946.

222 J. Xue, T. Wu, J. Qiu and Y. Xia, *Small Methods*, 2020, **4**, 2000125.

223 C. Liu, X. Li, F. Xu, H. Cong, Z. Li, Y. Song and M. Wang, *J Mater Sci Mater Med*, 2018, **29**, 1–13.

224 B. Black, V. Vishwakarma, K. Dhakal, S. Bhattarai, P. Pradhan, A. Jain, Y. T. Kim and S. Mohanty, *Sci Rep*, 2016, **6**, 29876.

225 K. Oyama, V. Zeeb, Y. Kawamura, T. Arai, M. Gotoh, H. Itoh, T. Itabashi, M. Suzuki and S. Ishiwata, *Sci Rep*, 2015, **5**, 16611.

226 K. Keino-Masu, M. Masu, L. Hinck, E. D. Leonardo, S. S.-Y. Chan, J. G. Culotti and M. Tessier-Lavigne, *Cell*, 1996, **87**, 175–185.

227 G. L. Ming, H. J. Song, B. Berninger, C. E. Holt, M. Tessier-Lavigne and M. M. Poo, *Neuron*, 1997, **19**, 1225–1235.

228   L. Finci, Y. Zhang, R. Meijers and J. H. Wang, *Prog Biophys Mol Biol*, 2015, 118, 153–160.

229   C. Rigato, R. Buckinx, H. Le-Corronc, J. M. Rigo and P. Legendre, *Glia*, 2011, **59**, 675–695.

230   K. Hong, L. Hinck, M. Nishiyama, M.-M. Poo, M. Tessier-Lavigne and E. Stein, *Cell*, 1999, **97**, 927–941.

231   J. Tong, M. Killeen, R. Steven, K. L. Binns, J. Culotti and T. Pawson, *Journal of Biological Chemistry*, 2001, **276**, 40917–40925.

232   J. Y. Hua and S. J. Smith, *Nat Neurosci*, 2004, **7**, 327–332.

233   C. N. Parkhurst and W. B. Gan, *Curr Opin Neurobiol*, 2010, **20**, 595–600.

234   N. F. Hassan, S. Rifat, D. E. Campbell, L. J. McCawley and S. D. Douglas, *J Leukoc Biol*, 1991, **50**, 86–92.

235   M. Heiman, A. Schaefer, S. Gong, J. D. Peterson, M. Day, K. E. Ramsey, M. Suárez-Fariñas, C. Schwarz, D. A. Stephan, D. J. Surmeier, P. Greengard and N. Heintz, *Cell*, 2008, **135**, 738–748.

236   E. Sanz, L. Yang, T. Su, D. R. Morris, G. S. Mcknight and P. S. Amieux, *Proceedings of the National Academy of Sciences*, 2009, **106**, 13939–13944.

237   E. P. R. Iyer and D. N. Cox, *Journal of Visualized Experiments*, 2010, e2016.

238   R. Waller, M. N. Woodroofe, S. Francese, P. R. Heath, S. B. Wharton, P. G. Ince, B. Sharrack and J. E. Simpson, *J Neurosci Methods*, 2012, **208**, 108–113.

239   K. Kaushansky, *Blood*, 2008, **111**, 981–986.

240   M. Cremer, H. Sallmon, P. J. Kling, C. Bührer and C. Dame, *Semin Fetal Neonatal Med*, 2016, **21**, 10–18.

241   L. Lieberman, R. S. Bercovitz, N. S. Sholapur, N. M. Heddle, S. J. Stanworth and D. M. Arnold, *Blood*, 2014, **123**, 1146–1151.

242   S. Nahirniak, S. J. Slichter, S. Tanael, P. Rebulla, K. Pavenski, R. Vassallo, M. Fung, R. Duquesnoy, C. L. Saw, S. Stanworth, A. Tinmouth, H. Hume, A. Ponnampalam, C. Moltzan, B. Berry, N. Shehata, S. Allard, D. Anderson, C. Bianco, J. Callum, V. Compernolle, D. Fergusson, A. Eder, A. Greinacher, M. Murphy, J. Pink, Z. M. Szczepiorkowski, L. Whitman and E. Wood, *Transfus Med Rev*, 2015, **29**, 3–13.

243   N. A. Murray, L. J. Howarth, M. P. Mccloy, E. A. Letsky and I. A. G. Roberts, *Transfusion Medicine*, 2002, **12**, 35–41.

244   Y. Xu, I. Kashiwakura and T. A. Takahashi, *Bone Marrow Transplant*, 2004, **34**, 537–543.

245   N. C. Shabrani, N. F. Q. Khan, V. P. Kale and L. S. Limaye, *Cytotherapy*, 2012, **14**, 366–380.

246   N. Sasayama, I. Kashiwakura, Y. Tokushima, Y. Xu, S. Wada, M. Murakami, Y. Hayase, Y. Takagi and T. A. Takahashi, *Cytotherapy*, 2001, **3**, 117–126.

247   M. Pick, A. Eldor, D. Grisaru, A. R. Zander, M. Shenhav and V. R. Deutsch, *Exp Hematol*, 2002, **30**, 1079–1087.

248   R. F. Levine, *Blood*, 1977, **50**, 713–725.

249   D. Metcalf, H. R. Macdonald, N. Odartchenko and B. Sordat, *Proceedings of the National Academy of Sciences*, 1975, **72**, 1744–1748.

250   Y. Ito, S. Nakamura, N. Sugimoto, T. Shigemori, Y. Kato, M. Ohno, S. Sakuma, K. Ito, H. Kumon, H. Hirose, H. Okamoto, M. Nogawa, M. Iwasaki, S. Kihara, K. Fujio, T. Matsumoto, N. Higashi, K. Hashimoto, A. Sawaguchi, K. ichi Harimoto, M. Nakagawa, T. Yamamoto, M. Handa, N. Watanabe, E. Nishi, F. Arai, S. Nishimura and K. Eto, *Cell*, 2018, **174**, 636–648.

251   Z. Tang, Y. Akiyama, K. Itoga, J. Kobayashi, M. Yamato and T. Okano, *Biomaterials*, 2012, **33**, 7405–7411.

252 K. Fukumori, Y. Akiyama, Y. Kumashiro, J. Kobayashi, M. Yamato, K. Sakai and T. Okano, *Macromol Biosci*, 2010, **10**, 1117–1129.

253 Y. Hayashi, J. Matsumoto, S. Kumagai, K. Morishita, L. Xiang, Y. Kobori, S. Hori, M. Suzuki, T. Kanamori, K. Hotta and K. Sumaru, *Commun Biol*, 2018, **1**, 218.

254 M. R. Koller, E. G. Hanania, J. Stevens, T. M. Eisfeld, G. C. Sasaki, A. Fieck and B. Palsson, *Cytometry Part A*, 2004, **61**, 153–161.

255 N. Lin, J. R. Cresswell, G. A. Richardson, M. A. Gerber and K. J. Kayser, *Curr Protoc Cytom*, 2008, **43**, 2–14.

256 P. Szaniszlo, W. A. Rose, N. Wang, L. M. Reece, T. v. Tsulaia, E. G. Hanania, C. J. Elferink and J. F. Leary, *Cytometry Part A*, 2006, **69**, 641–651.

257 C. Kojima, Y. Nakajima, N. Oeda, T. Kawano and Y. Taki, *Macromol Biosci*, 2017, **17**, 1600341.

258 D. Anggraini, W. Mubarok, Y. Hosokawa, K. Eto, S. Suetsugu and Y. Yalikun, *Applied Physics Express*, 2022, DOI:10.35848/1882-0786/ac8f17.

259 P. Kunda, A. E. Pelling, T. Liu and B. Baum, *Current Biology*, 2008, **18**, 91–101.

260 R. Matzke, K. Jacobson and M. Radmacher, *Nat Cell Biol*, 2001, **3**, 607–610.

261 O. O. Adeniba, E. A. Corbin, A. Ganguli, Y. Kim and R. Bashir, *Sci Rep*, 2020, **10**, 12803.

Achievements

PUBLICATIONS

Journal Articles

1. **Anggraini D**, Ota N, Shen Y, Tang T, Tanaka Y, Hosokawa Y, Li M, Yalikun Y. Recent advances in microfluidic devices for single-cell cultivation: methods and applications. 2022. Lab on a Chip. 22(8):1438-1468. (Chapter 1)

2. **Anggraini D**, Mubarok W, Hosokawa Y, Eto K, Suetsugu S, Yalikun Y. Reverse sorting of immortalized megakaryocyte progenitor cell lines (imMKCLs) by femtosecond laser scanning. 2022. Applied Physics Express. (Chapter 2 and 5)

3. **Anggraini D**, Liu X, Okano K, Tanaka Y, Inagaki N, Li M, Hosokawa Y, Yamada S, Yalikun Y. Guided Axon Outgrowth of Neurons by Molecular Gradients Generated from Femtosecond Laser-Fabricated Micro-holes. Lab on a Chip. (*Under review*). (Chapter 2, 3, and 4)

Proceedings

Anggraini D, Okano K, Tanaka Y, Yamada S, Yalikun Y, Hosokawa Y. In Situ Guided Neurite Outgrowth by Femtosecond Laser Processing in a Microfluidic Device. In 2021 IEEE 34th International Conference on Micro Electro Mechanical Systems (MEMS) 2021 Jan 25 (pp. 1001-1004). IEEE. (Chapter 2 and 3)

Handbooks

Anggraini D, Ota N, Shen Y, Tanaka Y, Hosokawa Y, Li M, Yalikun Y. Single-Cell Cultivation Utilizing Microfluidic Systems. In: Santra T.S., Tseng FG. (eds) Handbook of Single Cell Technologies. Springer, Singapore. 2020. (Chapter 1)

OTHER PUBLICATIONS

Journal Articles

1. Nurhayati RW, Cahyo RD, Pratama G, **Anggraini D**, Mubarok W, Kobayashi M, Antarianto RD. 2021. Alginate-Chitosan Microencapsulated Cells for Improving CD34+ Progenitor Maintenance and Expansion. Applied Sciences. 11(17):7887.

2. Zhang T, Shen Y, Kiya R, **Anggraini D**, Tang T, Uno H, Okano K, Tanaka Y, Hosokawa Y, Li M, Yalikun Y. 2021. Focusing of Particles in a Microchannel with Laser Engraved Groove Arrays. Biosensors. 11(8):263.

3. Juliandi B, Mubarok W, **Anggraini D**, Boediono A, Subangkit M, Bachtiar I, Murti H, Yaprianto K, Setiawan B. 2021. Spatial learning and memory of young and aging rats following injection with human Wharton's jelly-mesenchymal stem cells. Indonesian Journal of Biotechnology. 26(2):91-100.

4. Liem IK, Oktavina R, Zakiyah, **Anggraini D**, Deraya IE, Kodariah R, Krisnuhoni E, Wuyung PE. 2021. Intravenous injection of umbilical cord-derived mesenchymal stem cells improved regeneration of rat liver after 2AAF/CCL$_4$-induced injury. Online Journal of Biological Sciences. 21(2):317-326.

5. Zhang T, Namoto M, Okano K, Akita E, Teranishi N, Tang T**, Anggraini D**, Hao Y, Tanaka Y, Inglis D, Yalikun Y. 2021. Hydrodynamic particle focusing enhanced by femtosecond laser deep grooving at low Reynolds numbers. Scientific Reports. 11(1):1652.

Books

1. **Anggraini D**, Mubarok W, Nurhayati RW. Teknik Organ-on-a-Chip (*Organ-on-a-Chip Technique*). In: Nurhayati RW, Katili PA (eds) Rekayasa Jaringan (*Tissue Engineering).* UI Publishing. 2021.

2. Mubarok W, **Anggraini D**, Cahyo RD, Alawiyah K. Teknik 3D Bioprinting (*3D Bioprinting Technique*). In: Nurhayati RW, Katili PA (eds) Rekayasa Jaringan (*Tissue Engineering*). UI Publishing. 2021.

CONFERENCES

International conferences

1. **Anggraini D**, Okano K, Tanaka Y, Liu X, Yamada S, Hosokawa Y, Yalikun Y. Real-Time Guided Axon Growth of Primary Mouse Hippocampal Neurons Activated by Microscale Orifice. The International Chemical Congress of Pacific Basin Societies, December 16-21, 2021. (Poster)

2. **Anggraini D**, Liu X, Okano K, Yamada S, Tanaka Y, Inagaki N, Hosokawa Y, Yalikun Y. Real-Time Guided Axon Outgrowth of Primary Mouse Hippocampal Neurons Activated by Femtosecond Laser Pulses in Microfluidic Device. Miniaturized Systems for Chemistry and Life Sciences (μTAS), California, USA, October 10-14, 2021. (Poster)

3. Zhang T, Yalikun Y, Shen Y, **Anggraini D**, Tang T, Okano K, Tanaka Y, Li M, Hosokawa Y. Microfluidic Particle Separation Using Glass Structures. Miniaturized Systems for Chemistry and Life Sciences (μTAS), California, USA, October 10-14, 2021. (Poster)

4. **Anggraini D**, Okano K, Tanaka Y, Yamada S, Yalikun Y, Hosokawa Y. In Situ Guided Neurite Outgrowth by Femtosecond Laser Processing in a Microfluidic Device. The 34th IEEE International Conference on Micro Electro Mechanical Systems (MEMS), January 25-29, 2021. (Poster)

Domestic conferences

1. **Anggraini D**, Okano K, Tanaka Y, Yamada S, Yalikun Y, Hosokawa Y. In Situ Guided Neurite Outgrowth by Femtosecond Laser Processing in a Microfludic Device. Serendipity Symposium, Shizuoka, Japan, December 15-16, 2020. (Oral)

2. **Anggraini D**, Okano K, Tanaka Y, Yamada S, Yalikun Y, Hosokawa Y. Directional Neurite Outgrowth in Microfluidic Device Enabled by Precise Penetration of 4 μm Thin-Glass Sheet. 化学とマイクロ・ナノシステム学会 第 42 回研究会（Cheminas42), October 26-28, 2020. (Poster)

3. **Anggraini D**, Okano K, Tanaka Y, Yamada S, Yalikun Y, Hosokawa Y. In Situ Neurite Guidance Activated by Femtosecond Laser Processing in Microfluidic Device. The 81st JSAP Autumn Meeting, September 8-11, 2020. (Oral)

PATENTS

Retno Wahyu Nurhayati, Radiana Dhewayani Antarianto, Gita Pratama, Wildan Mubarok, **Dian Anggraini**, Jeanne Adiwinata Pawitan, Evah Luviah. Produk Mikroenkapsulasi Sel Punca Hematopoietik (*Product of Microencapsulated Hematopoietic Stem Cells*). 2020. *Patent Granted No. IDS000003218 on Indonesian Directorate General of Intellectual Property Rights, Indonesian Ministry of Law and Human Rights*.

Acknowledgements